Observational Constraints on Models of Rapidly Evolving Luminous Stars

Philip A. Rosenfield

A dissertation
submitted in partial fulfillment of the
requirements for the degree of

Doctor of Philosophy

University of Washington

2013

Reading Committee:

Julianne Dalcanton, Chair

Suzanne Hawley

Paul Hodge

Program Authorized to Offer Degree:
Astronomy

University of Washington

Abstract

Observational Constraints on Models of Rapidly Evolving Luminous Stars

Philip A. Rosenfield

Chair of the Supervisory Committee:
Julianne Dalcanton
Astronomy

Resolved stellar populations in galaxies are excellent laboratories for testing our understanding of galaxy formation, integrated colors and luminosities, supernova progenitor masses, and energy input from stellar feedback. However, the usefulness of resolved stellar populations rests on the ability to accurately model the evolution of the underlying stars.

In this dissertation, I present three projects, the first uses stellar evolution models of hot post-horizontal branch stars to explain the some of the of excess ultra-violet (UV) flux emitted from the center of the Andromeda galaxy. This flux was imaged as part of the Panchromatic Hubble Andromeda Treasury *HST* multi-cycle program, and excess of UV light from the centers of large elliptical galaxies has been well documented. Therefore, the results of this project go beyond stellar evolution and understanding M31. I find that this population of stars are indeed failed AGB stars or left the AGB early. I also find the stars producing the excess UV light are strongly concentrated in the central regions of the M31 bulge, which must shed light on the progenitor stars.

The subsequent two projects each constrain uncertain aspects of uncertain phases of stellar evolution using nearby dwarf galaxies from the *HST* ACS Nearby galaxy Survey Treasury and a follow-up *HST*/SNAP campaign which imaged a subset of ANGST galaxies in the near infrared.

The two uncertain phases of stellar evolution studied are the luminous core Helium burning (HeB) phase and the thermally pulsating AGB phase. Dwarf galaxies from the

ANGST are an ideal environment to test new models because they span 2 dex in metallicity, more than 30 galaxies have significant HeB populations, and we have HST/NIR follow up data for 26 galaxies with a large AGB population. I find that the convection occurring the HeB stars must increase in strength with increasing mass, and I find constrains on the mass loss prescriptions for low metallicity TP-AGB stars from $0.8- \sim 4M_{\odot}$

TABLE OF CONTENTS

Page

List of Figures iv

List of Tables xii

Chapter 1: Introduction 1
1.1 Basic Overview of Stellar Evolution 1
1.2 Connecting Theory to Observations 3
1.3 The Importance of Improving Stellar Evolution Models 5
1.4 Organization of this Disseration 10

Chapter 2: Bright UV Stars Throughout the Bulge of M31 11
2.1 Context 11
2.2 Introduction 12
2.3 The Data 15
2.3.1 PHAT Observations, Resolved Star Photometry, Astrometry 15
2.3.2 Comparison with FOC data 18
2.3.3 Radial Binning of UV Sources & Possible Contaminants 20
2.3.4 Integrated Light and Ancillary Imaging 22
2.4 Analysis 22
2.4.1 Radial Color–Magnitude Diagrams 22
2.4.2 Radial Luminosity Functions 25
2.4.3 Luminosity Contribution of HP-HB and P-AGB 26
2.4.4 Possible Contributions from Stellar Blends 30
2.4.5 Comparison to Other Evolving Populations 31
2.4.6 Stellar Population Lifetimes Inferred from Observations 34
2.5 Discussion 36
2.5.1 Gradients in Stellar Ages 38
2.5.2 Galactic Metallicity Gradient 39
2.5.3 Elemental Abundances Gradients 40

2.5.4 Radial Dust Gradients . . . 42
2.6 Closing Remarks . . . 43

Chapter 3: The Ratio of Blue and Red Helium Burning Stars in ANGST Galaxies 44
3.1 Context . . . 44
3.2 Introduction . . . 44
3.3 Stellar Evolution of HeB Stars . . . 49
3.3.1 Stellar Evolution During a Blue Loop . . . 49
3.3.2 Complications from Convection . . . 53
3.3.3 Core Overshoot and the Blue Loop: A New Model Grid . . . 54
3.4 Data . . . 56
3.4.1 Data Reduction . . . 56
3.4.2 Galaxy Sample . . . 60
3.4.3 Isolating the HeB Stars, and the RHeB and BHeB sequences . . . 60
3.4.4 HeB Sequences of the Galaxy Sample . . . 63
3.5 Analysis . . . 64
The Theoretical B/R Ratio . . . 72
Age-Magnitude Relationships with $\Lambda = 0.5$ . . . 78
3.5.1 B/R Ratios of the Galaxy Sample with B12 . . . 78
3.6 Discussion . . . 86
HeB Sequences with MDCOS . . . 87
Age-Magnitude Relationships MDCOS . . . 89
The B/R Ratios with MDCOS . . . 91
3.7 Conclusions . . . 92

Chapter 4: Constraining TP-AGB Lifetimes with Low-Metallicity Dwarf Galaxies 102
4.1 Context . . . 102
4.2 Introduction . . . 102
4.3 Data . . . 106
4.3.1 Resolved Stellar Populations in Optical and NIR . . . 106
4.3.2 Star Formation Histories of the Galaxy Sample . . . 106
4.3.3 Mean Metallicities of the Galaxy Sample . . . 107
4.3.4 Selecting AGB and RGB Stars . . . 108
4.4 Models . . . 111
4.4.1 Stellar Evolutionary Codes: PARSEC and COLIBRI . . . 112
4.4.2 COLIBRI Mass Loss Prescriptions . . . 112

4.5 Modeling the Data . . . 115
4.5.1 Population Synthesis with TRILEGAL . . . 115
4.6 Observational Constraints on Models . . . 117
4.7 Analysis . . . 117
4.7.1 Comparing the Mass Loss Prescriptions . . . 122
Mass Loss in the G10 Model . . . 123
Mass Loss in the VW93 Model . . . 123
Mass Loss in the BS95 Model . . . 124
4.7.2 What is Responsible for the Model-Data Disagreements . . . 124
Star Formation Histories . . . 128
4.7.3 Bracketing the Mass Loss Prescription . . . 129
4.8 Conclusions . . . 129

Chapter 5: Conclusion . . . 131

Bibliography . . . 133

Appendix A: A Note on the SFHs Used In Chapter 4 . . . 143

LIST OF FIGURES

Figure Number Page

1.1 Visual representation of stellar evolutionary phases. 5

1.2 Three views of the Andromeda Galaxy, closer and closer in to the center. Bottom right: Ultra-violet observations studied in Chapter 2. 6

1.3 Four of the ∼70 galaxies from ANGST with the HST footprints overlaid. These are among the galaxies studied in Chapters 3 and 4. *Image credit: http://www.nearbygalaxies.org/* 7

1.4 The galaxies from Fig. 1.3 as color magnitude diagrams. These are among the galaxies studied in Chapters 3 and 4. *Image credit: http://www.nearbygalaxies.org/* 8

1.5 An example CMD of an ANGST galaxy with stellar evolution phases annotated. 9

1.6 An example HRD with stellar evolution phases annotated. 9

2.1 Sample stellar evolutionary tracks (Bressan et al., 2012) showing hot HB stars and their progenies' placement on HR diagram (left) and CMD in UVIS filters (right) as seen at the distance of M31 (see Section 2.4.1). Each evolutionary channel is illustrated and labeled. A canonical AGB track (black) is not shown on right panel as it is fainter than $F336W = 28$. The P-AGB track is taken from Vassiliadis & Wood (1994) H-burning tracks for a mass of 0.597 $M_{\odot}$ and Z=0.016. Dashed box shows approximate range of other CMDs in this chapter. 14

2.2 Left: *HST* $F336W$ (blue), $F475W$ (green), and $F814W$ (red) composite mosaic of M31 bulge. Elliptical contours show locations of isophotes used as analysis region boundaries. The color scheme is used in other figures in this chapter and the median radius of each isophote bin is superimposed. Data within the innermost (black dotted) region are excluded from the analysis (see Section 2.3.3). The magenta box shows the footprint of the B98 FOC imaging. Right: GALEX FUV (blue) and NUV (green) composite mosaic of M31 (Barmby et al., 2006). The red ellipse denotes the outermost (black) contour displayed in left panel. The footprint of the M31 disk field plotted in Figure 2.5 is shown as a red rectangle in right panel. 17

2.3 A comparison of PHAT UV and FOC spatial overlap. Left: UV CMD for the B98 dataset. The FOC sources with PHAT counterparts are shown in red (filled circles), and FOC sources without PHAT counterparts are open circles. The PHAT data appear incomplete for the bluest sources with $F175W_{FOC} - F275W_{FOC} < -0.75$. Right: UV CMD for the PHAT dataset extracted from the smaller FOC footprint of B98. Stars that have matched counterparts in the B98 catalog are plotted in red (filled circles), and unmatched PHAT sources are open circles. The completeness limit of the PHAT data is roughly 0.3 magnitudes brighter in $F275W$ than the B98 FOC observations. The dashed lines correspond to B98 detection limit. 19

2.4 UV Color-magnitude diagrams of each analysis region. Dashed lines mark the 90% completeness limits and solid lines mark the 50% completeness limits (see Section 2.3). We limit our analysis to sources brighter than the 90% completeness limits in the innermost (green) region. The median projected radius of each distance-corrected logarithmically-spaced isophote is labeled in the upper left. The color scheme follows Figure 2.2. 21

2.5 Nature of the bright UV point sources in the central bulge (left) vs. star-forming regions in the field (right). The two panels on the left show the UV CMD for stars within 120 pc of the center; the two panels on the right show CMDs of the disk field (galactocentric radius $\sim$ 6.5 kpc; see red rectangle in the right panel of Figure 2.2). These CMDs are compared to MS tracks for young massive stars in the top panels; they are compared to P-AGB and HP-HB tracks for evolved stars in the bottom panels. It is apparent that the (reddened) MS tracks are a good match for the disk CMDs, but not the bulge (see Section 2.4.1). Markers are placed on the three most massive HP-HB tracks at 10^4 yr intervals. Two reddening vectors with $R_V = 3.1$ and 5 are also shown for 1 magnitude extinction in $F336W$. MS tracks assume $A_V = 0.99$ (Kang et al., 2009) and bulge tracks assume a pure MW foreground extinction of $A_V = 0.206$ (Schlegel et al., 1998). 23

2.6 Number of resolved HP-HB stars (left panel: $F275W$; right panel: $F336W$) as a function of magnitude, scaled by each region's stellar mass found by the 3.6μm M/L ratio (see Section 2.4.2), in bins of 0.2 magnitudes. The observed LFs are corrected for completeness and shown with thin lines fainter than the 90% completeness magnitude in the respective annulus (i.e., a correction by more than a factor of 1.1). The color scheme is the same as Figure 2.2, with green indicating the innermost bin. Long lived HP-HB stars are shown in model LF (dotted) evolved from the ZAHB with a flat distribution of mass below $1.0M_{\odot}$, and the Z=0.07 Y=0.389 tracks (cf. Figure 2.5). The model is normalized to the innermost region's peak LF in $F275W$. The over-abundance of stars with $F275W > 23$ in the innermost regions of M31 are associated with HP-HBs. The bright LF tails are due to a seemingly flat distribution of P-AGB stars (see Section 2.4.5). The increase in the model LF at faint magnitudes ($\gtrsim 24.5$) is due to numerous HB stars, of which the hottest likely dominate the UVX. 27

2.7 The radial distribution of UV sources. Left Panel: Surface brightness as a function of radius of $F275W$ (solid, black), $F336W$ (solid, red), HP-HB (dotted), and P-AGB(dashed). The best fit Sérsic profile from Courteau et al. (2011) is overplotted with μ_e shifted to $F336W$=23 (gray). Right Panel: Resolved flux ratio of HP-HB to P-AGB stars in each filter for each annulus. Shaded regions show Poisson uncertainty in number counts. In both panels, red denotes the $F336W$ filter and black denotes the $F275W$ filter. The characteristic metallicity as a function of radius reported by Saglia et al. (2010) is indicated on the top axes. Both the HP-HB and P-AGB populations increase toward the nucleus of M31, but the HP-HB stars show a dramatic increase in flux with respect to the P-AGB stars in the innermost regions. . 29

2.8 Input (black) and recovered (blue: $F275W$; green: $F336W$) luminosity functions in each of the radial bins. Close to the detection limit, blending causes an artificial upturn in the luminosity function. The effect only becomes appreciable below our adopted magnitude cuts (dashed lines) and is never above 27% (see Table 2.1 for exact values in each radial bin). 32

2.9 Surface density of UV-bright sources (blue = HP-HB, red = P-AGB), LMXBs (green, Voss & Gilfanov, 2007b), binned according to analysis region with Poisson uncertainties. The 3.6μm luminosity (black dashed) is plotted in different units and follows the right axis. The characteristic metallicity as a function of radius reported by Saglia et al. (2010) is indicated on the top axis. The least-squares fit power law index of each stellar component is noted above its profile with its uncertainty in the fitting. HP-HB (blue) and P-AGB (red) stars follow a different surface density profile than that of the 3.6μm light. However, the HP-HB stars seem to follow a profile consistent with the LMXBs. 33

2.10 Population variations in the central ~ 0.5 kpc of M31. Shown (solid, blue) is the inferred fraction of evolving MS stars that must go through the HP-HB channel to explain the HP-HB number count profile, given the integrated light properties. This fraction rises by about a factor of 3 towards the center. Shaded regions denote Poisson uncertainty. The Lick-Index based metallicity and its dispersion derived by Saglia et al. (2010) is shown on the right axis (dotted, black). 37

2.11 Strong anti-correlation as a function of radius between GALEX color (blue; Thilker et al., 2005) and the Lick Index-based metallicity and dispersion derived by Saglia et al. (2010) (right axis, black). There is a sharp increase in metallicity where the $FUV - NUV$ color becomes extremely blue. This anti-correlation may be evidence of the galactic metallicity gradient driving the radial variation in the numbers of UV-bright stars detected. The extreme blue color further shows that the UV-bright populations are strongly confined to the inner ~ 300 pc ($\sim 75''$) of the M31 bulge. 41

3.1 Representative CMDs in the galaxy sample. Examples of HeB regions in Sextans A and IC2574. BHeB stars are shown in blue and RHeB stars in red. The blue-ward plume of the BHeB is the main sequence. The ridge of stars red-ward of the RHeB are the RGB, which merge with the dense red clump at fainter magnitudes. Above the tip of the RGB and redder are AGB stars. Distance modulus, μ, and interstellar extinction A_v corrections are from Dalcanton et al. (2009), a reddening vector is drawn for 0.5 mag of extinction. 47

3.2 Sample Bressan et al. (2012) stellar evolution tracks for Z=0.001 and Y=0.25 from the beginning of the MS to Carbon burning or the first thermal pulse of the AGB (depending on mass). Blue loops are highlighted in blue and initial masses (in units of $M_\odot$) are marked at the beginning of the MS. Left: HR diagram, Right: CMD in HST filters. 51

3.3 Stellar interior parameters of a $5.0 M_\odot$ star during the blue loop. Top panels show important players in the blue loop (top to bottom): log effective temperature, and central parameters, mean molecular weight μ_c, density $\log \rho_c$, and pressure $\log P_c$ (all units in cgs). Bottom panel is a Kippenhahn diagram showing the mass fractions of convective regions (grey), He-burning core (red fill), H-burning shell (blue fill), and the edge of the convective core (solid black; region of convective overshooting is considered to be radiative). Relative central abundances are overlaid, ^{12}C, green; ^{16}O, purple; and He, red, as well as the relative amount of total luminosity due to Hydrogen fusion (blue dotted) and He fusion (red dotted). Grey vertical lines mark the RHeB, identifiable by the sharp change in $T_{\rm eff}$, and the BHeB, set at the maximum $T_{\rm eff}$ of the loop. 52

3.4 MSTO age differences (in Myr) with high and low values of core overshooting strength compared to the canonical value (Λ_c = 0.5 Bressan et al., 2012). Shown are three example metallicities Z = 0.001 (red), 0.004 (blue), and 0.02 (green). Increased core overshooting strength compared to Bressan et al. (2012) leads to a longer MS phase, and more so with increasing metallicity, while the opposite is true for relatively smaller values of Λ_c. The maximum fractional difference in MSTO age from either core overshoot value compared to Λ_c = 0.5 is 0.1 suggesting a wide range in core overshooting parameter exists without largely effecting stellar population ages. 57

3.5 The effects of core overshooting on the HR diagram (left) and an *HST* cmd (right). Shown are isochrones with $Z = 0.004$ and different core overshooting values, Λ_c = 0.3 (red), 0.5 (blue), and 0.7 (green). As Λ_c increases, the temperature extension of the blue loop decreases and the luminosity of the isochrone gets brighter. 58

3.6 Increasing core overshooting decreases the HeB lifetime and temperature extent of the loop. Shown here is an example of a $5M_{\odot}$ star with three values of core overshooting plotted against the fraction of the stellar lifetime (defined between the onset of He-burning until the first thermal pulse on the AGB). The adopted value in B12 and the preceding Padova Stellar Evolution models ($\Lambda_c = 0.5$) is shown in black, lower than canonical value Λ_c=0.3 is shown in red, and higher than canonical value Λ_c=0.7 is shown in blue 59

3.7 Optical ($F606W - F814W$) CMDs of sample galaxies with the BHeB and RHeB sequences identified with isochronal metallicities of 0.0007 and 0.001 (colored lines). Combined photometry of the galaxies are plotted below. Contours are drawn on areas of the cmd with a stellar density of at least 100 per CMD box of color width, 0.05 and mag height, 0.1. Contours are spaced logarithmically. 65

3.8 Same as Figure 3.7 but for $Z = 0.008$. 66

3.9 Same as Figure 3.7 but for $Z = 0.03$. 67

3.10 Same as Figure 3.7 but with $F555W - F814W$ and for $Z = 0.007$ and 0.001. 68

3.11 Same as Figure 3.10 but for $Z = 0.002$ and 0.003. 69

3.12 Same as Figure 3.10 but for $Z = 0.15$. 70

3.13 Optical ($F606W - F814W$) CMDs of all the BHeB and RHeB sequences identified in the data colored by nearest isochrone metallicity. 71

3.14 Optical ($F555W - F814W$) CMDs of all the BHeB and RHeB sequences identified in the data colored by nearest isochrone metallicity. 71

3.15 HeB Sequences ranging from $2 - 12M_{\odot}$ for different Z and different Λ_c in HST optical filters (with no reddening or extinction). Increasing overshoot decreases the extension of the loops, as shown in Figure 3.5. Isochrone values of $M_{\rm bol}, L\ T_{\rm eff}$ and $\log g$ were converted to HST filters with bolometric corrections from Girardi et al. (2008a). 73

3.16 Same as Figure 3.15 but with $F555W - F814W$ CMDs. 74

3.17 The predicted B/R ratio with $\Lambda_c = 0.3, 0.5$ and 0.7 (top to bottom) at lower metallicities. High ratio values at young ages and missing data are evidence of the HeB failing to undergo a blue loop. A slight metallicity effect can be seen at old ages, where the B/R ratio increases with increasing metallicity. Vertical axes are not at the same scale to emphasize the dynamic range of each panel) 76

3.18 The predicted B/R ratio with $\Lambda_c = 0.3, 0.5$ and 0.7 (top to bottom) at higher metallicities. High ratio values at young ages and missing data are evidence of the HeB failing to undergo a blue loop. Unlike the lower metallicities (Figure 3.17, the does not seem to be a metallicy effect. Vertical axes are not at the same scale to emphasize the dynamic range of each panel) 77

3.19 Age magnitude relationships for B12 models for the BHeB (left) and RHeB (right). Also plotted is the change in HeB magnitude as a function of BHeB age. 79

3.20 Theortical HeB Sequences ranging from $2 - 12M_{\odot}$ for different Z (dotted) and different Λ_c (increasing from top to bottom) in HST optical filters (with no reddening or extinction). Observationally measured HeB sequences are shown in solid lines). Increasing overshoot decreases the extension of the loops, as shown in Figure 3.5. Isochrone values of $M_{\rm bol}, L\ T_{\rm eff}$ and $\log g$ were converted to HST filters with bolometric corrections from Girardi et al. (2008a). 80

3.21 Measurements of the B/R ratio binned into sub-figures by isochronal metallicity. Two panels for each sub-figure. Top panel shows the observed B/R ratio (measured by applying the age-magnitude relationship to HeB stars) for each field (light gray) and the mean B/R ratio of the combined fields (black, solid). Over-plotted is the theoretical B/R ratio (black, dashed). The bottom panels show the fraction difference between the observed and theoretical B/R ratio. The theoretical B/R ratio was calculated directly from the stellar evolution tracks, if tracks were not calculated at the exact metallicity, the nearest metallicity calculated is shown. 81

3.22 Same as Figure 3.21 but for galaxies with isochronal metalicity $Z = 0.002$. . . 82

3.23 Same as Figure 3.21 but for galaxies with isochronal metalicity $Z = 0.003$. . . 83

3.24 Same as Figure 3.21 but for galaxies with isochronal metalicity $Z = 0.006$. . . 84

3.25 Same as Figure 3.21 but for galaxies with isochronal metalicity $Z = 0.008$. . . 85

3.26 HeB sequences with MDCOS. Left: HRD, right: CMD in HST filters. Compared to Bressan et al. (2012, See Figure 3.20 middle panel), fainter loops are more extended, while brighter loops are less extended. 89

3.27 Change in bolometric mag on the BHeB and RHeB as a function of BHeB magnitude for B12 (left) and MDCOS (right) 90

3.28 Age magnitude relationships for MDCOS for the BHeB (left) and RHeB (right). Also plotted is the change in HeB magnitude as a function of BHeB age. 90

3.29 Same as Figure 3.21, but using MDCOS models. 93

3.30 Same as Figure 3.29, but with galaxies with measured metallicity $Z = 0.002$. 94

3.31 Same as Figure 3.29, but with galaxies with measured metallicity $Z = 0.003$. 95

3.32 Same as Figure 3.29, but with galaxies with measured metallicity $Z = 0.006$. 96

3.33 Same as Figure 3.29, but with galaxies with measured metallicity $Z = 0.008$. 97

3.34 Same as Figure 3.29, but with galaxies with measured metallicity $Z = 0.011$. 98

3.35 Same as Figure 3.29, but with galaxies with measured metallicity $Z = 0.015$. 99

3.36 Same as Figure 3.29, but with galaxies with measured metallicity $Z = 0.018$. 100

4.1 Composite Hess diagrams of the $Z \sim 0.002$ galaxy sample (see Table 4.1). Each galaxy was first converted to absolute magnitudes using A_V and $m-M_0$ derived in Dalcanton et al. (2012) (and refs. therein. Parameters are also listed in Table 4.1). To create a single region each galaxy was then shifted in $F160W$ or $F814W$ to match the average M_{TRGB} (thick horizontal line), and the color and magnitude offsets of the RGB and AGB regions were applied to each individual galaxy. The separation between RHeB stars and AGB stars were chosen by eye and then assessed for contamination from other stellar phases (blue polygon). 105

4.2 Sample evolutionary tracks calculated with COLIBRI for TP-AGB stars under three mass loss prescriptions. Each track has $Z = 0.002, Y = 0.252$. Top: Mass loss rate over time, the increase of $\dot{M}$ with luminosity in BS95 (blue) is evident, as well as the higher efficiency of mass loss, where the TPAGB is reached just after 1 Myr. VW93 (green) has the longest lifetimes of the three. G10 begins with lower mass loss rates than VW93 but steadily increases. Bottom: Example HR diagrams, the three prescriptions follow very similar tracks, however, G10 and VW93 are intrinsically brighter than BS93, and continue to pulsate while becoming PNe. 116

4.3 CMDs and LFs calculated with each mass loss prescription compared to data for all the galaxies in the sample. Left and middle panels with each frame are $F110W - F160W$ CMDs of data (left) and model (middle), with numbers of RGB and AGB stars indicated. Horizontal lines mark the TRGB (see Table 4.1) and 1.5 mag below. Right panels show LFs of the models and data. The left side of the figure grid is calculated with $\dot{M}_{G10}$; middle with $\dot{M}_{BS95}$; and right with $\dot{M}_{VW93}$. From top to bottom are SCL-DE1, DDO78, and DDO71. 119

4.4 Same as Figure 4.3 but with galaxies DDO82, IC2574, and NGC4163 (from top to bottom). 120

4.5 Same as Figure 4.3 but with galaxies UGC8508 and two fields of UGC4305 (from top to bottom). 121

4.6 A comparison of the LF produced by the $\dot{M}_{G10}$ models. Top panel shows the LF of the models for each galaxy, this is a combination of the right-most panels of Figure 4.3. The percent difference in each magnitude bin is shown in the middle panel, and the bottom panel shows the residuals of the model and data. Galaxies with recent star formation are colored blue, the rest are colored red. 125

4.7 Same as Figure 4.6 but with $\dot{M}_{VW93}$. 126

4.8 Same as Figure 4.6 but with $\dot{M}_{BS95}$. 127

4.9 The lifetimes of TP-AGB stars with each mass loss prescription vs initial mass. The mass loss prescriptions bracket the probable lifetimes of TP-AGB stars (filled in grey). Left panel: Full TP-AGB tracks, right panel: TP-AGB stars brighter than the TRGB 130

A.1 TRILEGAL simulation using the SFH derived for SCL-DE1 calculated with stellar evolution models similar to those used in G10 (Padova) compared to the same, but calculated with PARSEC and COLIBRI. Top left: G10 models, top right: PARSEC and COLIBRI models, bottom left: fractional difference between the models, and bottom right: significance of difference given by $\mathrm{sign}(n-m)\sqrt{\chi^2}$ where n is the number of stars in top left CMD, m is the number of stars in the top right CMD, and χ^2 is the Poisson-equivalent χ^2 statistic: $2(m+n(\log(n/m)-1))$ (Dolphin, 2002). The total χ^2 is annotated on the bottom right panel. Differences in the models are discussed in the text. 145

A.2 Same as Fig. A.1 but for DDO71 146

A.3 Same as Fig. A.1 but for DDO78 147

A.4 Same as Fig. A.1 but showing NIR CMDs and LFs (SFHs still derived from optical CMDs). 148

A.5 Same as Fig. A.4 but for DDO71 149

A.6 Same as Fig. A.4 but for DDO78 150

LIST OF TABLES

Table Number Page

2.1 Region area is of each logarithmically spaced isophote; a is the semi-major axis (see Section 2.3.3), given in minimum, maximum, and median. The median radius is calculated directly from the isophotal boundary, assuming distance modulus $(m - M)_0 = 24.47$ (McConnachie et al., 2005). $N_{\rm stars}$, are the numbers of UV-sources in each annulus (detected in both filters and brighter than the 90% completeness magnitude of the innermost bin); 90% Comp., percent completeness magnitude in each annulus. Frac Cont., fractional contamination at the 90% completeness magnitude of each annulus (see Section 2.4.4). 18

2.2 First two columns are the same as in Table 2.1, followed by B/D, the bulge-to-disk ratio of luminosity within each annulus (Howley et al., in prep); $F_{3.6\mu\rm m}$, region integrated flux within each annulus obtained from Spitzer/IRAC 3.6μm imaging (Barmby et al., 2006). Next are integrated and resolved flux measurements in each UVIS filter, followed by the resolved flux of HP-HB stars. All UVIS fluxes are in units of 10^{-15} erg cm^{-2} s^{-1} Å^{-1}. Finally, the surface densities of the resolved UV-bright populations are tabulated (cf. Figure 2.9). 34

3.1 Properties of the 33 sample galaxies. Sources: (1) Piersimoni et al. (1999); (2) van Zee (2000); (3) van Zee & Haynes (2006); (4) van Zee et al. (2006); (5) Berg et al. (2012); (6) Croxall et al. (2009); (7) Kniazev et al. (2005); (8) Marble et al. (2010, and refs. therein); (9) Tüllmann et al. (2003); (10) Saviane et al. (2008); (11) Lee et al. (2003); and (12) Kobulnicky & Skillman (1996) 61

4.1 Columns 3–7 from Dalcanton et al. (2012), column 8 from Berg et al. (2012); Marble et al. (2010, and refs. therein). $\log[O/H]$ for DDO78, DDO71, and SCL-DE1 were taken from the SFH weighted average calculated by MATCH. 110

4.2 Mass loss prescriptions used in this chapter η refers to Reimers (1975)'s efficiency parameter. For every computational step, the mass loss rate is $\dot{M} \equiv \max[\dot{M}_{pre-dust}, \min(\dot{M}_{dust}, \dot{M}_{SW})]$ (see Marigo, 2013). 114

4.3 The AGB to RGB ratio using several mass loss prescriptions with random uncertainties. From the table we find wide spread over production of all TP-AGB stars, with the least being from the BS95 mass loss prescription and the largest being from VW93. 118

ACKNOWLEDGMENTS

I would like to thank first and foremost, Dr. Julianne Dalcanton, for the enormous amounts of expertise, enthusiasm, and support for every part of this process. Access to her excellent collaborators have provided unquantifiable amounts of motivation and help in synthesizing ideas and gaining experience both in aspects of observational astronomy and theoretical stellar astrophysics. Of those collaborators were Dr. Léo Girardi, Dr. Paola Marigo, and Dr. Alessandro Bressan, who provided countless helpful discussions and generously hosted three visits to Padova. Also, Dr. Tod Lauer, Dr. Evan Skillman, and Dr. Kristen McQuinn were always available to help shape ideas and put them into broader context. Dr. Ben Williams, Dr. Daniel Weisz, and Dr. Morgan Foresneau, and Mr. Cliff Johnson were always available to synthesize ideas, brainstorm, and help me process data that I was not yet familiar. Dr. Henny Lamers' stellar evolution class and his huge contribution to the literature helped me outline the pedagogical process I've since used in talks and in the following work.

DEDICATION

To my family,

and especially Grandma,

who would have read this cover to cover.

Chapter 1

INTRODUCTION

In the last twenty years, observations with the Hubble Space Telescope (HST) have revolutionized our ability to understand stellar evolution and test stellar evolution models. We can now measure the individual brightness and temperature of stellar surfaces in galaxies over 4 Mpc away.

This thesis uses data from two major HST treasuries to constrain models of luminous, rapidly evolving stars . The first, used in Chapter 2 is the Panchromatic Hubble Andromeda Treasury (PHAT; Dalcanton et al., 2012), shown in Fig. 1.2. We use some of the first data available from this multi-cycle treasury, which are of the center of M31. We found the largest sample to date of the progeny of extreme horizontal branch stars (see below).

The second HST treasury is the ACS Nearby Galaxy Survey Treasury (ANGST Dalcanton et al., 2009). ANGST is a volume-limited sample of ∼70 nearby galaxies from $\sim 1.5 - 4$Mpc (four of these galaxies are shown in Fig. 1.3). Many of these galaxies have a luminous, core Helium burning sequence populated from $\sim 2 - 12 M_{\odot}$, making the survey an excellent source of HeB stars to test stellar evolution models, which we present in Chapter 3. These galaxies also boast a large population of thermally pulsating AGB stars, the most uncertain phase of low and intermediate mass stars. We constrain how these stars lose their mass in Chapter 4. First, we will introduce some theoretical background to the thesis, which will be presented in more depth in the relevant chapters.

1.1 Basic Overview of Stellar Evolution

Most stellar evolutionary phases are distinguishable by their major sources of energy (fusion) as well as where the energy sources are located within the stellar interior (either in the core, or shells some distance from the core). Fig. 1.1 shows a rough schematic of how low and intermediate mass stars change over time. The top panel shows a sketch of the stellar

evolution of a star like the Sun. On the left, the star is in its main sequence (MS) phase, burning[1] Hydrogen in its core. Over time, when the supply of core Hydrogen runs out, fusion continues in a shell of Hydrogen around a degenerate Helium-rich core; now the star is on the red giant branch (RGB). As the star continues to fuse Hydrogen, the star becomes brighter, "climbing" the RGB, until the temperature of the degenerate core becomes high enough for Helium fusion. This causes the star to contract and become a horizontal branch star[2] (HB). HB stars burn Helium in their core and Hydrogen in a shell above. When there is no core Helium left, at the end of the HB phase, the star's core is degenerate again, and fusion occurs in Helium and Hydrogen shells, this phase is known as the Asymptotic Giant Branch (AGB). As the evolution progresses, the star strips away its outer envelope, becoming a planetary nebula that will dissipate and eventually leave behind a white dwarf.

A peculiar case of the HB, when it has very little convective envelope is discussed in Chapter 2.

The bottom panel of Fig. 1.1 is for stars more massive than the Sun, though not massive enough to ever fuse Carbon in the core (otherwise they would not have the planetary nebula phase). One major difference between the stars in each horizontal panel is in the Helium burning phase. Unlike HB stars, the core Helium burning phase is split in two. An intermediate mass star will begin core Helium burning with no degenerate core. It begins as a red Helium burning star (RHeB) and then becomes a blue Helium burning star (BHeB) before becoming an AGB star. HeB stars are the subject of Chapter 3.

The AGB is one of the most fascinating and uncertain evolutionary phases because so many interesting physical processes happen during the AGB. To list a few, core degeneracy, double shell fusion, large convective envelopes that vanish periodically, He-flashes and thermal pulsations, drastic chemical evolution of the surface, dust and molecule production, and enormous amounts of mass loss.

---

[1]It is so common in astronomical literature to use the term "burning" to mean "fusion" that is has become confusing to use correct terminology

[2]Many stellar evolutionary phases are named after their appearance on classic stellar evolution diagrams. The horizontal branch makes a horizontal shape mainly because the size of the He-rich core are all the same, no matter what the initial mass, the variable color is from the size of the convective envelope surrounding the star.

The AGB is final stage for all stars from $\sim 1 - 8M_{\odot}$, possibly $10M_{\odot}$ (e.g,. Herwig, 2005). Stars enter this stage after core He-burning and remain until nearly the entire surface is stripped away by winds. The details of everything that happens in between are still uncertainly modeled. We constrain AGB models in Chapter 4.

This basic picture of stellar evolution has been pieced together over years of theoretical and observational work, and begs the question: How does one go from observations of resolved stellar populations to constraining stellar evolution models?

1.2 Connecting Theory to Observations

Photometric data in more than one filter allow us to measure the distribution of colors and magnitudes of stars. With these data, we can (statistically) identify which evolutionary stage a star is in given only a few pieces of information.

The first step is to exploit the fact that a star's luminosity is related to its radius and temperature ($L \propto R^2T^4$). The Hertzprung-Russell (HR) diagram is a plot of $\log L$ against $T_{\rm eff}$ of some set of stellar models, shown for $Z = 0.001$ in Fig. 1.6. The location of a star on this diagram is directly related to the current stellar evolution phase the star is in, since there is a precise relationship between $\log L$ and $T_{\rm eff}$ and the luminosity of the star is set by the fusion process and stars are for the most part, black bodies.

Each line in Fig. 1.6 is a stellar evolution "track" at a given mass, labeled at the bottom left where the track "starts." A stellar evolution track is a parametric curve a star takes over its lifetime (what isn't shown, however, is how long a star spends at any given location). These tracks begin at the onset of Hydrogen fusion (MS), cool to become RGB stars, and evolve to become RHeB, BHeB, and finally AGB stars. Lower mass stars become HB stars, which are shown in the lowest mass tracks at $\log T_{\rm eff} \sim 3.8, \log L \sim 2$ (but not annotated).

The next step is a matter of calculating how much of the star light is expected to be emitted by the star in the observed filter sets. Transforming the luminosity, temperature, and radius (though in practice usually, $\log g$, the surface gravity) to HST filters takes the inclusion of atmospheric models, and is inherently complicated. Throughout this thesis, we use the transformations in Girardi et al. (2008a), and refer the reader to that paper for details. Once that transformation is complete, we can compare the models to the

observations using a color-magnitude diagram.

Sample color-magnitude diagrams (CMD) are shown in Fig. 1.4, which directly matches the layout of Fig. 1.3. The CMD of Sextens A, the galaxy in the upper left panel of Figures 1.3 and 1.4 is shown in Figure 1.5 with the same stellar evolutionary phases annotated as in Figure 1.6. The MS phase is the bluest in the optical filters, forming a bright plume and spreading with increasing photometric error at fainter magnitudes. The RGB is shown as a highly populated red sequence just brighter than the red clump. The red clump is a specific instance of the HB phase. Two other sequences are seen between the MS and RGB, these are the RHeB and BHeB. As mentioned above, the RHeB and BHeB are in the same core Helium burning phase, but separated on the CMD (for reasons discussed in Chapter 3). Finally, the AGB stars are shown brighter and redder than the RGB.

From here, we use several tools to understand how well the models match the observations. For example, in Chapter 2, we use the fuel consumption theorem (FCT, Renzini & Buzzoni, 1986a) which exploits the main sequence turn-off as a stellar clock. We use the FCT to estimate the percentage of the stellar population of the bulge is responsible for the excess ultra-violet light we detect.

We also model the evolution of a population of extremely hot HB stars and compare the model luminosity distribution (luminosity function, LF) to that observed. LFs are classic stellar evolution callibrators. We also use LFs in Chapter 4, where we calculate several thermally pulsating AGB models with different mass loss prescriptions and compare the model and observed LFs.

The CMD is also a powerful tool to test new stellar evolution models. In Chapter 3 we use the magnitude and color distributions of HeB stars in the ANGST sample to show there is a mass dependence to the strength of a boundary effect of stellar convection.

The analysis in Chapter 4 also makes use of CMD-derived star formation histories (SFH). This method uses the relationship between the number density of stars in any evolutionary phase on a CMD of a galaxy to how many stars were initially produced in the galaxy (at a time long enough ago to allow the stars to be currently passing through the observed phase). If we know the star formation history of a galaxy, and we have physical models that predict how long stars spend in each phase, (as well as the initial mass distribution of the

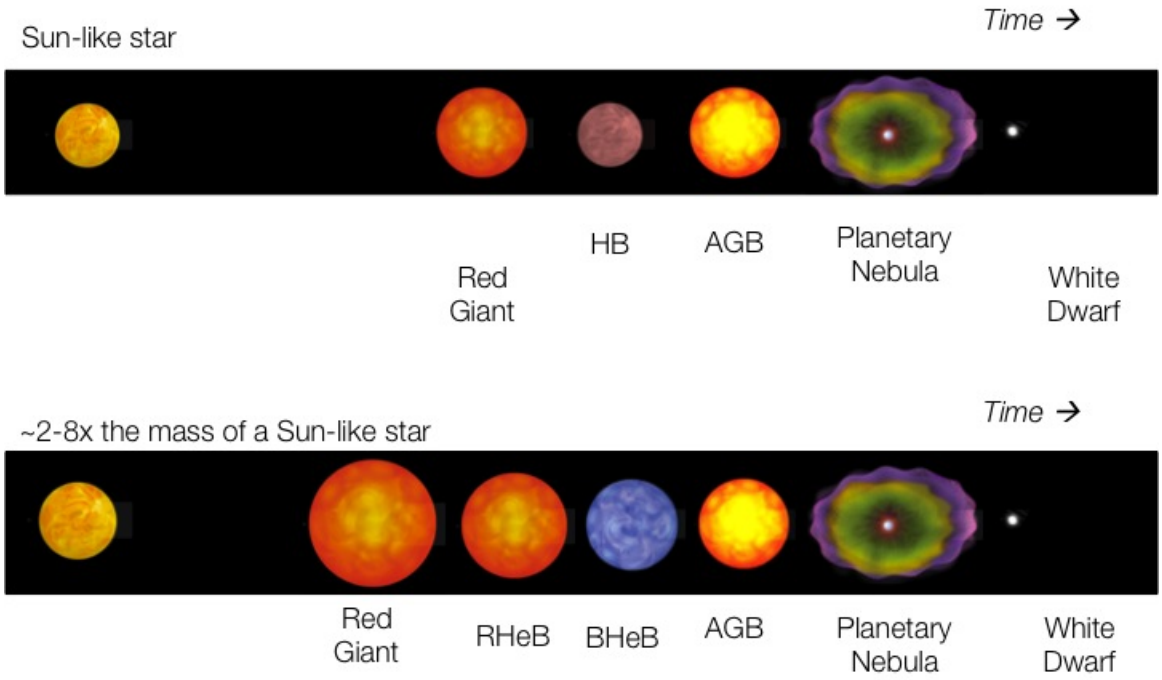

Figure 1.1 Visual representation of stellar evolutionary phases.

stars) we can model CMDs of galaxies and test our models (within the uncertainties of the star formation histories).

Together, we use these observational tools and the excellent observations from *HST* to constrain the theoretical models of AGB and HeB stars.

1.3 The Importance of Improving Stellar Evolution Models

There are several lines of reasoning to improve stellar evolution models. Firstly, and most obvious, is that stellar evolutionists want to understand the physics of stars. Other fields within astronomy also benefit. Nearby galaxies are the end points of cosmological simulations. If we understand the stars in these galaxies, we can then unravel the the history of star formation in the nearby galaxies, to finally make constraints on cosmological simulations.

Observational astronomers also depend on stellar evolution models. For example, extragalactic astronomers use stellar models by combining them with synthetic spectra to

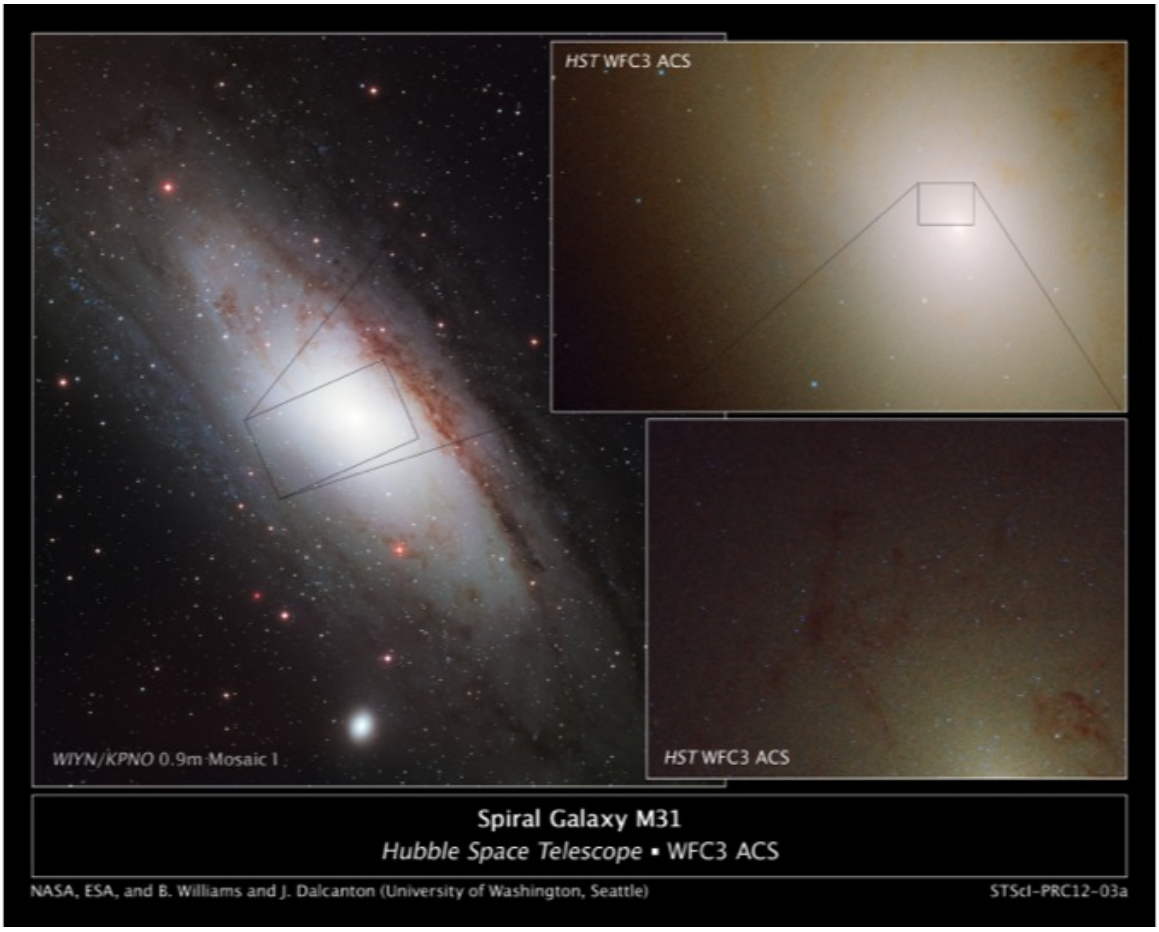

Figure 1.2 Three views of the Andromeda Galaxy, closer and closer in to the center. Bottom right: Ultra-violet observations studied in Chapter 2.

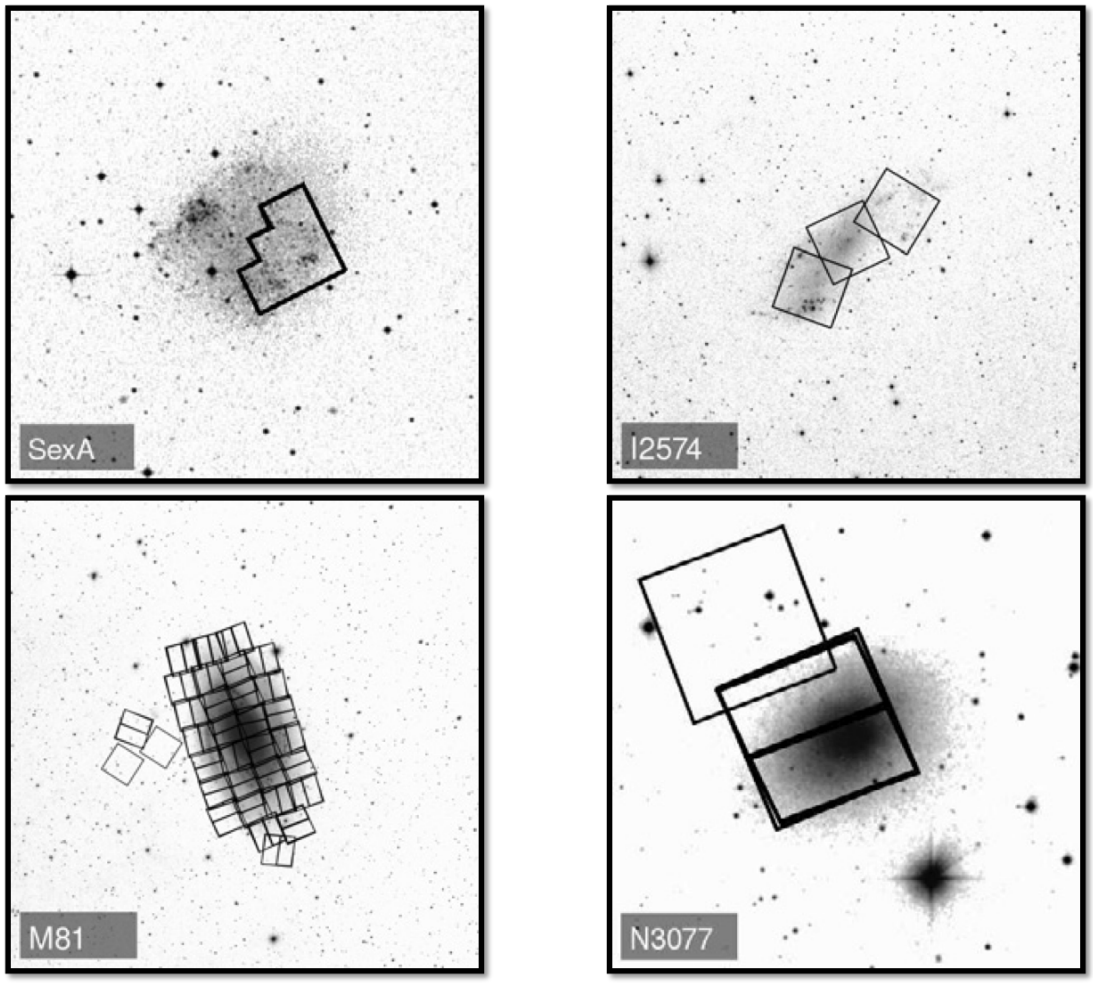

Figure 1.3 Four of the ∼70 galaxies from ANGST with the HST footprints overlaid. These are among the galaxies studied in Chapters 3 and 4. *Image credit: http://www.nearbygalaxies.org/*

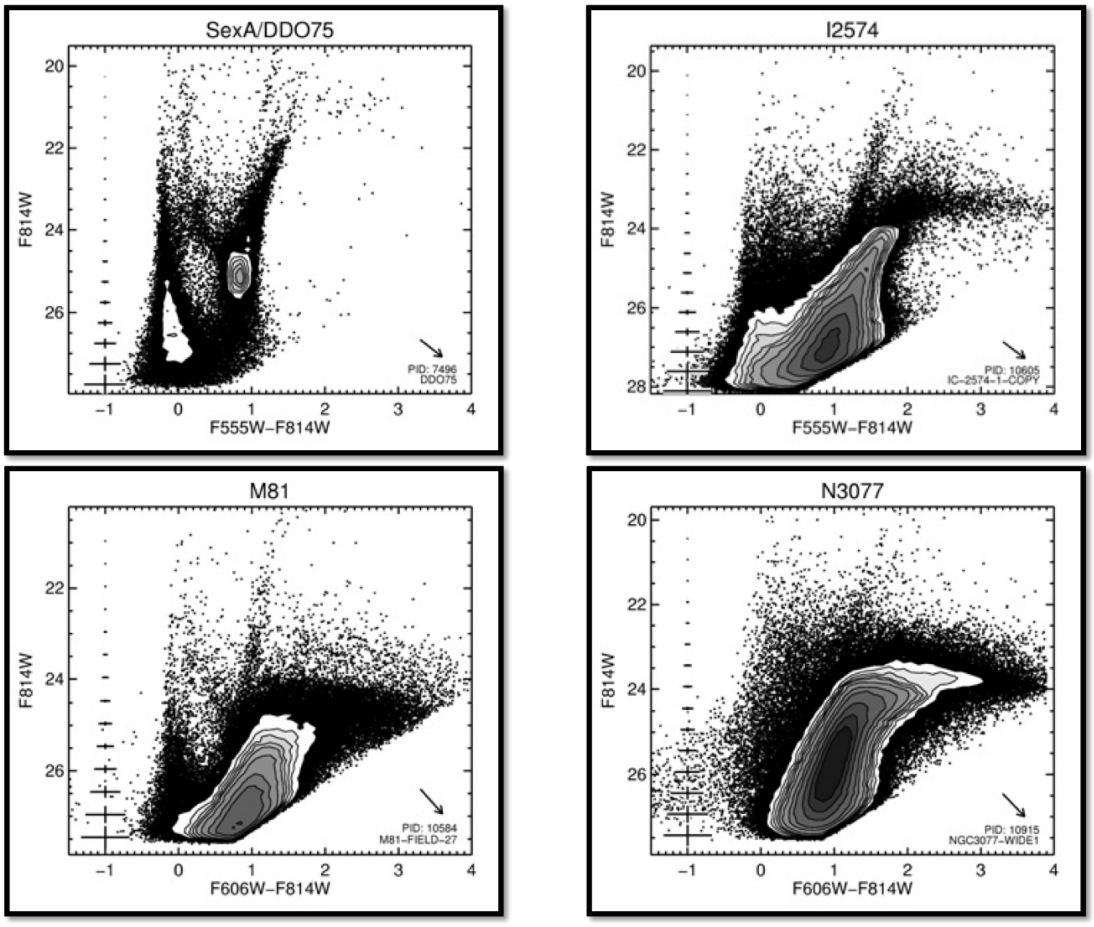

Figure 1.4 The galaxies from Fig. 1.3 as color magnitude diagrams. These are among the galaxies studied in Chapters 3 and 4. *Image credit: http://www.nearbygalaxies.org/*

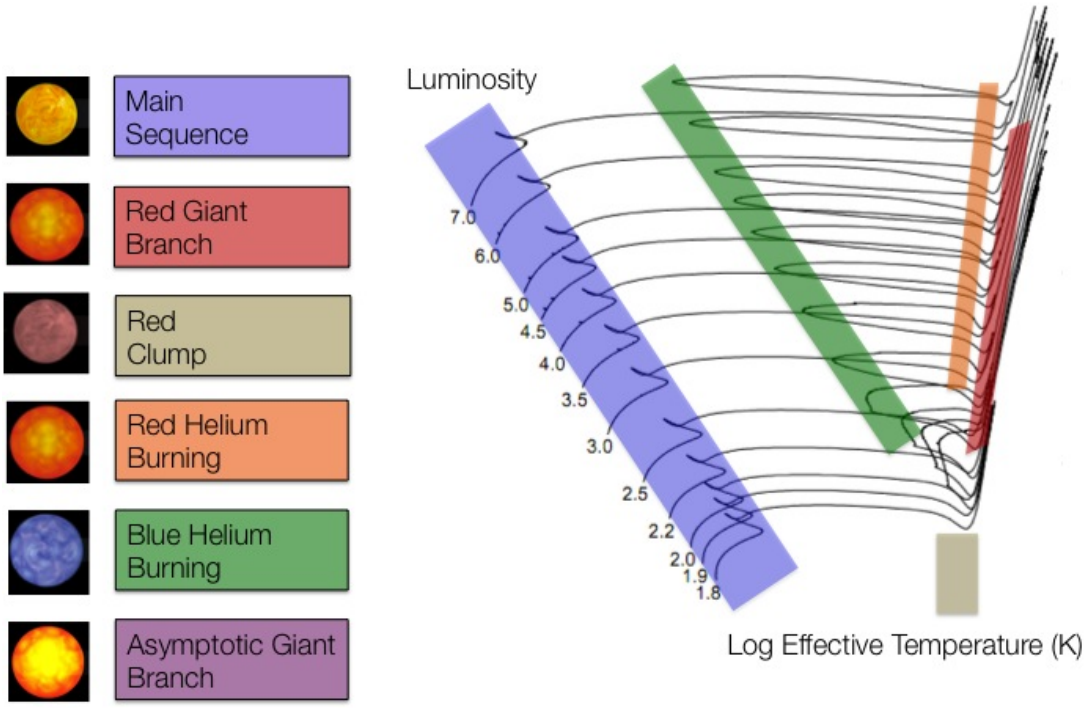

Figure 1.5 An example CMD of an ANGST galaxy with stellar evolution phases annotated.

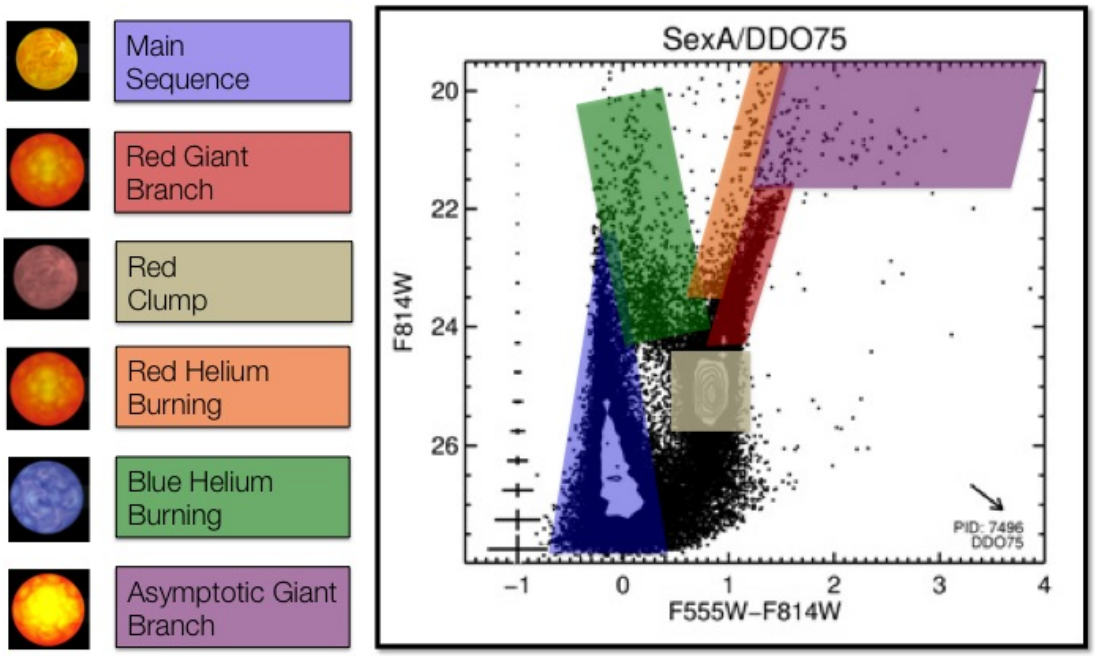

Figure 1.6 An example HRD with stellar evolution phases annotated.

understand integrated light properties of distant galaxies. Astronomers searching locally for planets rely on stellar models, which are quite literally shining light on the objects they wish to detect.

1.4 Organization of this Disseration

This dissertation is organized as follows. Chapter 2 is about the apperience and radial variation of the progeny of EHB stars found in the center of the Andromeda galaxy. Chapter 3 aims to illeviate recent problems in lumious core Helium burning star models by introducing a simple mass dependent core overshooting prescription in intermediate mass HeB stars ($> 1.75 M_{\odot}$). Chapter 4 presents constraints to mass loss prescriptions in low mass, low metallicity TP-AGB stars ($\sim 1 - 3 M_{\odot}, Z = 0.002$). Finally, we conclude in Chapter 5.

Throughout this dissertation, I use the pronoun "we" because members of the Padova Stellar Evolution Group, the PHAT team, and the ANGST team made significant contributions to these projects. The aspects in which I was most distant were in the observational design and acquisition of the data, the data reduction, and the maintenance and development of stellar evolution codes (the PARSEC code, used in every chapter, had its beginnings after World War II). However, I am certainly the primary investigator for each project and either did the analyses myself or lead others in small aspects of individual projects.

All magnitudes quoted throughout this thesis are in the VEGAMAG system.

Chapter 2

BRIGHT UV STARS THROUGHOUT THE BULGE OF M31

2.1 Context

We start with peculiar horizontal branch stars, though we don't observe them directly. The progeny of these stars were serendipitously observed as part of a ~ 1000 HST orbit multi-cycle campaign to image $\sim 1/3$ of the M31 star forming disk. The observations studied in this chapter came from the center of M31. This chapter is reproduced by permission of the AAS (Rosenfield et al., 2012).

As part of the Panchromatic Hubble Andromeda Treasury (PHAT) multi-cycle program, we observed a $12' \times 6.5'$ area of the bulge of M31 with the WFC3/UVIS filters $F275W$ and $F336W$. From these data we have assembled a sample of ∼4000 UV-bright, old stars, vastly larger than previously available. We use updated Padova stellar evolutionary tracks (Bressan et al., 2012) to classify these hot stars into three classes: Post-AGB stars (P-AGB), Post-Early AGB (PE-AGB) stars and AGB-manqué stars. P-AGB stars are the end result of the asymptotic giant branch (AGB) phase and are expected in a wide range of stellar populations, whereas PE-AGB and AGB-manqué (together referred to as the hot post-horizontal branch; HP-HB) stars are the result of insufficient envelope masses to allow a full AGB phase, and are expected to be particularly prominent at high Helium or α abundances when the mass loss on the RGB is high. Our data support previous claims that most UV-bright sources in the M31 bulge are likely hot (extreme) horizontal branch stars (EHB) and their progeny.

We construct the first radial profiles of these stellar populations, and show that they are highly centrally concentrated, even more so than the integrated UV or optical light. However, we find that this UV-bright population does not dominate the total UV luminosity at any radius, as we are detecting only the progeny of the EHB stars that are the likely source of the UVX. We calculate that only a few percent of MS stars in the central bulge

can have gone through the HP-HB phase and that this percentage decreases strongly with distance from the center. We also find that the surface density of hot UV-bright stars has the same radial variation as that of low-mass X-ray binaries. We discuss age, metallicity, and abundance variations as possible explanations for the observed radial variation in the UV-bright population.

2.2 Introduction

Many elliptical and large spiral bulges show enhanced ultra-violet (UV) flux towards their centers. This excess from $\sim$ 2000Å to the Lyman limit is referred to as either the UV upturn, UV-rising branch, or UV-excess (UVX). First discovered by Code (1969), explanations of the UVX converged on stellar phenomena as higher resolution telescopes came online (Bertola et al., 1995; King et al., 1992, 1995; Brown et al., 1998, 2000) and far-UV spectra from HUT and FUSE became available (Brown et al., 1997).

The UVX is generally believed to be due to core Helium burning stars (commonly known as horizontal branch stars; HB) and their descendants. These stars have evolved off the zero-age horizontal branch (ZAHB) and are following some combination of three evolutionary channels to becoming white dwarfs, depending on the fraction of their stellar envelope lost while they were red giants. Stars with a modest amount of mass-loss on the red giant branch (RGB) will leave the red side of the HB, lose a large convective envelope as canonical asymptotic giant branch (AGB) stars, and become Post-AGB (P-AGB) stars. Intermediate amounts of mass loss will leave stars with smaller convective envelopes (which will be subsequently lost) and hotter effective temperatures than canonical AGBs. These stars will leave the AGB track early, becoming post-early AGB (PE-AGB) stars[1]. Stars that lose nearly all their envelopes on the RGB become extreme (blue) horizontal branch (EHB) stars. These stars will have envelopes which are too small and temperatures which are too high to reach the canonical AGB line, and instead will become AGB-manqué or post-EHB stars (for a full review see Greggio & Renzini, 1999; O'Connell, 1999).

Examples of these stars' evolutionary tracks and the hot side of the ZAHB are illustrated

[1]This same effect can also arise in certain scenarios where stars burn their envelopes from the bottom up on the ZAHB, also leading to PE-AGBs.

in Figure 2.1 for both a Hertzsprung-Russell diagram and UV color-magnitude diagram (CMD). AGB-manqué and PE-AGB stars collectively are long-lived, hot post-HB stars (hereafter referred to as HP-HB). These HP-HB are 2-4 magnitudes brighter in $F336W$ than EHB stars with similar $F275W - F336W$ color. HP-HB stars have bolometric luminosities around 10^{2-3} $L_{\odot}$ and have typical effective temperatures of 15,000–20,000 K, compared to $L \sim 30$ $L_{\odot}$ and $T_{\rm eff} = 10^4$ K for HB stars (Bressan et al., 2012). The initial masses of stars that become HP-HB is never more than 2 $M_{\odot}$, corresponding to main sequence (MS) lifetimes $\gtrsim 0.6$ Gyr.

Brown et al. (1998) (hereafter B98) obtained HST Faint Object Camera (FOC) data in the M31 bulge, providing one of the most detailed discussions of these different types of UV-bright stars. However, these data only covered a small area ($14'' \times 14''$; see magenta box in Figure 2.2). Since radial gradients in age and metallicity are common in ellipticals and the bulges of large spiral galaxies (e.g., Carollo et al., 1993; Davies et al., 1993; Trager et al., 2000; Peletier et al., 1990; Gorgas et al., 1990; Thomsen & Baum, 1987; Wirth, 1981), we should expect radial gradients in the UV source population as well. These gradients can be used to constrain how age and metallicity affect the stellar evolution leading to UV HP-HB stars.

M31 is an excellent target for the study of radial trends in galaxy bulges. It hosts the most massive and metal rich bulge (e.g., Ferguson & Davidsen, 1993) that can be resolved into individual UV sources (as demonstrated by Bertola et al., 1995 and B98), has a measured UVX (Burstein et al., 1988), and estimated age-metallicity gradients derived from integrated line indices (Saglia et al., 2010).

In this chapter, we present observations and analysis of the UV component of the bulge of M31, the first data imaged in the UV by the Panchromatic Hubble Andromeda Treasury (PHAT) survey (Dalcanton et al., 2012). Section 2.3 presents our observations and their comparison to those of B98. We investigate the radial properties of the UV sources and present a first broad comparison to new stellar models in Section 2.4. In Section 2.5, we discuss our findings in light of the possible causes of the UVX. Closing remarks are presented in Section 2.6.

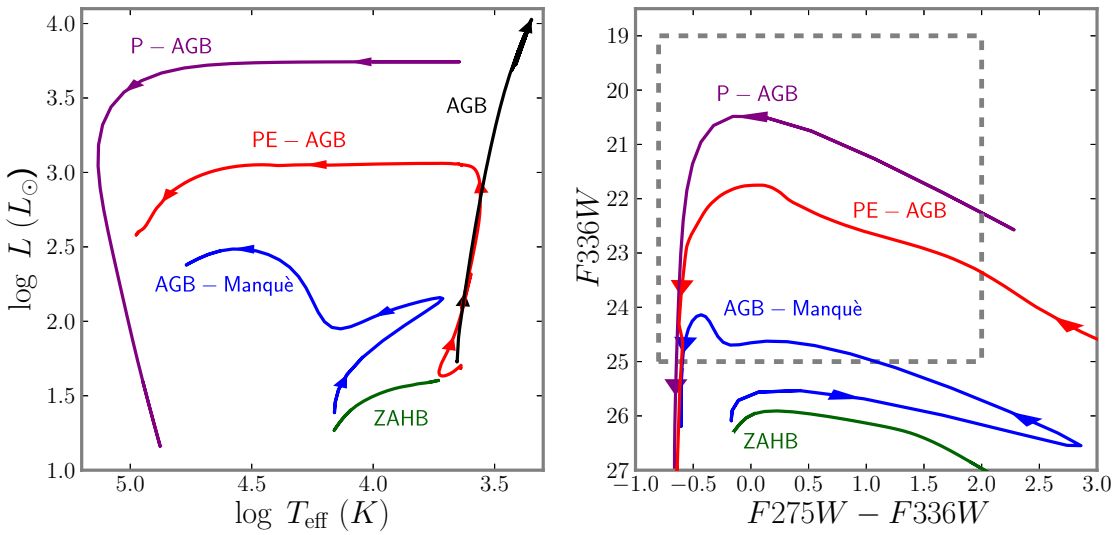

Figure 2.1 Sample stellar evolutionary tracks (Bressan et al., 2012) showing hot HB stars and their progenies' placement on HR diagram (left) and CMD in UVIS filters (right) as seen at the distance of M31 (see Section 2.4.1). Each evolutionary channel is illustrated and labeled. A canonical AGB track (black) is not shown on right panel as it is fainter than $F336W = 28$. The P-AGB track is taken from Vassiliadis & Wood (1994) H-burning tracks for a mass of 0.597 $M_{\odot}$ and Z=0.016. Dashed box shows approximate range of other CMDs in this chapter.

2.3 The Data

2.3.1 PHAT Observations, Resolved Star Photometry, Astrometry

As part of the PHAT program (GO-12058), we obtained UV imaging over a $12' \times 6.5'$ region (2.6×1.4 kpc) around the center of M31 with HST/WFC3-UVIS. The UVIS channel has a pixel size 15μm and plate scale of 0.04 arcsec/pixel. Images were taken in the $F275W$ and $F336W$ filters. Although the filters were chosen primarily for the study of massive stars in the star-forming disk, they also allow an excellent sampling of the UV-bright sources across the bulge. The area covered for this study is illustrated in Figure 2.2 and consists of a 3×6 grid of pointings with a 180° orientation flip between the two 3×3 subgrids. The UVIS fields overlap by $\sim 45''$. Two exposures were taken at each position in each filter, with a $1.9''$ dither between exposures to cover the UVIS chip gap. Total exposure times are 1010 seconds and 1350 seconds in $F275W$ and $F336W$ respectively. For complete details of the PHAT observing strategy see Dalcanton et al. (2012).

We performed point spread function photometry on all UVIS pipeline processed data (`.flt` files) in the region of interest using the software package DOLPHOT[2]. DOLPHOT is a modified version of HSTPhot (Dolphin, 2000) that has been updated to include a specialized WFC3 module. Cosmic rays were rejected from the raw images using the IDL package `lacosmic`, which masks cosmic rays based on their very sharp edges. Furthermore, our sharpness cuts (see below) removed most other cosmic rays from the photometry catalog.

We have merged the independent photometric catalog for each of the 18 pointings into a single catalog for the entire bulge. We have removed duplicate sources in overlapping regions as follows. First, given DOLPHOT's source positions and initial astrometric solution, we searched the overlapping regions for pairs of stars that are close in celestial coordinates. We used a search radius of 2 arcseconds which is large enough to compensate for HST pointing errors. We then produced a histogram of (ΔRA, ΔDec) vectors, which yielded a large but nearly uniform background of false matches plus a bump of correct matches at the RA, Dec offset between the two pointings. We measured these offsets for all pairs

[2]http://purcell.as.arizona.edu/dolphot

of pointings, then performed a least-squares fit to find the offsets and affine corrections (scales, rotations, and shears) between the pointings. By applying these corrections, we could put the sources detected in the separate pointings on a common local astrometric system. We then searched for sources that are measured in multiple pointings and merged their photometric measurements so that each star was represented by a single catalog entry. The local astrometric system was then tied to a global astrometric system by first aligning the WFC3/UVIS sources with our ACS/WFC sources, which are in turn aligned to a local reference catalog produced from CFHT imaging, which is in turn tied to 2MASS (Skrutskie et al., 2006).

The photometry output was then filtered to only allow objects classified as stars with DOLPHOT parameters `signal-to-noise` > 4, `sharp` < 0.075, `crowd` < 0.5, and `round` < 1.5 in both filters (see Dolphin, 2000, for a detailed description of each parameter).

To measure the completeness function, we performed 100,000 artificial star tests (ASTs) for each observed field, and applied the above photometric cuts to the results. We find the data to be at least 90% complete in each radial bin down to $F275W = 24.3$ and $F336W = 23.9$.We limit our analysis to this innermost 90% completeness limit to ensure that completeness is at least 90% at all radii. Completeness magnitudes are listed in Table 2.1 for each radial bin. We made one further cut to limit the contamination of hot Milky Way (MW) foreground stars by removing bright red stars with $F336W < 19$ and $F275W - F336W > 0.8$ (see Section 2.3.3).

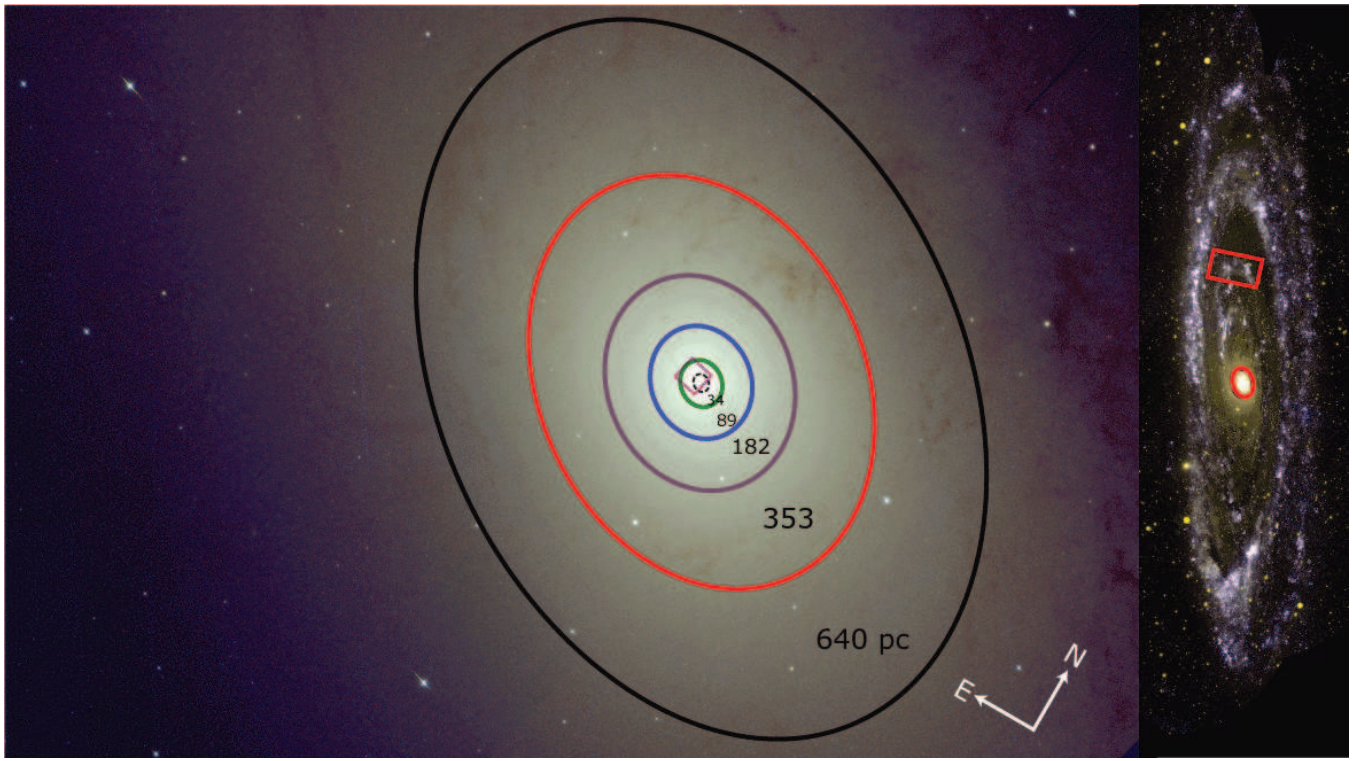

Figure 2.2 Left: *HST* $F336W$ (blue), $F475W$ (green), and $F814W$ (red) composite mosaic of M31 bulge. Elliptical contours show locations of isophotes used as analysis region boundaries. The color scheme is used in other figures in this chapter and the median radius of each isophote bin is superimposed. Data within the innermost (black dotted) region are excluded from the analysis (see Section 2.3.3). The magenta box shows the footprint of the B98 FOC imaging. Right: GALEX FUV (blue) and NUV (green) composite mosaic of M31 (Barmby et al., 2006). The red ellipse denotes the outermost (black) contour displayed in left panel. The footprint of the M31 disk field plotted in Figure 2.5 is shown as a red rectangle in right panel.

Photometry Measurements

Region	Region area (arcsec^2)	Region $a_{\rm min}$ (arcsec)	Region $a_{\rm max}$ (arcsec)	median a (arcsec)	median a (pc)	$N_{\rm stars}$	90% Comp. $F275W$	90% Comp. $F336W$	Frac Cont. $F275W$	Frac Cont. $F336W$
0	76	0.0	4.3	2.1	8.2	...	...	...	...	...
1	600	4.3	13.6	8.9	34.0	280	24.3	23.9	0.27	0.22
2	3197	13.6	33.0	23.3	88.5	607	24.4	24.0	0.12	0.14
3	9816	33.0	63.0	48.0	182.3	856	24.5	24.4	0.04	0.09
4	34422	63.0	123.0	93.0	353.2	1187	24.5	24.7	0.02	0.03
5	85143	123.0	214.0	168.5	640.0	1404	24.6	25.1	0.01	0.01

Table 2.1 Region area is of each logarithmically spaced isophote; a is the semi-major axis (see Section 2.3.3), given in minimum, maximum, and median. The median radius is calculated directly from the isophotal boundary, assuming distance modulus $(m-M)_0 = 24.47$ (McConnachie et al., 2005). $N_{\rm stars}$, are the numbers of UV-sources in each annulus (detected in both filters and brighter than the 90% completeness magnitude of the innermost bin); 90% Comp., percent completeness magnitude in each annulus. Frac Cont., fractional contamination at the 90% completeness magnitude of each annulus (see Section 2.4.4).

2.3.2 Comparison with FOC data

As a consistency check, we compared our photometry to that of B98, which carried out a comparable UV stellar population analysis, but over a much smaller area than presented here. B98's imaging was taken by the FOC in its $F175W$ and $F275W$ filters, which are suited for the detection of stars with effective temperatures up to $T_{\rm eff} \sim 40,000$ K. To compare these datasets, we began by correcting the FOC photometry to be 0.5 mag brighter, as recommended by Section 4.4.1 in Brown et al. (2000) to account for calibration revisions. We made no conversion between the FOC and WFC3 filter systems, beyond transforming the B98 data from its tabulated STMAG values into the VEGAMAG system. We then transformed the B98 catalog positions onto our astrometric system using linear shifts determined by matching bright sources ($F275W < 22$) in the similar $F275W$ passbands. Once aligned, we constructed comparison catalogs with identical spatial coverage defined by the 14" $\times$ 14" FOC field of view (see Figure 2.2) and excluded a circular 2.5" radius in the center to exclude the most crowded regions. Finally, we performed cross-catalog matching using a $\sim$ 2 pixel ($\sim$ 0.07 arcsec) search radius, and accepted matches with $F275W$ magnitude

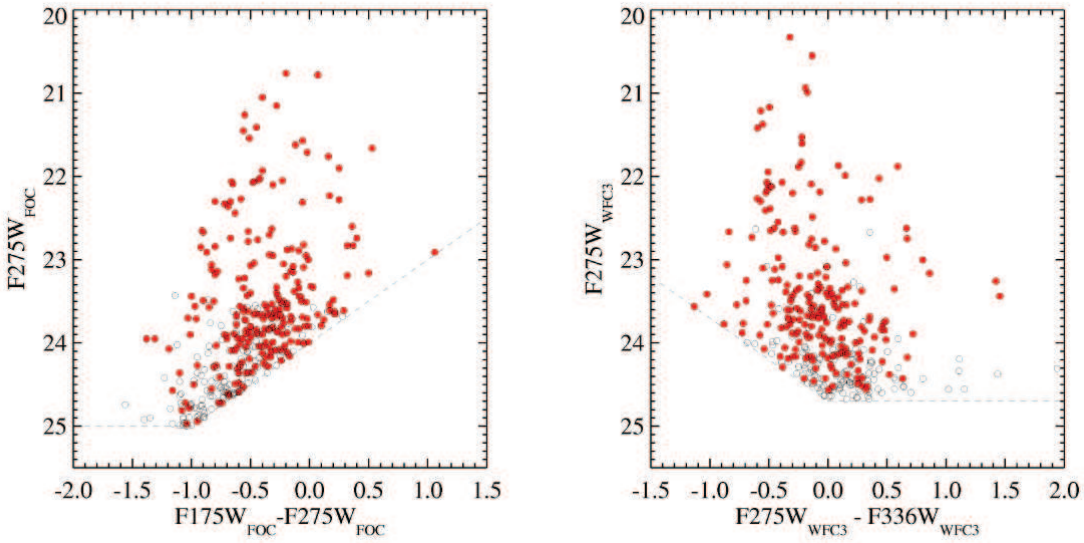

Figure 2.3 A comparison of PHAT UV and FOC spatial overlap. Left: UV CMD for the B98 dataset. The FOC sources with PHAT counterparts are shown in red (filled circles), and FOC sources without PHAT counterparts are open circles. The PHAT data appear incomplete for the bluest sources with $F175W_{FOC} - F275W_{FOC} < -0.75$. Right: UV CMD for the PHAT dataset extracted from the smaller FOC footprint of B98. Stars that have matched counterparts in the B98 catalog are plotted in red (filled circles), and unmatched PHAT sources are open circles. The completeness limit of the PHAT data is roughly 0.3 magnitudes brighter in $F275W$ than the B98 FOC observations. The dashed lines correspond to B98 detection limit.

differences < 0.7 mag. If multiple sources fulfilled the match criteria, we chose the match with the smallest magnitude difference.

The results are presented in Figure 2.3. We were able to match 65% of the B98 catalog to WFC3 sources in our catalog. A majority of the unmatched B98 sources fall in the fainter ($F275W_{FOC} > 24.5$), bluer ($F175W_{FOC} - F275W_{FOC} < -0.5$) portion of the FOC CMD, showing the B98 dataset's slightly shorter wavelength sensitivity. Overall, however, this comparison showed that these two datasets probe comparable stellar populations, with the PHAT dataset providing superior spatial coverage, and the FOC sample providing a better probe of the very hottest stars.

2.3.3 Radial Binning of UV Sources & Possible Contaminants

We divided the data into bins to analyze the properties of the UV sources as a function of radius. These bins were defined using logarithmically spaced isophotes, as measured on a 3.6μm image from Spitzer (Barmby et al., 2006). The innermost contour (semi-major axis distance of $\sim 4''$) was set to exclude the nuclear region, due to the relatively lower quality of our photometry, while the outermost contour ($214''$) was set to avoid major dust lanes and regions of recent star formation that lie along the inner arms/ring in the disk. Table 2.1 lists the properties of the bins, which are illustrated in Fig. 2.2. Their CMDs are shown in Fig. 2.4.

Because metal poor MS stars can occupy the same region of CMD space as UV-bright stars, we needed to assess potential effects of contamination on our study. We examined the contamination from the star-forming disk of M31 by comparing the radial gradients of stars in two regions of the CMD. The first CMD region was chosen to occupy the same color-magnitude space as a MS dominated disk field (galactocentric radius ~ 6.5 kpc), shown as a red rectangle in the right hand image in Figure 2.2 ($22 < F336W < 23, -0.13 < F275W - F336W < 0.28$). The second CMD region was selected to be too blue to have contamination from MS stars ($22 < F336W < 23, -0.35 < F275W - F336W < -0.50$). The stellar gradients of these regions showed a nearly constant ratio within uncertainties, indicating MS contamination from the M31 bulge is small across the analysis region. Furthermore, bulge-disk decomposition suggest that while the fraction of disk light increases five-fold between the inner and outer annuli, the disk never contributes more than 12.5%, even in the outer most analysis region (Howley et al, in prep).

There is also a possibility that some of the redder stars, ($F275W - F336W \gtrsim 0.8$; see Fig. 2.4) are hot MW foreground stars. To estimate the MW contamination we have made TRILEGAL (Girardi et al., 2005a) simulations of the MW for the field of view contained in the entire analysis region. Most of the simulated foreground stars are redder than $F275W - F336W = 0.8$ and brighter than $F336W = 19$. We excluded 69 sources brighter and redder than these limits from our analysis. Bluer and fainter than these limits, our simulations suggest a negligible contribution ($\sim$40 stars) of foreground stars with $F336W > 19$.

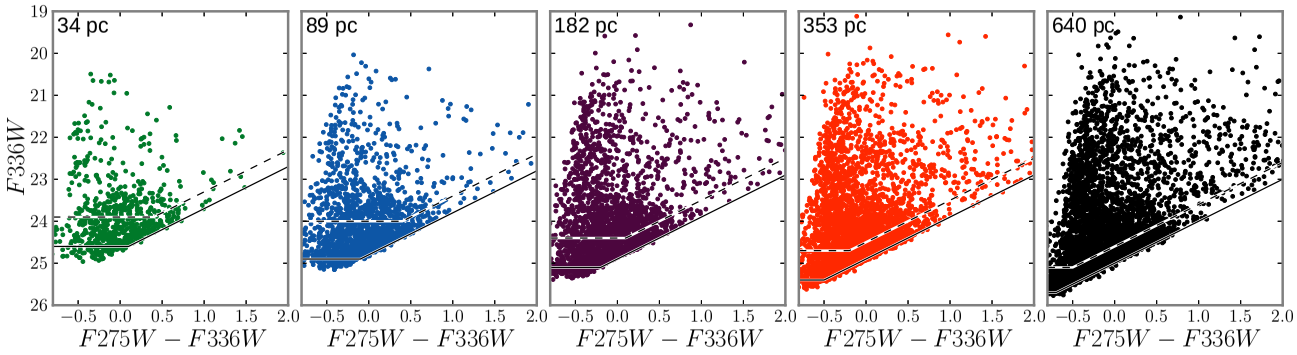

Figure 2.4 UV Color-magnitude diagrams of each analysis region. Dashed lines mark the 90% completeness limits and solid lines mark the 50% completeness limits (see Section 2.3). We limit our analysis to sources brighter than the 90% completeness limits in the innermost (green) region. The median projected radius of each distance-corrected logarithmically-spaced isophote is labeled in the upper left. The color scheme follows Figure 2.2.

2.3.4 Integrated Light and Ancillary Imaging

As a way of assessing bulk properties of the defined analysis regions, we calculated total integrated fluxes for each analysis region from the $F275W$ and $F336W$ imaging, as well as from the Spitzer/IRAC 3.6μm image. For the HST imaging, we first assembled an aligned mosaic of the UV imaging by means of the Multidrizzle task within PyRAF (Koekemoer et al., 2003) using the astrometry solution obtained from the stellar catalogs and with sky-subtraction disabled. Once we obtained this combined mosaic, we performed aperture photometry of the regions on the combined image. To estimate the sky level for the F275W and F336W mosaics, we performed photometry on outer disk images (galactocentric radius of $\sim$ 15 kpc) obtained with identical observing parameters as part of the PHAT survey and confirmed that the true sky background level is $\sim$ 0 at these very blue wavelengths. As such, there was no need for sky subtraction as part of our aperture photometry. For the Spitzer image, we used available mosaics (see Barmby et al., 2006, for details) and similarly performed aperture photometry for the analysis regions.

Table 2.2 includes the surface density of HP-HB and P-AGB stars (see Section 2.4.3 for a discussion on how the populations are separated), their resolved UV flux, the total resolved UV flux, and total integrated UV flux in each filter, in each annulus. Also tabulated is the total integrated flux within each annulus obtained from Spitzer/IRAC 3.6μm imaging ($F_{3.6\mu\mathrm{m}}$, Barmby et al., 2006) and the bulge-to-disk ratio (B/D) integrated within the radial bin using a 2D, two-component model of an exponential disk and Sérsic bulge (Howley et al., in prep).

2.4 Analysis

2.4.1 Radial Color–Magnitude Diagrams

Figure 2.5 shows a UV CMD of the inner two radial bins (15–120 pc; left panels) and a disk field (right panels, red rectangle in Figure 2.2) composed of the entire Brick 9 (galactocentric radius $\sim$ 6.5 kpc) from the larger PHAT dataset. We superimposed stellar evolutionary tracks converted to the WFC3/UVIS photometric system following the Girardi et al. (2008b) bolometric corrections updated with the latest WFC3/UVIS filter throughputs. We assumed

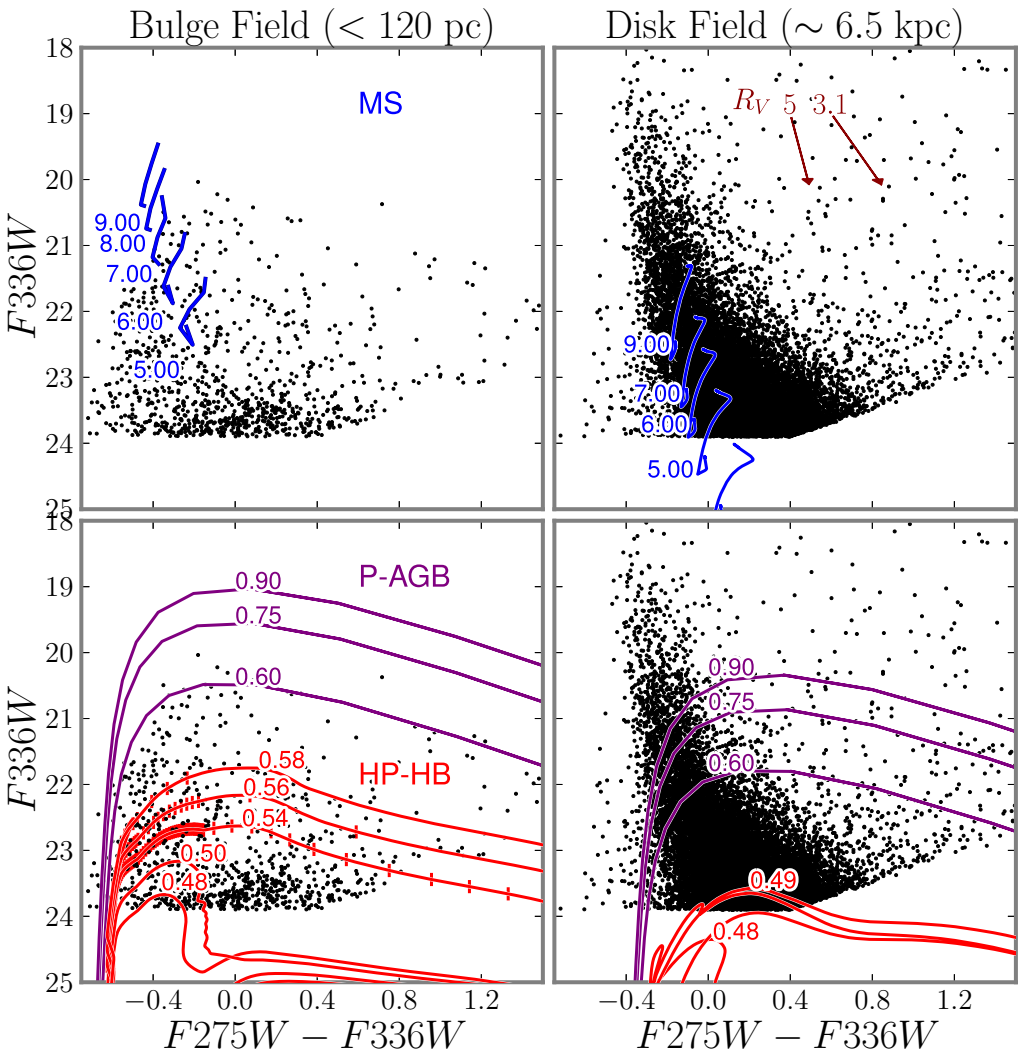

Figure 2.5 Nature of the bright UV point sources in the central bulge (left) vs. star-forming regions in the field (right). The two panels on the left show the UV CMD for stars within 120 pc of the center; the two panels on the right show CMDs of the disk field (galactocentric radius $\sim$ 6.5 kpc; see red rectangle in the right panel of Figure 2.2). These CMDs are compared to MS tracks for young massive stars in the top panels; they are compared to P-AGB and HP-HB tracks for evolved stars in the bottom panels. It is apparent that the (reddened) MS tracks are a good match for the disk CMDs, but not the bulge (see Section 2.4.1). Markers are placed on the three most massive HP-HB tracks at 10^4 yr intervals. Two reddening vectors with $R_V = 3.1$ and 5 are also shown for 1 magnitude extinction in $F336W$. MS tracks assume $A_V = 0.99$ (Kang et al., 2009) and bulge tracks assume a pure MW foreground extinction of $A_V = 0.206$ (Schlegel et al., 1998).

a distance modulus of $(m-M)_0 = 24.47$ (McConnachie et al., 2005). When plotting young MS tracks, we adopted an interstellar extinction of $A_V = 0.99$ for the disk field, based on the median E(B-V) value from Kang et al. (2009) for star forming regions in the disk analysis field. Although we are not currently able to derive the foreground interstellar extinction for the bulge, we adopted the value from Schlegel et al. (1998), $A_V = 0.206$. These A_V values were converted into the $F275W$ and $F336W$ extinction values using the coefficients $A_{F275W}/A_V = 2.05$ and $A_{F336W}/A_V = 1.67$ derived from the Cardelli et al. (1989) and O'Donnell (1994) (shortward of U-band) extinction curve with $R_V = 3.1$ applied to a $T_{\rm eff} = 15,000$ K star.

The evolutionary tracks come from two sources: Vassiliadis & Wood (1994) for H-burning P-AGB stars of masses $> 0.6\ M_{\odot}$with $Z = 0.016$ and $Y = 0.25$ and the most recent Padova library (Bressan et al., 2012) for the HP-HB stars[3]. For the latter, the chemical composition is either $Z = 0.07$ and $Y = 0.389$ with an α-enhanced composition typical of bulges (adapted from Bensby et al., 2010) for the bulge field (left panels), or $Z = 0.02$ and $Y = 0.285$ with solar-scaled composition for the disk field (right panels). The metallicity chosen for the bulge is an extreme case to allow for high Helium content. It may be possible to populate the EHB and its progeny in similar CMD space with evolutionary tracks of lower metallicity by increasing mass loss rates. . The calculations for the tracks plotted in Figure 2.5 include **all** kinds of single stars that can give rise to UV-bright stars, namely the younger MS, the intermediate-age Post-AGBs, and the old EHB and HP-HB stars.

It is evident from the left panels of Figure 2.5 that the CMD of the inner 15–120 pc of the bulge shows quite different characteristics than the disk CMD in the opposing panels. The disk field shows a well populated diagonal sequence that is mostly redder than $F275W - F336W = -0.3$ and that becomes systematically redder at fainter magnitudes. In contrast, the bulge contains a significant population of stars bluer than $F275W - F336W = -0.3$ that does not appear to be an under-populated version of the disk field.

Comparing to models, the stars in the young, star-forming disk match the solar MS evolutionary tracks, as expected. However, the higher metallicity MS tracks fail to match

[3]P-AGB stars with masses $M > 0.9M_{\odot}$ are not included in Figure 2.5 because their progenitors are too massive and short-lived, and thus not expected in the bulge.

the bulge population – with its wide spread in the CMD for $F336W < 23$, and its remarkable concentration of stars at $F336W > 23$ – indicating that the UV-bright stars in the bulge are not primarily MS stars. In contrast, the HP-HB stellar evolutionary tracks provide a good match to the bulge, but fail to match the disk population. This match suggests that the UV-bright stars in the bulge are primarily a mix of PE-AGB and fainter AGB-manqué stars (red tracks in Figure 2.5, red and blue tracks, respectively, in Figure 2.1). While more luminous P-AGB stars (purple tracks in Figures 2.1 and 2.5) with masses $> 0.6 M_{\odot}$ could potentially be detected, in practice their evolution is sufficiently fast that they make no significant contribution to the UV CMD.

If we examine the CMDs across the entire bulge (Figure 2.4), there is a clear radial trend. The number of stars brighter than $F336W \simeq 23$ decreases towards the center as does the area of each isophotal region. Dimmer stars, however, do not show this trend, and in fact, their numbers remain high at all radii. Both of these trends are probably driven by changes in the relative proportions of P-AGB and HP-HB stars, which in turn depends on the changes in the progenitor stars as a function of radius (though the P-AGB do not contribute to the faint gradient). We analyze these trends more extensively below.

2.4.2 Radial Luminosity Functions

Figure 2.6 shows the luminosity functions (LF) for contaminant-corrected (see Section 2.3.3) resolved UV sources within our adopted annuli. We removed the effects of changing radial stellar density by scaling the LF by each region's stellar mass. We estimated the stellar masses from the integrated 3.6μm flux (Barmby et al., 2006), which should scale linearly with stellar mass, up to a multiplicative constant.[4] Following the procedure of Barmby et al. (2006), we assumed an optical bulge color of $B - R = 1.8$ (Walterbos & Kennicutt, 1987), a K-band M/L ratio of 1.09 derived using the color-dependent relations from Bell & de Jong (2001), and 3.6μm to K-band M/L ratio conversion from Oh et al. (2008), resulting in an 3.6μm M/L ratio of 0.95. In Figure 2.6 we made completeness corrections to see

[4]Isochrones from Girardi et al. (2010, and ref. therein) confirm that the expected 3.6μm mass-to-light ratio does not change significantly for stellar populations of ages older than $\sim$ 4 Gyr and metallicities Z$>$ 0.001.

if each LF peak was not simply a manifestation of incompleteness of the data. To do so, we removed our magnitude limit criteria (see Section 2.3) and divided the sources of good quality detected in both filters by the completeness fraction found from the ASTs in 0.2 magnitude bins.

The LFs look similar at bright magnitudes for all radii, but show significant radial variations at fainter magnitudes. First, we see a dramatic trend at faint magnitudes where faint HP-HB stars ($F275W,\ F336W > 23$) become increasingly abundant in the inner bulge, relative to the overall stellar mass. Second, we see a weaker trend for stars with magnitudes between $21 - 23$, which also show increasing contributions toward the inner bulge. These are likely P-AGB stars of a continuous distribution of masses less than $\sim 0.6 M_{\odot}$, suggesting that the outer regions are under-abundant in P-AGB stars.

To help interpret these results, we overlay a synthetic LF (dotted in Figure 2.6) made of low-mass $Z = 0.07, Y = 0.389$ tracks from the Padova stellar evolution library (Bressan et al., 2012) evolved from the ZAHB, assuming that the mass distribution of stars along the ZAHB is flat for all ZAHB masses below 1.0 $M_{\odot}$. This approximation is reasonable since the range of ZAHB masses that actually contributes to the LF is very narrow ($\sim 0.45 - 0.58 M_{\odot}$).

The simulated Helium-burning LF reproduces the shape and color of the bump in the LF fainter than 22.5 mag, especially for the inner M31 radial bin. This bump can therefore be interpreted as being made by the HP-HBs. Deeper observations would likely reveal a much larger bump in the LF due to the EHB.

In addition, the flux density from the detected stars does not vary with magnitude except for the inner region. Essentially all stars between 20 and 24 in both $F275W, F336W$ contribute equally to the flux density with the exception perhaps of region 1, where the contribution tends to increase towards fainter magnitudes.

2.4.3 Luminosity Contribution of HP-HB and P-AGB

Although P-AGB and HP-HB stars are individually bright in our UV bandpasses, together they only make up a small fraction of the integrated UV light ($< 2\%$ in $F275W$). A vast majority of the UV light must be emitted by fainter populations, such as EHB stars that

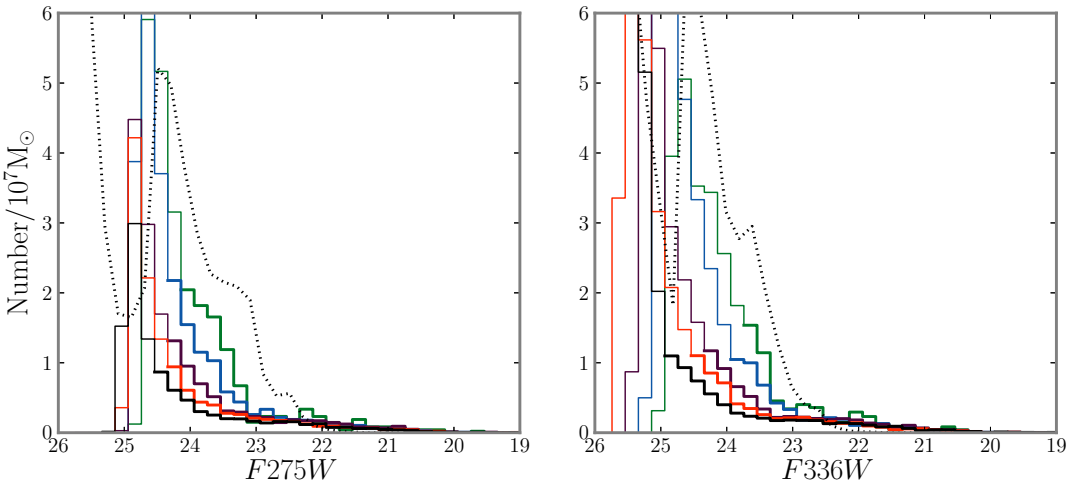

Figure 2.6 Number of resolved HP-HB stars (left panel: $F275W$; right panel: $F336W$) as a function of magnitude, scaled by each region's stellar mass found by the 3.6μm M/L ratio (see Section 2.4.2), in bins of 0.2 magnitudes. The observed LFs are corrected for completeness and shown with thin lines fainter than the 90% completeness magnitude in the respective annulus (i.e., a correction by more than a factor of 1.1). The color scheme is the same as Figure 2.2, with green indicating the innermost bin. Long lived HP-HB stars are shown in model LF (dotted) evolved from the ZAHB with a flat distribution of mass below 1.0$M_\odot$, and the Z=0.07 Y=0.389 tracks (cf. Figure 2.5). The model is normalized to the innermost region's peak LF in $F275W$. The over-abundance of stars with $F275W > 23$ in the innermost regions of M31 are associated with HP-HBs. The bright LF tails are due to a seemingly flat distribution of P-AGB stars (see Section 2.4.5). The increase in the model LF at faint magnitudes ($\gtrsim 24.5$) is due to numerous HB stars, of which the hottest likely dominate the UVX.

remain undetected in our resolved photometry.

Since the P-AGB and HP-HB stars we detect are a very small fraction of the UV light (see Table 2.2), the total integrated UV flux must be coming from some other population of fainter, but more numerous stars. Our model LF suggests a large population of EHB stars fainter than mag ~ 25. These stars are likely the main source of the UVX (c.f., B98). These stars could be detected with deeper UVIS observations and with bluer filters, provided that the crowding limit was sufficiently faint to detect these numerous stars.

To further quantify the radial gradients of stellar populations, we divided UV-bright stars into HP-HB and P-AGB stars. We separated the HP-HB stars from P-AGB stars using the highest mass evolutionary track that produces a HP-HB star at $Z = 0.07$ and $Y = 0.389$ ($M = 0.58 M_{\odot}$; see the brightest red track in the bottom left panel of Figure 2.5) for the Padova stellar evolution library. More massive evolutionary tracks than this critical mass produce stars with enough envelope mass to become canonical AGB stars; this behavior has little metallicity dependence, and does not appear to change with He-abundance from $0.26 < Y < 0.46$ (Bressan et al., 2012). We have classified stars brighter than this track as P-AGB. As a faint limit of UV-bright stars, we use our innermost region 90% completeness magnitude (see Section 2.3).

The left panel of Figure 2.7 shows the surface brightness profiles of the HP-HB, P-AGB, and integrated UV light. In both filters, the surface brightness increases toward the center for both HP-HB and P-AGB. The right panel of Figure 2.7 shows the ratio of resolved UV stars, and indicates that the flux from HP-HB stars increases with respect to the P-AGB.

A best fit Sérsic profile from Courteau et al. (2011) is overplotted on the left panel of Figure 2.7, with arbitrary normalization in surface brightness. Courteau et al. (2011) fit $UVBRI$, $2MASS$, and Spitzer IRAC surface brightness profiles of M31 to find the Sérsic bulge index of $n = 2.2 \pm 0.3$ and effective radius of $R_e = 1.0 \pm 0.2$ kpc. We did a simplistic least-squares fit to a Sérsic profile using the surface brightness of our total integrated light in $F336W$ imagery to find $\mu_{e_{F336W}} = 21.7$ mag/$\prime\prime^2$, $n_{F336W} = 2.4$, and $R_{e_{F336W}} = 2.1$ kpc. These numbers are consistent with the steeper scaled gradient in UV sources.

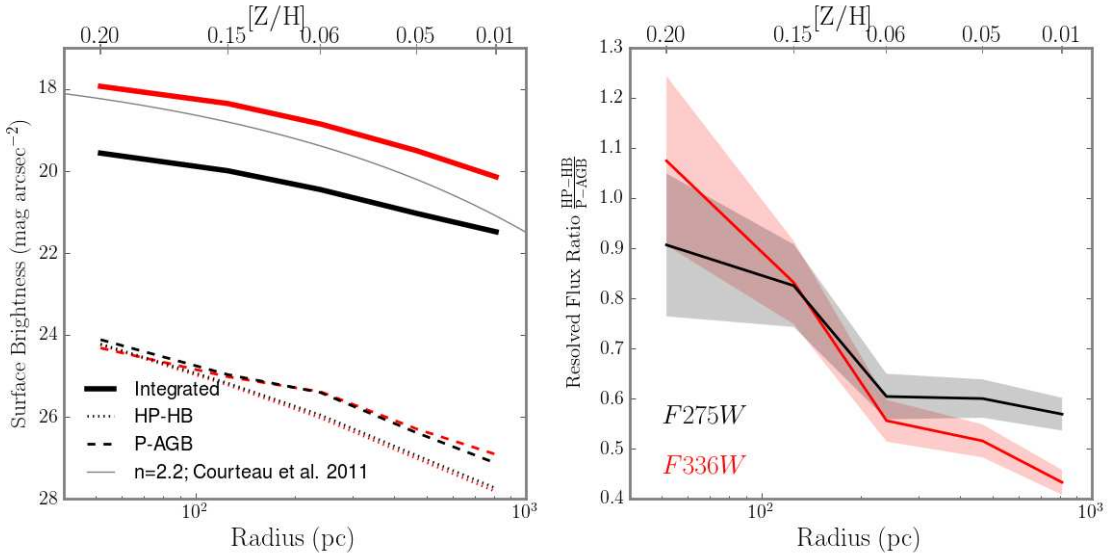

Figure 2.7 The radial distribution of UV sources. Left Panel: Surface brightness as a function of radius of $F275W$ (solid, black), $F336W$ (solid, red), HP-HB (dotted), and P-AGB(dashed). The best fit Sérsic profile from Courteau et al. (2011) is overplotted with μ_e shifted to $F336W$=23 (gray). Right Panel: Resolved flux ratio of HP-HB to P-AGB stars in each filter for each annulus. Shaded regions show Poisson uncertainty in number counts. In both panels, red denotes the $F336W$ filter and black denotes the $F275W$ filter. The characteristic metallicity as a function of radius reported by Saglia et al. (2010) is indicated on the top axes. Both the HP-HB and P-AGB populations increase toward the nucleus of M31, but the HP-HB stars show a dramatic increase in flux with respect to the P-AGB stars in the innermost regions.

2.4.4 Possible Contributions from Stellar Blends

The bulge of M31 has a strong surface brightness gradient in the UV, which must be due to a dramatic increase in the number density of stars towards the center of the galaxy. As we show in Table 2.2, the majority of these stars are unresolved in our observations, but they could possibly lead to the detection of spurious sources, if sufficient numbers of the fainter stars were blended together to rise above our detection threshold. These spurious sources would dominate at fainter magnitudes and would be expected to show a strong radial gradient due to the increased crowding in the center, and thus could potentially mimic our observed gradient. While we have minimized the likelihood of this contamination by excluding the most crowded regions of the bulge and by choosing a relatively bright limiting magnitude for our analysis ($F336W = 23.9$, $F275W = 24.3$), it is still worthwhile to confirm that this issue is not affecting our conclusions.

We have ruled out this possibility by considering two different cases. For the first, we assume that the luminosity function observed at bright magnitudes continues as a power-law to faint magnitudes. This assumption puts large numbers of stars just below the detection threshold, where the chances are maximized that a star will blend with an undetected source and rise above the detection threshold. We then simulate the observed luminosity function as follows. In a series of magnitude bins, we randomly select stars from the same catalog of artificial stars used to calculate our completeness limits. The number of stars drawn in each magnitude bin is determined by our assumed power-law luminosity function. We then use the recovered properties of the artificial stars (i.e., the magnitudes the stars were recovered with, and if they were detected at all) to generate the luminosity function that would be observed. Figure 2.8 shows the input and recovered luminosity function in each of the radial bins, plotted as black and colored lines, respectively. As expected, blending leads there to be an artificial upturn in the luminosity function as one approaches the detection limit, with the effect being more dramatic in the most crowded inner annulus. However, these effects only become appreciable below our adopted magnitude cuts (vertical dashed lines). At our adopted analysis limit of $F336W = 23.9$ and $F275W = 24.3$, the observed luminosity function never has more than 27% contamination from blends (see Table 2.1 for

exact contamination levels in each bin). Given that the luminosity function is observed to vary a factor of 100, it is unlikely that the observed radial trend is produced by radially-dependent blending from a power-law luminosity function.

We have also considered a second, somewhat less likely source of blends. It is believed that the majority of the unresolved flux in our images comes not from sources just below our detection threshold, but from a large population of long-lived EHB stars (e.g., B98) that are more than a magnitude fainter than our detection threshold. If so, these sources must have a very high surface density, which could sometimes lead to multiple EHB stars blending together within a single resolution element. Assuming a typical EHB magnitude of $F336W = 26.5$ (Bressan et al., 2012), and a surface brightness of $\sim$18 magnitudes arcsec^{-2}, we can calculate the mean number of EHB stars per square arcsecond. Adopting this mean, we can then calculate the Poisson probability that there will be a sufficiently large upward fluctuation in the local density (within the HST resolution element) to produce a spurious source at $F336W = 24$. We then multiply by the number of independent resolution elements to calculate the contamination in the inner most annulus. When we do so, we find that we expect no more than 0.1 spurious stars brightward of $F336W = 24$, in contrast to the 164 stars found between 23.5 and 24 magnitudes in region 1. We therefore rule out blends from EHB stars as a significant source of contaminants to the observed luminosity function.

These two tests indicate that it is highly unlikely that false blended sources are significant contaminants brighter than the magnitude limit we adopted for our analysis.

2.4.5 Comparison to Other Evolving Populations

Figure 2.7 establishes that the resolved flux of HP-HB increases with respect to the P-AGB sources toward the nucleus. We now look in depth at the radial variations of these populations and expand the discussion to include other stellar populations.

The HP-HB sources discussed here are not the first population of astrophysical sources to show enhancement towards the inner regions of M31's bulge. In their study of Chandra X-ray point sources, Voss & Gilfanov (2007b) show an increase in the low-mass X-ray binary (LMXB) population at small radii within the bulge of M31. These authors conclude that

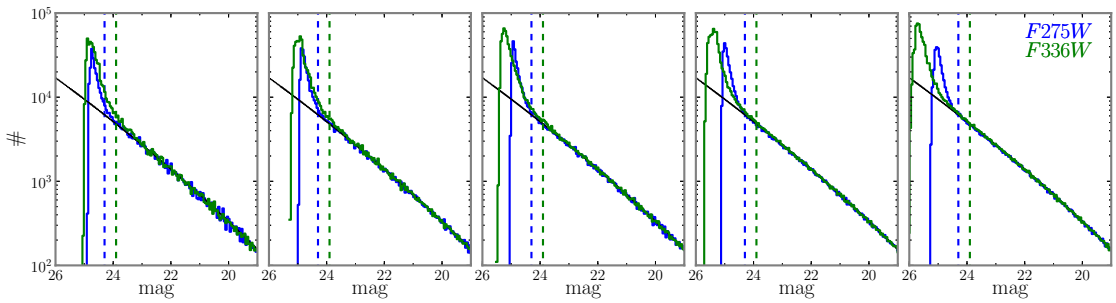

Figure 2.8 Input (black) and recovered (blue: $F275W$; green: $F336W$) luminosity functions in each of the radial bins. Close to the detection limit, blending causes an artificial upturn in the luminosity function. The effect only becomes appreciable below our adopted magnitude cuts (dashed lines) and is never above 27% (see Table 2.1 for exact values in each radial bin).

this enhancement can be accounted for by a population of dynamically produced LMXBs, which explains why the distribution's profile follows the square of the stellar density (ρ_*^2).

For comparison, we binned the X-ray sources from the Voss & Gilfanov (2007a) catalog according to our analysis regions, excluding those sources that are either identified as non-LMXBs or that are associated with globular clusters (as their origin is different than that of unclustered LMXBs). The resulting number density distributions for the LMXBs are shown in Figure 2.9. We find the intriguing result that the excess in UV-bright sources is consistent with the power law index of the LMXBs.

We have also evaluated the radial trends in the density of PNe, as these stars are likely descendants from the P-AGB populations and might be expected to show a similar radial trend. We use the Merrett et al. (2006) catalog of 2615 PNe in M31 detected by 5007Å emission and find that the distribution of PNe across the bulge is roughly constant with radius, and does not follow the trends of HP-HB, P-AGB, or LMXBs. However, the Merrett catalog is not expected to be complete in the innermost regions. If the true radial distribution of PNe does follow the gradient in the P-AGB population, then the inner regions must be incomplete by a factor of ~ 5.5. We discuss the implications of these results in Section 2.5 below.

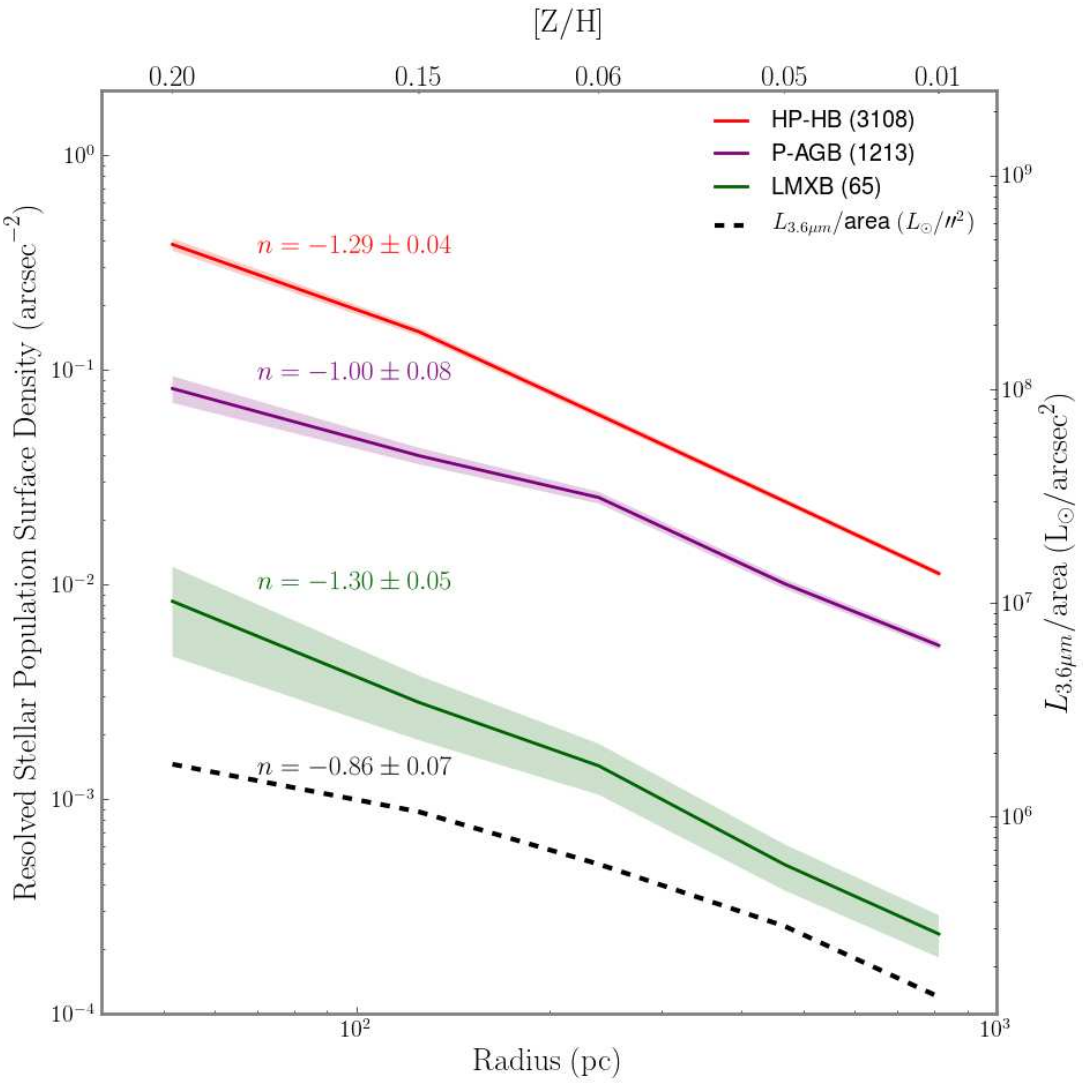

Figure 2.9 Surface density of UV-bright sources (blue = HP-HB, red = P-AGB), LMXBs (green, Voss & Gilfanov, 2007b), binned according to analysis region with Poisson uncertainties. The 3.6μm luminosity (black dashed) is plotted in different units and follows the right axis. The characteristic metallicity as a function of radius reported by Saglia et al. (2010) is indicated on the top axis. The least-squares fit power law index of each stellar component is noted above its profile with its uncertainty in the fitting. HP-HB (blue) and P-AGB (red) stars follow a different surface density profile than that of the 3.6μm light. However, the HP-HB stars seem to follow a profile consistent with the LMXBs.

Radial Gradients

Region	B/D	$F_{3.6\mu m}$	Integrated Flux		Resolved Flux		HP-HB Resolved Flux		Surface Density	
			$F275W$	$F336W$	$F275W$	$F336W$	$F275W$	$F336W$	HP-HB	P-AGB
		(Jy)							(arcsec^{-2})	(arcsec^{-2})
0	40.7	0.27	...	...	...	...	...	...	...	...
1	40.7	1.16	25.26	98.33	0.96	0.75	0.46	0.39	0.383	0.082
2	33.5	3.74	89.77	351.08	2.23	1.85	1.01	0.84	0.150	0.040
3	20.7	6.77	181.40	681.08	4.01	3.45	1.51	1.23	0.062	0.025
4	12.0	12.99	373.58	1315.45	5.70	5.12	2.14	1.74	0.024	0.010
5	7.0	16.71	608.05	1802.78	6.96	6.73	2.52	2.03	0.011	0.005

Table 2.2 First two columns are the same as in Table 2.1, followed by B/D, the bulge-to-disk ratio of luminosity within each annulus (Howley et al., in prep); $F_{3.6\mu m}$, region integrated flux within each annulus obtained from Spitzer/IRAC 3.6μm imaging (Barmby et al., 2006). Next are integrated and resolved flux measurements in each UVIS filter, followed by the resolved flux of HP-HB stars. All UVIS fluxes are in units of 10^{-15} erg cm^{-2} s^{-1} Å^{-1}. Finally, the surface densities of the resolved UV-bright populations are tabulated (cf. Figure 2.9).

2.4.6 Stellar Population Lifetimes Inferred from Observations

Now that we have detected gradients in HP-HB stars, it is useful to make a rough estimate of what fraction of stars are expected to become UV-bright through this channel as a function of radius. Renzini & Buzzoni (1986b) provided a powerful tool to relate the number of evolved stars in a population to their lifetimes, with only a few conservative assumptions. Using the fact that most fuel is consumed by stars fusing Hydrogen or Helium, and that the initial mass function is not too steep, they relate the number of stars, N_j; in any evolved state, j, to the average amount of time (in years) the star spends in that state $\langle t_j \rangle$:

$$N_j = L_T B(t) \langle t_j \rangle \ , \tag{2.1}$$

where L_T is the total bolometric luminosity of the stellar population in $L_\odot$ and $B(t)$ is the rate of stars leaving the MS in units of ${L_\odot}^{-1}$ yr^{-1}.

Equation 2.1 is strictly valid only for a stellar population of single age and metallicity that happens to contain HP-HB stars. Any subregion of the M31 bulge, instead, is likely to contain a range of populations, with some spread in their ages and metallicities. Since just a fraction f of these populations will likely produce HP-HB stars (e.g. the oldest, most

metal rich, and/or of highest Helium content), equation 2.1 can be conveniently re-written as

$$f = \frac{N_{\rm HP-HB}}{L_T B(t) \langle t_{\rm HP-HB} \rangle} \ , \tag{2.2}$$

where $f \equiv \frac{N_{\rm HP-HB,obs}}{N_{\rm HP-HB,pred}}$. This equation can be solved for f, allowing us to solve for the fraction of evolving stars that pass through the HP-HB channel.

We have previously measured $N_{\rm HP-HB,obs}$, as listed in Table 2.2. We also adopt a value of $B(t) = 2.2 \times 10^{-11} {L_\odot}^{-1} {\rm yr}^{-1}$, derived from solar metallicity evolutionary models. This number should be accurate to 10% for populations 10 Gyr and older (Renzini & Buzzoni, 1986b). For the average time in the observed state, $t_{\rm HP-HB}$, we calculated the mean CMD crossing time of the relevant Padova stellar evolution tracks shown in figure 2.5 to find $\langle t_{\rm HP-HB} \rangle \sim 2 \times 10^6$ yr for the HP-HB.

To calculate L_T, we convert the 3.6μm flux (corrected to exclude any disk contamination using B/D; see Table 2.2) to bolometric luminosity. As mentioned above, 3.6μm flux traces the stellar population of the bulge, modulo a bolometric correction:

$$L_T = L_{3.6\mu{\rm m}} \times \frac{L_{\rm bol}}{L_{3.6\mu{\rm m}}} \ . \tag{2.3}$$

We calculated the bolometric correction by simulating the integrated light of simple stellar popultations over a range of ages and metallicities using isochrones from Girardi et al. (2010, and references therein). As mentioned in passing in Section 2.4.2, isochrones from Girardi et al. (2010) confirm that the expected 3.6μm flux of star light does not change significantly for stellar populations of ages older than ~ 4 Gyr and metallicities Z$>$ 0.001.

With the bolometric correction, BC = 2.60 and adopting $\rm M_{\odot,bol} = 4.77$ and $\rm M_{\odot,3.6\mu m} = 3.24$ (Oh et al., 2008), we converted $L_{3.6\mu{\rm m}}$ to L_T,

$$\frac{L_{\rm bol}}{L_{3.6\mu{\rm m}}} = 10^{-0.4({\rm M_{\odot,bol}} - {\rm M_{\odot,3.6\mu m}} - {\rm BC})} = 2.7 \ . \tag{2.4}$$

Combining equations 2.2, 2.3, and substituting the values above for $B(t)$ and $\langle t_{\rm HP-HB} \rangle$, we solve for f,

$$f = 1.7 \times 10^3 \frac{N_{\rm HP-HB,obs}}{L_{3.6\mu{\rm m}}} \ . \tag{2.5}$$

Substituting in numbers from Table 2.2, we plot f as a function of radius (Figure 2.10). We find that the fraction of stars that go through the HP-HB channel is small, but that the fraction increases systematically towards the center of M31. Figure 2.10 shows that nearly 3% of the MS turnoff (MSTO) stars in the innermost regions of M31 become HP-HB stars. This implies that 97% of the MSTO stars become canonical P-AGB stars. In contrast, in the outermost regions of the bulge, fewer than 1% of MSTO stars become HP-HB stars. Note that these $\sim$3% of HP-HB stars appearing as bright resolved UV sources belong to the same population of the fainter EHB stars that, according to evolutionary models, do make a large fraction of the unresolved UV light (see Section 2.4.3).

The fraction of stars that go though the HP-HB channel in the innermost regions is consistent with what is found in M32 by Brown et al. (2008). Our findings are also consistent with Brown et al. (1997), who demonstrated that galaxies with moderate UVX have about 2% of the main sequence population passing through the EHB.

This test has shown that, even in the center of M31, very few stars from the bulge population are necessary to become HP-HB and explain the UV-bright stars we detect. What causes an RGB or EHB star to eventually become a HP-HB star only affects a small percentage of the underlying stellar population, but that small likelihood varies strongly with radius, for reasons we discuss below.

2.5 Discussion

Our LFs and CMDs allow us to confirm B98's claim that HP-HB stars are the likely evolutionary channel for the production of most of the UV-bright stars in the M31 bulge. However, $\sim$ 20% of brighter UV stars in the inner two radial bins (15–120 pc) are compatible with P-AGB tracks (see Figure 2.9), expected for stars with negligible mass loss on the RGB.

We detect clear gradients in the number and types of UV-sources. We see a steep gradient at faint magnitudes ($F275W,\ F336W \gtrsim 23$) that likely arises from an increase in the HP-HB population towards the center of the bulge. These faint stars contribute about 60% of the resolved flux of the inner two radial bins in both $F275W$ and $F336W$ (see Table 2.2) and roughly 2% of evolving MS stars pass though this long-lived HP-HB channel

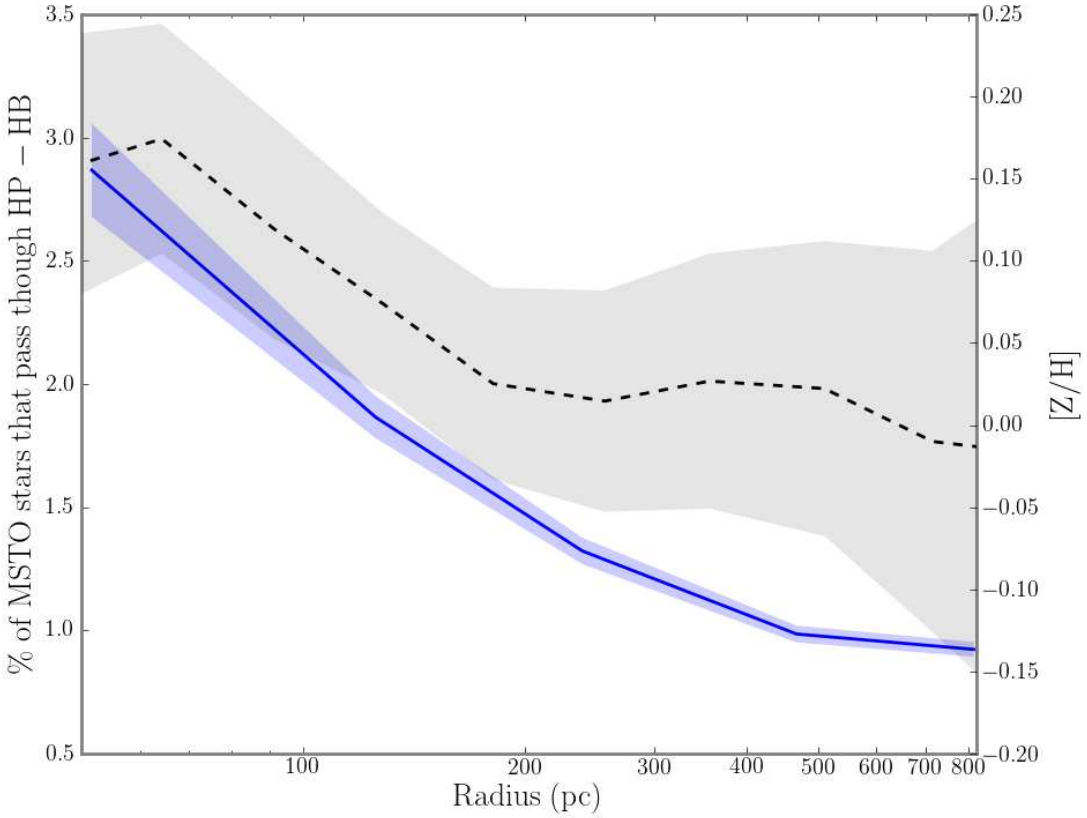

Figure 2.10 Population variations in the central ~ 0.5 kpc of M31. Shown (solid, blue) is the inferred fraction of evolving MS stars that must go through the HP-HB channel to explain the HP-HB number count profile, given the integrated light properties. This fraction rises by about a factor of 3 towards the center. Shaded regions denote Poisson uncertainty. The Lick-Index based metallicity and its dispersion derived by Saglia et al. (2010) is shown on the right axis (dotted, black).

before becoming white dwarfs (see Figure 2.10), the remainder pass though the short-lived P-AGB. However, the detected stars only make up ∼2% of the total flux in the $F275W$ filter indicating that we have not yet detected the stars directly responsible for the UVX. These missing stars are likely to be faint EHB stars, as suggested by B98.

We now outline possible causes of the detected radial gradients of HP-HB stars.

2.5.1 Gradients in Stellar Ages

The UVX is expected to increase with time for an aging stellar population. As a population ages, the mass of the MSTO will decrease, so for a fixed RGB mass loss rate, the older (i.e., less massive) stars will have smaller post-RGB envelope masses and thus will be hotter HBs. As a result, the UVX has been proposed as a possible age indicator for the centers of elliptical galaxies (Greggio & Renzini, 1999; Bressan et al., 1994; Yi et al., 1999). Bressan et al. (1994) found that the EHB and AGB-manqué stars power the UV flux of a high mass galaxy at ages older than $\sim 7.6 \times 10^9$ yr. A negative age gradient across the M31 bulge could therefore potentially explain the gradient in HP-HB stars we measure.

There is, however, no obvious evidence for an age gradient in the bulge of M31. Saglia et al. (2010) constrained the stellar populations in the inner bulge of M31 using spline-interpolated Lick indices models with α-element overabundances (Thomas et al., 2003), assuming simple stellar population models(Maraston, 1998, 2005a) and a Kroupa (2001) IMF. They found the age of the bulge (over the regions we analyze) to be consistent with the age of the universe, with no significant radial gradient. If anything, the mean ages from Saglia et al. (2010) suggest a positive age gradient with radius (i.e., older stars at larger radii), which is in the opposite sense of what is needed to produce the observed HP-HB gradient.

Another age effect is expected if the UVX is not from EHB stars and their progeny at all, but is instead from binary stars. This is an attractive explanation for why the surface density profile of LMXBs matches that of the HP-HB stars in Figure 2.9. Studies by Han and others (Han et al., 2002, 2003; Han et al., 2007, and references therein) present detailed synthetic SEDs that include three binary star evolutionary channels: common envelope, Roche lobe

overflow, and merging He white dwarfs. Over time, stars in these models will power the UVX. However, if this is the case, all old populations should have a UVX, which they do not (e.g., O'Connell, 1999). Alternatively, the lack of a central peak of PNe may suggest an alternate channel of P-AGB evolution in the central regions, such as AGB-manqué or PE-AGB, which in turn produces a central peak in the HP-HB stars. These conclusions should be considered tentative in light of the likely incompleteness of the Merrett et al. (2006) PNe catalog in this region of M31.

2.5.2 Galactic Metallicity Gradient

Negative radial metallicity gradients are common features of ellipticals and large spiral bulges (e.g., Roediger et al., 2011; Jablonka et al., 2007; Papovich et al., 2001; Kobayashi & Arimoto, 1999; Davies et al., 1993) with typical values of $\Delta[\mathrm{Fe/H}]/\Delta\log(r) \sim -0.3$ for ellipticals. Metal-rich stars are linked to more mass loss on the RGB (Greggio & Renzini, 1990) which result in smaller HB envelopes and thus hotter stars and more UV flux. Thus metallicity gradients may influence the fraction of stars that enter the EHB phase at each radius.

Support for the importance of RGB mass loss in producing the UVX population comes from Kalirai et al. (2007), who found that the white dwarfs of the metal-rich old open cluster NGC 6791 ([Fe/H]$\sim +0.4$, $t = 8$ Gyr) are under-massive due to the enhanced mass loss of their progenitors. The same cluster hosts a significant population of very hot Helium burning stars, which, although only 30% of all HB stars, would be sufficient to produce a UV excess. Dorman et al. (1995); Buzzoni & González-Lópezlira (2008) found with synthetic population models that only $\sim 20\%$ of HB stars need to be hot to explain the UV upturn, in agreement with the NGC 6791 observations.

The small fraction of evolving MS stars that go though the HP-HB channel could be explained by a galactic metallicity gradient if the HP-HB are indeed the result of extreme mass loss, and the mass loss depends on metallicity. Saglia et al. (2010) found that the metallicity in the bulge of M31 decreases by 0.2 dex every decade in radius, from [Z/H] ~ 0.4 in the center to solar at $\sim 100''$ (see Figure 2.10). In the inner regions of M31,

it is reasonable to assume that the bulk of the stars will have metallicities that sample the metallicities reported by Saglia et al. (2010), but that there will also be a tail to high metallicities. If metallicity variations drive the gradient in HP-HB stars, then the HP-HB population must result from this high metallicity tail, to avoid more than ∼3% of stars passing through the HP-HB channel (i.e., Figure 2.10).

Ancillary support for metallicity gradient being the driver of UV-bright star production can be found in Figure 2.11, where we plot GALEX $FUV-NUV$ vs. radius, along with the metallicities derived by Saglia et al. (2010). The $FUV-NUV$ color should track the relative strength of the EHB (see GALEX globular cluster CMDs in Schiavon et al., 2012). It is clear that there is a sharp upturn in [Z/H] exactly where the $FUV-NUV$ colors become extremely blue. This anti-correlation suggests that the radial variation in the numbers of UV-bright stars follows the galactic metallicity gradient.

An alternative metallicity-dependent explanation for the UV excess is through production of low metallicity ($Z < 0.008$) MSTO stars of intermediate age, which emit a large amount of their flux in the NUV. If these stars were responsible for the UV flux we detect, we would expect the UV flux to fall toward the center, due to the increased metallicity. In fact, we see the opposite gradient, the UV flux increases toward the center (see B98, for a similar discussion). This mechanism does not help to explain the changing fraction of HP-HB stars.

2.5.3 Elemental Abundances Gradients

Carter et al. (2011) found that the UVX depends more strongly on [α/Fe] than [Fe/H]. An abundance gradient in [α/Fe] could be expected if high amounts of star formation and supernovae increase the α-element enrichment of stars in the bulges of galaxies (Greggio & Renzini, 1999; Bressan et al., 1994; Catelan, 2009). However, Saglia et al. (2010) found no obvious gradient in [α/Fe] over the regions we analyze in M31. Within the bulge of M31, the negative radial metallicity gradient exhibits a much stronger correlation to the stellar populations responsible for the UVX.

Higher metallicity also implies higher Helium content ($\Delta Y/\Delta Z \sim 2-3$, Greggio &

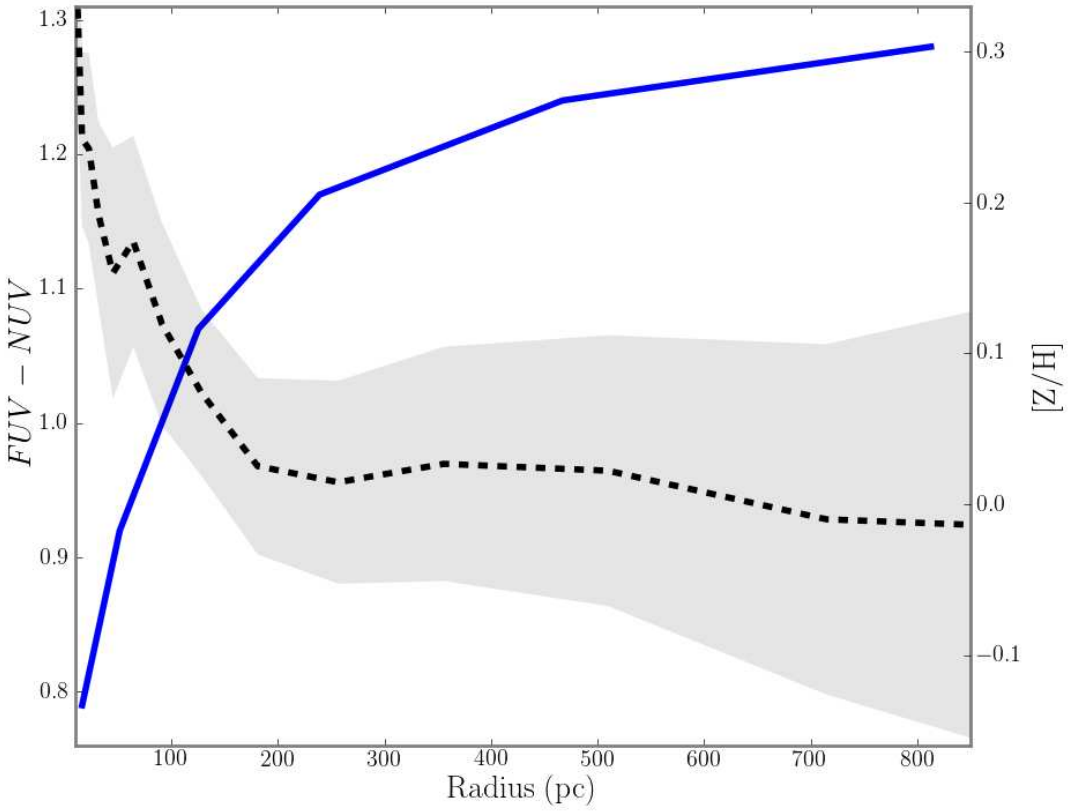

Figure 2.11 Strong anti-correlation as a function of radius between GALEX color (blue; Thilker et al., 2005) and the Lick Index-based metallicity and dispersion derived by Saglia et al. (2010) (right axis, black). There is a sharp increase in metallicity where the $FUV - NUV$ color becomes extremely blue. This anti-correlation may be evidence of the galactic metallicity gradient driving the radial variation in the numbers of UV-bright stars detected. The extreme blue color further shows that the UV-bright populations are strongly confined to the inner ~ 300 pc ($\sim 75''$) of the M31 bulge.

Renzini 1990; $2.5 - 5$, Bressan et al. 1994; at least 2.5, Pagel et al. 1992). The MSTO mass decreases strongly with increasing Helium abundance for a given age (see O'Connell, 1999, and references therein). For a fixed amount of RGB mass loss, increased Helium content will lead to hotter HB stars, that is, more EHB stars. Higher initial abundances of Helium will also cause the star to burn more of its Hydrogen envelope during the HB phase, also favoring the production of HP-HB stars (O'Connell, 1999; Horch et al., 1992). The increased Helium abundances necessary to produce EHB stars could be from contamination by the winds of older generations of AGB stars (Norris, 2004), the winds of massive stars (Decressin et al., 2007). Alternatively, these stars may have formed from the accretion of material from winds of central stars (Seth, 2010). High Helium content is a necessary ingredient to reproduce our results, and stellar winds causing the higher Helium could explain the radial gradients we detect. Detailed stellar evolution modeling that varies the possible range of Helium abundances from wind contamination is necessary to conclusively explain the radial gradient in MS stars that become HP-HB stars.

2.5.4 Radial Dust Gradients

Differential dust reddening could lead to gradients in the number of UV-bright stars detected as a function of radius. It is evident from Figure 2.2 that there is some structured dust obscuration in the bulge. The question then becomes, is there systematically less dust in the center of the bulge and if so, could dust alone account for the observed increase in faint UV sources towards the center of the galaxy?

Based on three lines of evidence, we find it unlikely that the UV population gradients are caused by dust. First, M31's bulge is a 3-dimensional object, and its dust is likely to be confined primarily to the midplane. It is therefore reasonable to assume $\sim 50\%$ of the bugle stars are in front of the dust layer. Second, we have inspected far-IR images of the bulge and see no systematic gradient in the FIR surface brightness over the central kiloparsec. We also see no obvious dust hole in the central regions. Finally, an A_B extinction map (Melchior et al., 2000; Ciardullo et al., 1988) shows no evidence of a significant radial dust gradient in the inner regions of M31. Therefore, while it is likely that dust has reduced the

total number of UV stars we have detected (such that the percentages in Figure 2.10 are likely to be lower limits), it is unlikely that radial variations in extinction can be responsible for the rapid decline in HP-HB stars with radius.

2.6 Closing Remarks

We have shown that the UV-bright population in the bulge of M31 is due largely to the progeny of hot HB stars. Our findings are consistent with the conclusion of B98, that these stars are just the tip of the iceberg of the hot HB stars responsible for the UVX. We report radial gradients in the resolved UV stellar population of M31's bulge that may be imperceptible in other data (e.g., in optical/NIR observations) because they require less than $\sim 3\%$ of the evolving stellar populations in the bulge ($\sim 2\%$ for M31's inner arcseconds and $\lesssim 5\%$ for M32 cf., B98; Brown et al. 2000). We have demonstrated the great utility of PHAT wide-area data, though bluer, deeper data are necessary for directly measuring the UVX.

The gradients in the likely HP-HB stars can only result from gradients in the properties of their progenitors across the bulge. The most likely changes in progenitor properties across the bulge are due to gradients in metallicity, possibly coupled to gradients in Helium abundance.

Chapter 3

THE RATIO OF BLUE AND RED HELIUM BURNING STARS IN ANGST GALAXIES

3.1 Context

In the last chapter, we studied the progeny of the extreme HB, low mass core He burning stars, in M31. In this chapter, we look to higher mass counterparts of the HB, luminous core He burning stars, and instead of M31, we use data from many nearby dwarf galaxies to constrain uncertain physics of HeB stars, specifically, a boundary effect on zones of convection called core overshooting.

3.2 Introduction

As we have seen, resolved stellar populations are excellent laboratories for testing our understanding of galaxy formation, integrated colors and luminosities, supernova progenitor masses, and energy input from stellar feedback. However, the usefulness of resolved stellar populations rests on the ability to accurately model the evolution of the underlying stars.

Several key phases of stellar evolution are well understood in a wide variety of environments, (for a full review see Gallart et al., 2005). However, uncertainties remain, and can be especially problematic for luminous, rapidly-evolving phases. One such uncertain evolutionary stage is the luminous core Helium burning (HeB) phase. HeB stars have $M \gtrsim 1.75 M_{\odot}$, though are usually observed at intermediate masses ($1.75 \lesssim M \lesssim 15 M_{\odot}$) where the HeB phase lasts $\sim 20\%$ of the MS lifetime.

HeB stars are those that begin He-fusion in a non-degenerate core. Such stars have already climbed the red giant branch (RGB), and are in the stellar evolution phase before becoming AGB stars (if $M \lesssim 8 M_{\odot}$) or stars fusing Carbon in their cores (if $M \gtrsim 8 M_{\odot}$). HeB stars occupy two luminous nearly-vertical sequences on a color-magnitude diagram (CMD, see Figure 3.1). Each sequence is populated by stars with a range of masses ($\sim 2 - 15 M_{\odot}$),

with the luminosity increasing nearly monotonically with mass.

Successful models of HeB stars must reproduce not only their mass-luminosity relationship, but also their unusual color distribution. HeB stars split their evolution to two sides of a CMD as they undergo a "blue loop" (see, e.g., Kippenhahn et al., 2013). They begin with large convective atmospheres near the Hayashi line[1] on a red sequence (RHeB), and rapidly evolve to hotter, bluer colors, pausing their evolution on the blue sequence (BHeB) that sometimes overlaps with the MS (in optical filters), before returning toward the Hayashi line, ending the HeB phase (see Section 3.3). Comparing the colors of the two sequences, and the ratio of the number of HeB stars (of a given age or mass) on each sequence sheds light on the subtle interior stellar physics that cause these stars to travel across the HR diagram and back again (e.g., Dohm-Palmer & Skillman, 2002).

There are two main observational motivators to accurately model HeB stars. First, given the mass range of HeB stars, HeB sequences are populated by stars that formed in the last $\sim 25 - 300$ Myr (e.g., Dohm-Palmer & Skillman, 2002). This behavior makes HeB stars an unambiguous tracer of recent star formation on these sequences. Second, redder HeB stars make significant contributions to NIR flux (Dalcanton et al., 2012; Melbourne et al., 2012) which has important consequences for integrated galaxy colors and luminosities, particularly in an era where NIR observations are increasingly important. However, the ability to use HeB sequences as probes of the star formation history rests on accurate models of the complex phenomena that occur in the interiors of these stars.

The interiors of HeB stars are complex because they are convective. Stars more massive than $\sim 1.2 M_{\odot}$ experience convective cores during their core fusion stages of evolution (e.g., Bertelli et al., 1994). In standard stellar evolution models, the transport of energy via convection is approximated by mixing length theory (Böhm-Vitense, 1958) which assumes the distance a convective cell moves until it dissolves into its surroundings is proportional to the pressure scale height inside the star. These theories usually include some parameterization of how much material overshoots the classical (Schwartzchild) convective boundary (e.g.,

[1]The Hayashi line is cool $T_{\rm eff}$ limit for stars with large convective envelopes. Since convection is very efficient in transporting energy, stars cannot have cooler $T_{\rm eff}$ at constant L, so they naturally pile up when this limit is reached.

Bressan et al., 1981), this "core overshooting" encodes the degree to which a convective cell travels beyond the theoretically expected region.

The exact strength of overshooting is not known from first principles, and thus stellar evolution models depend sensitively on how overshooting is implemented and calibrated. Following the early work by Saslaw & Schwarzschild (1965) and Bressan et al. (1981), several groups have shown the need for core overshooting and constrained its amplitude by: (1) calculating and fitting isochrones (e.g., Bressan et al., 1986; Stothers & Chin, 1981; Matraka et al., 1982; Bertelli et al., 1985, 1986; Woo & Demarque, 2001; VandenBerg et al., 2006); (2) modeling binary star systems (e.g., Claret, 2007; Ribas et al., 2000; Andersen et al., 1990); and (3) using results from asterosiemology (e.g., Straka et al., 2005; Aerts et al., 2003). These studies have suggested that the strength of core overshooting may not be constant among all stars, and instead may increase with mass (e.g., Umezu, 1995; Ribas et al., 2000; Claret, 2007; VandenBerg et al., 2006) and possibly metallicity (Cordier et al., 2002).

Most observational constraints on core overshooting in general have come from MS stars (Gallart et al., 2005, and refs. therein). However, there are other phases of stellar evolution that are even more sensitive to core overshooting that can potentially provide stronger constraints (e.g., Chiosi et al., 1992). In particular, during the blue loop, HeB stars' surface temperature and luminosity are extremely sensitive to stellar evolutionary parameters that control mixing, involving convective overshooting (e.g., Bertelli et al., 1994). HeB stars therefore provide an excellent testing ground for stellar evolution models (e.g., see discussion in Brocato et al., 2003).

Successful models of HeB stars rest on correctly modeling the blue loop. Since the blue loop effectively splits the HeB evolution phase in two, models must reproduce the observed colors and magnitudes of the two HeB sequences (as a function of age and metallicity).

Correctly modeling the color and magnitude distribution of HeB stars is not enough to constrain HeB lifetimes. The observed number of BHeB stars to RHeB stars as a function of age (hereafter the B/R ratio) is the primary means of constraining the relative lifetimes of BHeB and RHeB stars. There have been several attempts to use this ratio as a definitive test of the accuracy of massive and intermediate mass stellar models (e.g., van den Bergh,

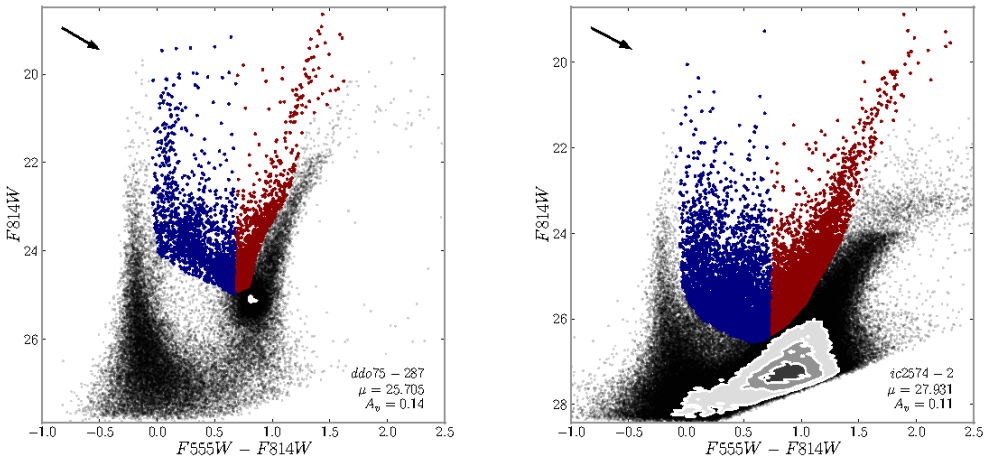

Figure 3.1 Representative CMDs in the galaxy sample. Examples of HeB regions in Sextans A and IC2574. BHeB stars are shown in blue and RHeB stars in red. The blue-ward plume of the BHeB is the main sequence. The ridge of stars red-ward of the RHeB are the RGB, which merge with the dense red clump at fainter magnitudes. Above the tip of the RGB and redder are AGB stars. Distance modulus, μ, and interstellar extinction A_v corrections are from Dalcanton et al. (2009), a reddening vector is drawn for 0.5 mag of extinction.

1968; Langer & Maeder, 1995; Maeder & Meynet, 2001). Until recently, the observational history of B/R ratios was rife with inhomogeneity and confusion, which has led to uncertain calibrations and interpretations of intermediate mass ($12 - 20 M_{\odot}$) and massive star models (e.g., Maeder & Conti, 1994; Langer & Maeder, 1995, and references therein).

Nearly all the historical issues in determining the B/R ratio can be addressed by using large statistical samples of HeB stars. However, such samples are difficult to create in stellar clusters, the traditional laboratories for stellar evolution studies. Because the HeB is a short lived phase, very few stars will be passing through the RHeB or BHeB in any given stellar cluster. Therefore, measurements in clusters in the MW and MCs have had too few stars to reliably measure the relative numbers of B/R stars or trace the entire sequences of colors and magnitudes spanned by HeB stars of different masses and metallicities.

As an alternative approach, one can analyze CMDs of entire galaxies, rather than individual stellar clusters. Not only do galaxies have many more stars overall, but their extended star formation histories frequently allow the entire HeB sequence to be populated with stars

of many different ages (and thus, masses). The strongest constraints in the literature have come from such an approach (e.g., McQuinn et al., 2011), following the seminal work by Dohm-Palmer & Skillman (2002).

The ACS Nearby Galaxy Survey Treasury (ANGST; Dalcanton et al., 2009) and the ANGRRR archive[2], provide an excellent stellar database for these kinds of studies. Through its volume limited nature (D $\lesssim$ 4 Mpc), ANGST provides an unbiased window into the demographics of a statistically significant diverse sample of nearby galaxies. The ANGST sample has produced photometry for $\sim$ 14 million resolved stars in $\sim$ 70 galaxies spanning more than a factor of 10^4 in luminosity, $\sim$ 2 dex in metallicity across a wide range in morphological types and environmental settings.

Using data from ANGST, McQuinn et al. (2011) (hereafter M11) compared the HeB stars in 19 nearby star bursting galaxies to predictions from the Padova stellar evolution models (Girardi et al., 2008a; Marigo et al., 2008). They found generally good agreement, however, discrepancies exist in the colors of the HeB sequences as well as inconsistencies between the modeled and observed B/R ratio at the youngest ages.

In this chapter, we find that the strength of core overshooting in intermediate mass stars is mass-dependent, using 44 fields of 33 ANGST galaxies ranging from 1.3 to 4.6 Mpc and Z=0.0005 to 0.03. This work significantly expands the galaxy sample of M11 and forms the framework for specific revisions in critical core overshooting prescriptions. We introduce an initial prescription for mass-dependent core overshooting and discuss how it better matches the observational data and derived HeB lifetimes..

The chapter is outlined as follows. We begin in Section 3.3 with an overview of the stellar evolution of HeB, with a specific focus on its relationship to convection. In Section 3.4, we briefly describe reduction of the archival HST data, our galaxy sample, and the method for identifying the HeB stars and the BHeB and RHeB sequences. In Section 3.5, we present the HeB sequences, and the theoretical and observationally derived B/R ratio using the Padova Trieste Stellar Evolution Code as it is presented in Bressan et al. (2012). We discuss the need for and a basic implementation of mass-dependent core overshooting

[2]http://archive.stsci.edu/prepds/angrrr/

and the resulting model predictions in Section 3.6. We conclude in Section 3.7.

3.3 Stellar Evolution of HeB Stars

Before investigating the ANGST data for constraints on the uncertain physics of HeB stars, we review the evolution of HeB stars and their most uncertain feature, convection.

3.3.1 Stellar Evolution During a Blue Loop

Throughout the HeB phase, some stars will contract, heat up, and reach temperatures closer to MS stars of similar luminosity. This excursion to high $T_{\rm eff}$ and subsequent return to the Hayashi line is called the "blue loop," as seen in Figure 3.2. The stellar interior of a $5M_{\odot}$ star on the blue loop is shown in Figure 3.3. The bottom of Figure 3.3 is a Kippenhahn diagram limited to the HeB phase[3]. The top panel is log $T_{\rm eff}$, the surface temperature, and the three panels in the middle are all quantities measured in the center of the star (from top to bottom, the mean molecular weight, μ_c, the central density, ρ_c, and the central pressure, log P_c).

In Figure 3.3 the regions in which fusion occurs are marked by red (He) and blue (H), and the convective region is shaded grey. The useful quantities included in this Kippenhahn diagram are the mass fraction of the core (solid black), the fraction of stellar luminosity from fusing Hydrogen (L_X, dotted blue) and Helium (L_Y, dotted red), and the central mass fractions of Helium (Y_c, solid red), Oxygen (^{16}O, purple), and Carbon (^{12}C, green). The blue loop, more clear perhaps in Figure 3.2, can be seen in the change of temperature in the top panel of Figure 3.3. For clarity, the end of the RHeB and the maximum $T_{\rm eff}$ of the BHeB are drawn as vertical grey lines on each of the panels.

As a basic overview, for this model, the star is on the RHeB locus from $\sim 88 - 91$ Myr, traverses the CMD until reaching the BHeB phase at ~ 94.5 Myr, after which it quickly

[3]A note on Kippenhahn diagrams: A Kippenhahn diagram is a means to visualize where in the star certain quantities are acting throughout its evolution. Since the stellar radius changes dramatically throughout a star's evolution (and many interesting processes are confined to a very small, but dense region of the star), mass fraction is usually taken as the dependent variable. With the diagram's simple scaling of mass from 0 to 1, many other scaled parameters are often overlaid. For example, in Figure 3.3, everything besides the fusion and convective regions are relative parameters.

returns toward the Hayashi line. Below we describe the primary interior processes that change the star's appearance during this phase.

The HeB phase begins with fusing He on the RHeB. As a RHeB star fuses Helium into Carbon, the mean molecular weight, μ_c, of the core increases, reducing the core pressure, causing the core to expand. The steady increase in the mean molecular weight of the core can be seen in the top panel of Figure 3.3. This increase initially causes the central pressure (third panel from the top), P_c, to decrease and the core to expand (since $P_c \propto \rho T/\mu$). This core expansion is similar to what happens during the main sequence, as Hydrogen is fused into Helium, although the resulting structure and atmospheric effects are quite different. For core He-burning stars, core expansion has a complicated effect on the global stellar properties, due to the Hydrogen fusion shell nestled between the stellar envelope and the He-burning core (shown as a blue band in Figure 3.3). In this scenario, any change in core size is mirrored by the stellar atmosphere; as the core expands, the envelope contracts, and vice versa[4]. Therefore, when the core expands, the outer layers contract, increasing the effective temperature (top panel of Figure 3.3) which manifests as a star moving to the left in an HR diagram.

As fusion continues inside the RHeB star, the mean molecular weight of the He-burning core increases, causing the core to expand, and (by the mirror principle) the outer layers to contract. This contraction causes the star's atmosphere to cease convection and instead transport the bulk of the outflowing energy radiatively. The switch to radiation energy transport causes the effective temperature to become much hotter, until a maximum temperature is reached, moving the star onto the BHeB sequence.

What finally ends the BHeB phase and causes the star to return toward the Hayashi line cannot be simply stated. It is clear that the core density increases again, and in response, the envelope expands and becomes convective. What is less clear, however, is the critical values that determine exactly when the star begins to decrease its $T_{\rm eff}$. Most signs point toward

[4]This "mirror principle" of shell burning can be explained by following how the fusion shell must react to a changing core to remain in thermal equilibrium. The shell must remain at nearly constant temperature, due to the temperature sensitivity of nuclear burning. If the shell expands, for example, it would imply cooling. During core He-burning, when the core expands, the density of the fusion shell must increase at constant temperature, meaning the pressure above the shell must increase, so the layers above the shell must contract.

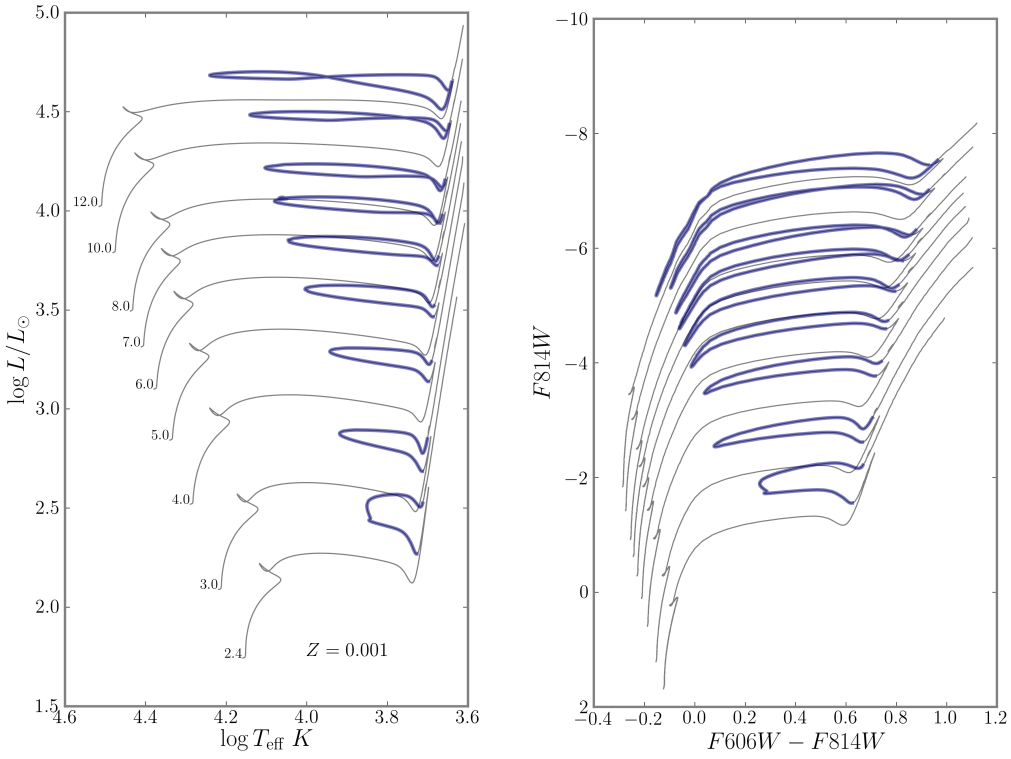

Figure 3.2 Sample Bressan et al. (2012) stellar evolution tracks for Z=0.001 and Y=0.25 from the beginning of the MS to Carbon burning or the first thermal pulse of the AGB (depending on mass). Blue loops are highlighted in blue and initial masses (in units of $M_\odot$) are marked at the beginning of the MS. Left: HR diagram, Right: CMD in HST filters.

the beginning of the exhaustion of He in the core, which can be seen as the $^{12}\mathrm{C}(\alpha,\gamma)^{16}\mathrm{O}$ reactions begins to take place.

The size of the stellar core determines the lifetime of the HeB stage, as well as the MS lifetime. Different strengths of convective overshooting change the size of the core, and thus effect the delicate balance that determines the length of time spent as a BHeB star, and the maximum $T_{\rm eff}$ reached at that stage. We now turn to the most uncertain physical parameter in HeB models, the strength of convection.

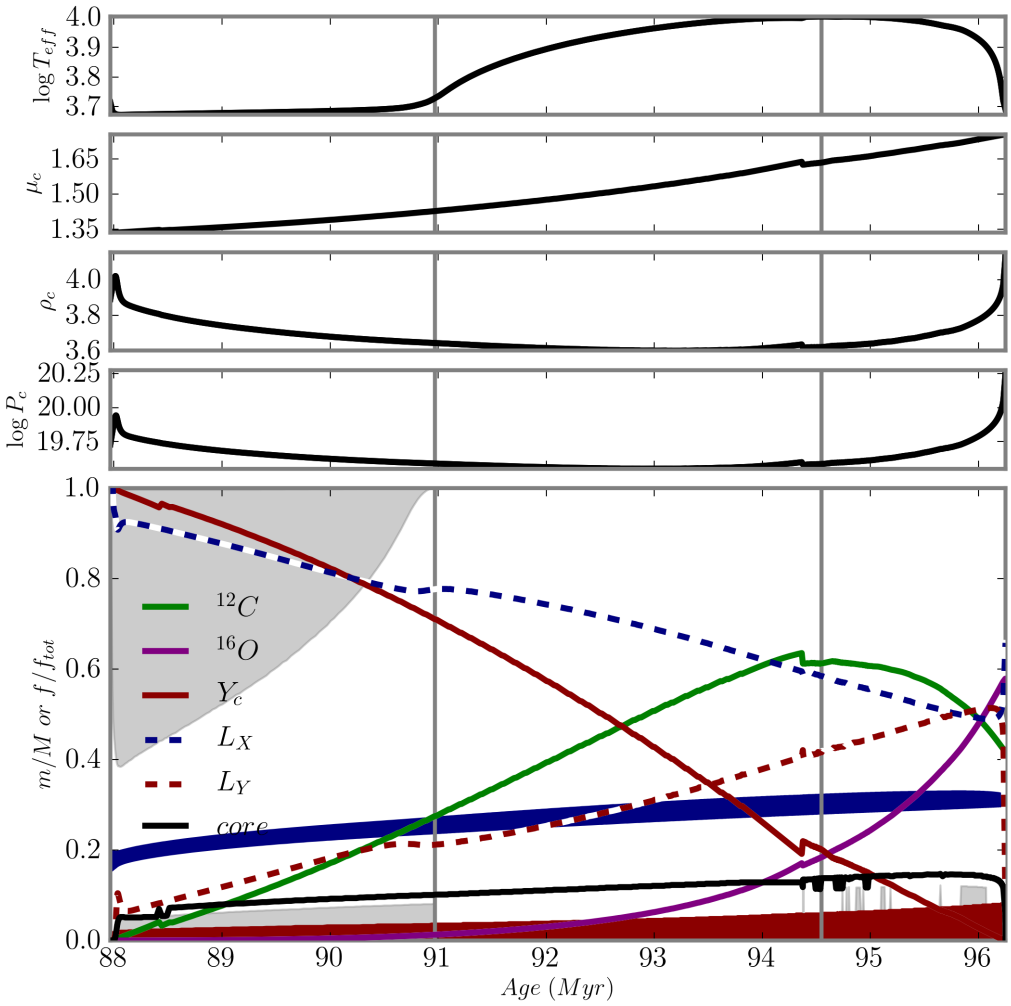

Figure 3.3 Stellar interior parameters of a $5.0 M_{\odot}$ star during the blue loop. Top panels show important players in the blue loop (top to bottom): log effective temperature, and central parameters, mean molecular weight μ_c, density $\log \rho_c$, and pressure $\log P_c$ (all units in cgs). Bottom panel is a Kippenhahn diagram showing the mass fractions of convective regions (grey), He-burning core (red fill), H-burning shell (blue fill), and the edge of the convective core (solid black; region of convective overshooting is considered to be radiative). Relative central abundances are overlaid, ^{12}C, green; ^{16}O, purple; and He, red, as well as the relative amount of total luminosity due to Hydrogen fusion (blue dotted) and He fusion (red dotted). Grey vertical lines mark the RHeB, identifiable by the sharp change in $T_{\rm eff}$, and the BHeB, set at the maximum $T_{\rm eff}$ of the loop.

3.3.2 Complications from Convection

Convection occurs in regions of a star where the radiative temperature gradient, $\nabla_{\rm rad}$, is larger than the adiabatic temperature gradient, $\nabla_{\rm ad}$ (e.g., Kippenhahn et al., 2013). In other words, for a star to transport energy by the motion of convective cells, it must be very difficult to transport energy via radiation. There are two regimes when convection may occur, both of which arise when the radiative temperature gradient is very steep.

The radiative temperature gradient is proportional to $\kappa\rho L/r^2$, where κ is the opacity, ρ is the density, r is the radius, and L is the luminosity. Therefore, when κ or L/r^2 is large, the adiabatic temperature gradient is shallower than the radiative temperature gradient, and convection occurs.

The first convective regime occurs in cool stellar atmospheres, where the H^- ion leads to large opacities. The other regime occurs in the cores of stars where an enormous amount of energy is generated in a small area, usually when the fusion efficiency, ϵ, depends very strongly on temperature, leading to a large L/r^2. Convective cores are found in MS stars with $M \gtrsim 1.2 M_\odot$, where the CNO cycle leads to $\epsilon \propto T^{12}$, and in the cores of stars that fuse heavier elements. Convection also occurs in BHeB stars, where fusion in the Helium core via the triple-α process produces strongly temperature dependent efficiencies ($\epsilon \propto T^{30}$). This condition is also met later in BHeB evolution where the $^{12}C(\alpha,\gamma)^{16}O$ reaction with $\epsilon \propto T^{42}$ takes over.

Where and when convection occurs in stars is well understood. However, how well the convection mixes the stellar material is not. The Schwarzschild criterion, defined when the condition $\nabla_{\rm ad} = \nabla_{\rm rad}$ is met, can be imagined as a convective cell accelerating until hitting a wall when the buoyancy force is balanced by the pressure over the cell's area. However, a cell can still have momentum at that boundary, and therefore will not instantly come to a stop. More realistic treatments of convection (in the absence of fully consistent 3d hydrodynamical models) follow the momentum of a convective cell that overshoots this historical boundary.

One of these treatments comes from the models we use throughout this disseration. The **Pa**dova and T**r**ieste **S**tellar **E**volution **C**ode (PARSEC) is a thoroughly revised version of the

popular Padova stellar evolution code (Bressan et al., 2012, and http://stev.oapd.inaf.it/cmd) Briefly, PARSEC in its version 1.1 offers new stellar tracks that span $0.0005 \leq Z \leq 0.07$, $0.1M_{\odot} \leq M \leq 12M_{\odot}$, from the Pre-MS phase to either the thermally-pulsating AGB or the core Carbon ignition phase.

PARSEC calculates energy transport by convection by parameterizing the mean free path, l, of a convective cell across the boundary of the convective region in units of the pressure scale height, H_p (Bressan et al., 1981). We hereafter refer to $\Lambda_c = lH_p$ as the core overshooting parameter (N.B. the definitions of core overshooting differ among stellar evolution modeling groups, e.g., Meynet et al., 1994, and refs. within). PARSEC adopts the same parameter as has been used by the Padova Stellar evolution group. This specific value of Λ_c has been constrained for low mass stars using the MSTO morphologies of open clusters in the Milky Way, the populous intermediate-age clusters in the Magellanic Clouds, and using recent results from asteroseismology ($M \lesssim 2.5M_{\odot}$) (Girardi et al., 2009; de Meulenaer et al., 2010; Kamath et al., 2010). For these standard models, PARSEC adopts $\Lambda_c = 0.5$ for $M > 1.5M_{\odot}$ i.e., the mixing length of convective cells reduces to $0.5H_p$ across the theoretically unstable region (Bressan et al., 2012). This value is consistent with previously mentioned studies which have broadly constrained Λ_c to the range of $0 < \Lambda_c \lesssim 2$, with typical values $\Lambda_c \sim 0.5$. However, there is evidence that for higher mass stars, Λ_c should be greater (e.g., $\Lambda_c \sim 0.6$, Godart et al., 2013). Throughout this chapter, we refer to the PARSEC models published with $\Lambda_c = 0.5$ as B12.

3.3.3 Core Overshoot and the Blue Loop: A New Model Grid

The first step in constraining values of Λ_c is building an appropriate set of models. Several observational properties of blue loops depend on the size of the convective core, where the amount of core overshooting is most uncertain. The strongest constraints on the strength of core overshooting currently come from the morphology of the main sequence turn off (MSTO) of low mass stars ($M \lesssim 1.8$, e.g., VandenBerg & Stetson, 2004; Rosvick & Vandenberg, 1998; Gim et al., 1998). Although these constraints are based on very different masses and evolutionary phases than the HeB stars of interest, these MS studies are useful guides

for what range of Λ_c might be plausible. They also provide a benchmark for comparing new Λ_c models in that changes to Λ_c should not "break" existing results from MSTO studies. One important constraint is the lifetime of the MS.

For the range of $0.3 < \Lambda_c < 0.7$, the MS lifetime does not change more than 10% for all masses between $2-12M_\odot$ and metallicities $0.0005 \leq Z \leq 0.03$ (see Figure 3.4). Thus, a wide range of core overshooting parameters are essentially indistinguishable in terms of the age of the MSTO. This insensitivity suggests that there may be substantial leeway in adjusting Λ_c without violating the observed properties of the MS, and we therefore consider a large rang in Λ_c when comparing to data. However, as has been shown in e.g., Bertelli et al. (1994), an increase in core overshooting does lead to a hotter, brighter MSTO at constant age, meaning the ages of stars derived from isochronal fitting could be off by $\sim 10\%$ (see Figure 3.5).

To build a set of stellar models appropriate for comparing to galaxy observations, we proceed as follows. First, a large set of evolutionary models are calculated with PARSEC with a range of mass, metallicity, and Λ_c. The surface quantities of each stellar model are also calculated ($\log L, \log T_{\rm eff}, \log g$) and then translated into colors and magnitudes (using the methods and tables of Girardi et al., 2008a). Calculated stellar evolution tracks of all masses are then interpolated to create isochrones for each metallicity.

As an initial attempt to narrow the best range of Λ_c, we used PARSEC to calculate three large grids of stellar evolution models (924 total tracks) with $\Lambda_c = 0.3, 0.5$, and 0.7. Each of those grids were calculated with metallicities, $Z = 0.0005$, 0.001, 0.002, 0.004, 0.008, 0.010, 0.011, 0.014, 0.017, 0.02, and 0.03. The corresponding Y values were derived from the Helium enrichment relationship in Bressan et al. (2012): $Y_0 + dY/dZ * Z$, where Y_0, the primordial value of He-content is 0.2485, and $dY/dZ = 1.80$. Within these chemical compositions and core overshooting parameters, we calculated evolutionary tracks of stars with mass $M \geq 2.5M_\odot$: M =2.5, 2.8, 3.0, 3.4, 4.0, 4.2, 4.4, 4.6, 4.8, 5.0, 5.2, 5.4, 5.6, 5.8, 6.0, 6.2, 6.4, 6.6, 6.8, 7.0, 7.4, 8.0, 9.0, 10.0, 11.0, 12.0, 15.0, and $20.0M_\odot$. These tracks were then interpolated in age to create isochrones[5] with log Age $7.0-9.0$ and steps of $d\log$

[5]Throughout this dissertation, "tracks" refer to stellar evolution models as a function of age, and "isochrones" refer to an interpolation of several stellar evolution models at a constant age.

Age = 0.15.

To identify when a model enters the BHeB and RHeB, we tag the evolutionary stages in PARSEC and follow them through to the calculation of isochrones. The BHeB is defined as the maximum $T_{\rm eff}$ during the HeB, and the RHeB is defined by the minimum luminosity between the tip of the RGB and the BHeB.

Increasing the degree of core overshooting leads to two major effects during HeB phases. It decreases the temperature extent of the loops and decreases the relative amount of time a star spends near the BHeB sequence (c.f., Becker, 1981; Bertelli et al., 1986; Bressan et al., 1986). These effects can be seen in Figure 3.5, which shows isochrones calculated with different amounts of core overshooting. The lower the value of Λ_c, the larger the temperature extension of the loop. While the lifetimes of the HeB are reduced with increasing core overshooting, Figure 3.6 shows that the *relative* amount of time spent near the BHeB decreases with increasing Λ_c. These changes also depend on stellar mass, since the core mass increases with stellar mass, such that the evolution of higher mass stars is more affected by changes in Λ_c.

3.4 Data

We now have models that span a large range in possible strengths of core overshooting for intermediate mass stars. To constrain this range, we must look to observations of galaxies with well populated HeB sequences. In the following section we discuss the galaxy data with respect the the HeB stars.

3.4.1 Data Reduction

All data were reduced as outlined in the ANGST survey paper and we refer the reader to Dalcanton et al. (2009) for complete details. As a brief summary, STScI ACS pipeline data were photometered using DOLPHOT2.0 (Dolphin, 2002) including the ACS module. Cosmic rays were rejected after combining all images into a single drizzled image using the multidrizzle task within PyRAF (Koekemoer et al., 2003). We use the conservative data product (`*gst`), which only includes objects with DOLPHOT parameters `SNR < 4`, ((`sharp1` + `sharp2`)$^2 \leq 0.075$, and crowding ((`crowd1` + `crowd2`) ≤ 0.1) in both filters. As

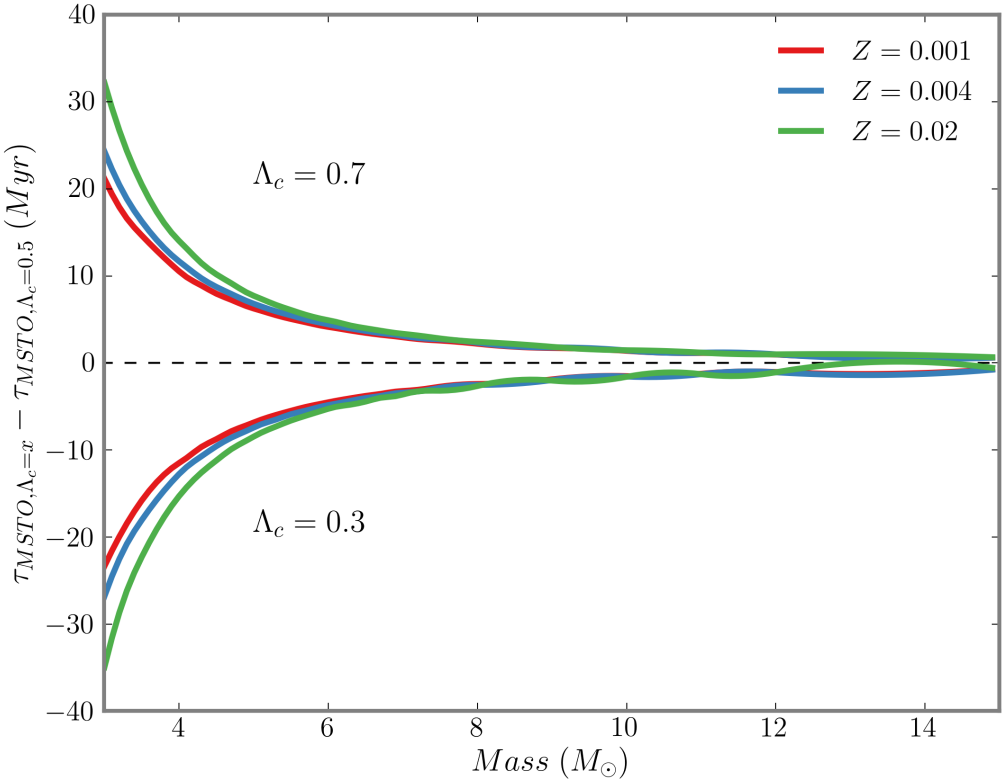

Figure 3.4 MSTO age differences (in Myr) with high and low values of core overshooting strength compared to the canonical value ($\Lambda_c = 0.5$ Bressan et al., 2012). Shown are three example metallicities $Z = 0.001$ (red), 0.004 (blue), and 0.02 (green). Increased core overshooting strength compared to Bressan et al. (2012) leads to a longer MS phase, and more so with increasing metallicity, while the opposite is true for relatively smaller values of Λ_c. The maximum fractional difference in MSTO age from either core overshoot value compared to $\Lambda_c = 0.5$ is 0.1 suggesting a wide range in core overshooting parameter exists without largely effecting stellar population ages.

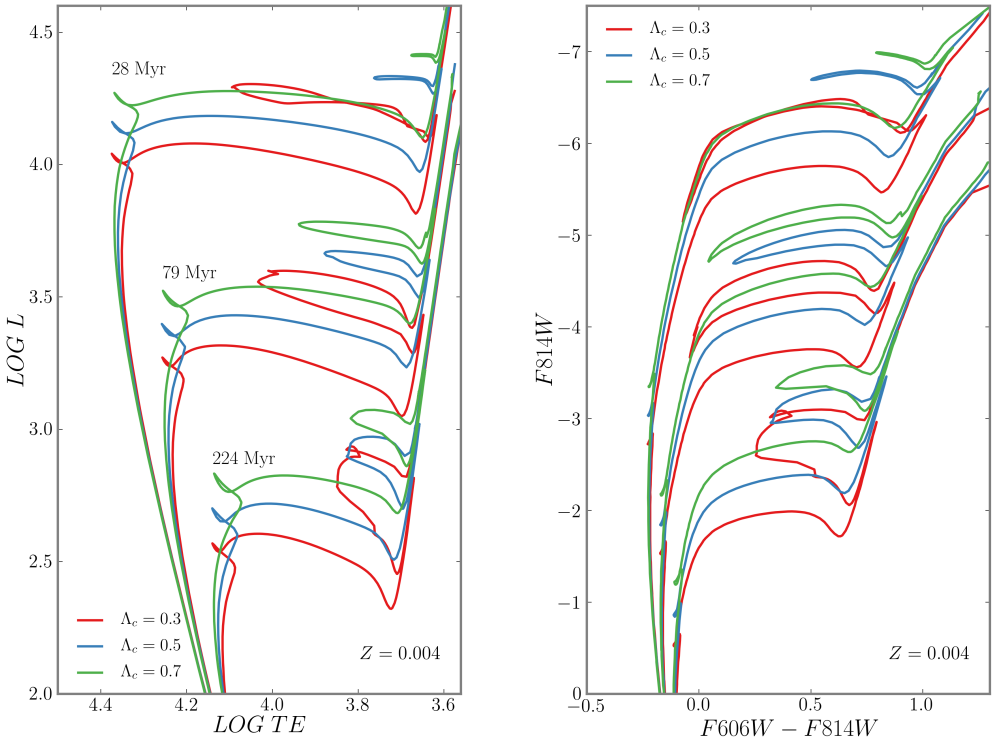

Figure 3.5 The effects of core overshooting on the HR diagram (left) and an *HST* cmd (right). Shown are isochrones with $Z = 0.004$ and different core overshooting values, $\Lambda_c =$ 0.3 (red), 0.5 (blue), and 0.7 (green). As Λ_c increases, the temperature extension of the blue loop decreases and the luminosity of the isochrone gets brighter.

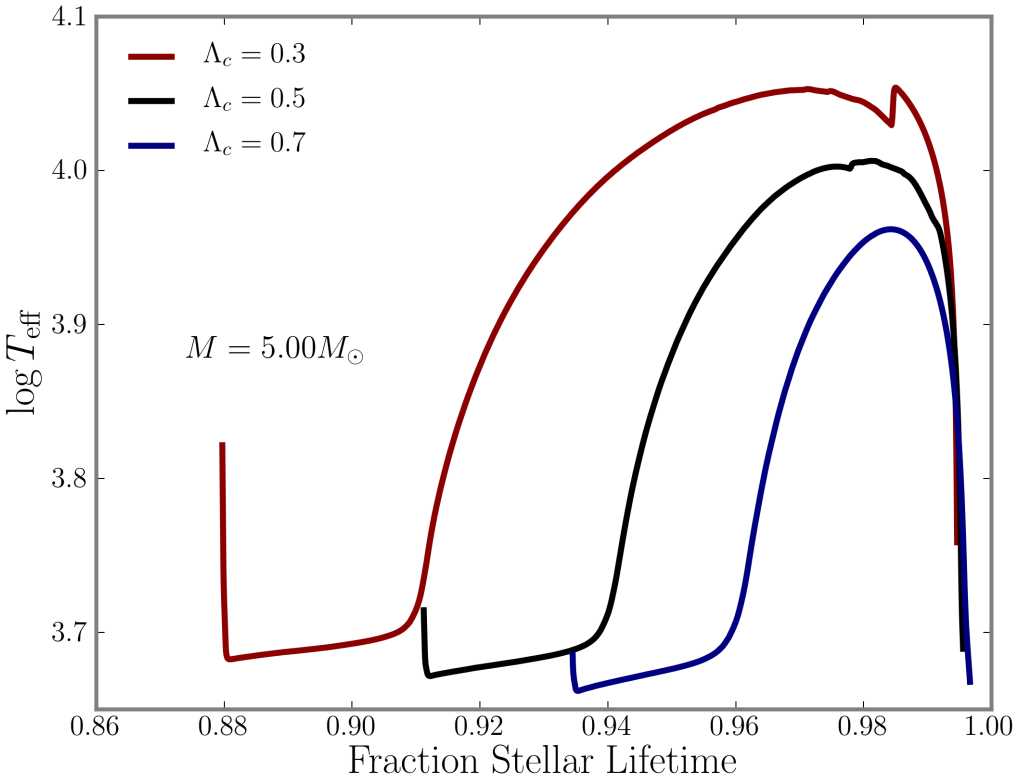

Figure 3.6 Increasing core overshooting decreases the HeB lifetime and temperature extent of the loop. Shown here is an example of a $5M_\odot$ star with three values of core overshooting plotted against the fraction of the stellar lifetime (defined between the onset of He-burning until the first thermal pulse on the AGB). The adopted value in B12 and the preceding Padova Stellar Evolution models ($\Lambda_c = 0.5$) is shown in black, lower than canonical value Λ_c=0.3 is shown in red, and higher than canonical value Λ_c=0.7 is shown in blue

necessary, ANGST and ANGRRR followed the WFPC2 pipeline of Holtzman et al. (2006), which processes STScI baseline output through HSTphot, a WFPC2 optimized predecessor of DOLPHOT but updated to July 2008 CTE corrections (derived by A. Dolphin).

3.4.2 Galaxy Sample

We selected any galaxy from ANGST that shows obvious BHeB and RHeB sequences. For each galaxy we analyzed photometry for $F814W$ and the bluest available filter, allowing us to maximize the color baseline, enhancing the separation of CMD features.

The resulting sample of 25 galaxies is listed in Table 3.1 in order of increasing luminosity. The metallicity of the young stars is estimated using spectroscopic gas-phase oxygen abundances taken from Berg et al. (2012), when available. In the absence of spectroscopic constraints, we used the SFH-weighted average metallicities obtained from the best-fit star formation histories derived by Weisz et al. (2011). Metallicities determined by MATCH are highly weighted by the need to match the shape of the RGB (Dolphin, 2000), and therefore track a wide range of stellar ages, all of which are typically older than the HeB stars used in this study, thus, our adopted MATCH metallicities are lower limits to the metallicity of the underlying stellar population that gave rise to the HeB stars in our sample.

From either the spectroscopic oxygen abundance (O/H) or the MATCH estimated iron abundance [Fe/H], we estimated the metallicities of each galaxy,

$$z_{\rm galaxy} = z_{\odot} * 10^{[\rm Fe/H]_{\rm galaxy}} \tag{3.1}$$

where,

$$[\rm Fe/H]_{\rm galaxy} = \log(\rm O/H) - \log(\rm O/H)_{\odot} \tag{3.2}$$

using the value of Solar oxygen abundance, $\log(\rm O/H)_{\odot} = 8.76$ from Caffau et al. (2008) and the value of Solar metallicity, $z_{\odot} = 0.015$. We list the resulting metallicity in Table 2.

3.4.3 Isolating the HeB Stars, and the RHeB and BHeB sequences

In optical CMDs, at bright magnitudes, the BHeB sequence is nearly vertical and parallel to the MS. The photometric quality is such that the sequences are obviously separate. The

Properties of Sample Galaxies

Galaxy	Alt. Name	M_B	D (Mpc)	A_V	$12 + \log(O/H)$	source	Z	Z_{MATCH}	$Z_{\rm isochrone}$
Antlia	...	-9.38	1.3	0.24	7.39	1	0.0008	0.0010	0.001
KKH 98	...	-10.29	2.5	0.39	...	...	...	0.0021	0.002
KDG 73	...	-10.75	3.7	0.06	...	...	...	0.0006	0.0006
A0952+69	Arp's Loop	-11.38	3.9	0.26	...	...	...	0.0112	0.011
UGCA 292	...	-11.36	3.1	0.05	7.30±0.05	2	0.0007	0.0002	0.0007
KDG 52	M81 Dwarf A	-11.37	3.5	0.06	...	...	...	0.0007	0.0007
GR 8	UGC 8091	-12.00	2.1	0.08	7.65±0.06	3	0.0015	0.0011	0.002
UGC 8833	...	-12.31	3.1	0.04	...	...	...	0.0007	0.0007
DDO 6	UGCA 15	-12.40	3.3	0.05	...	...	...	0.0006	0.0006
UGC 4483	...	-12.58	3.2	0.11	7.56±0.03	4	0.0012	...	0.001
DDO 181	UGC 8651	-12.94	3.0	0.02	7.85±0.04	4	0.0023	0.0007	0.002
UGC 8508	...	-12.95	2.6	0.05	7.76±0.07	5	0.0019	0.0012	0.002
NGC 3741	...	-13.01	3.0	0.07	7.68±0.03	5	0.0016	0.0006	0.002
DDO 183	UGC 8760	-13.08	3.2	0.05	...	...	...	0.0010	0.001
DDO 53	UGC 4459	-13.23	3.5	0.12	7.82±0.09	6	0.0022	0.0027	0.002
Ho IX	UGC 5336	-13.31	3.7	0.24	8.65±0.25	6	0.0147	0.0060	0.015
Sextans A	DDO 75	-13.71	1.3	0.14	7.54±0.06	7	0.0011	...	0.001
NGC 4163	...	-13.76	3.0	0.06	7.56±0.14	5	0.0012	0.0030	0.001
Sextans B	UGC 5373	-13.88	1.4	0.10	7.53±0.05	2	0.0011	...	0.001
DDO 190	UGC 9240	-14.14	2.8	0.04	7.95±0.03	4	0.0029	0.0022	0.003
Ho I	UGC 5139	-14.26	3.8	0.15	7.92±0.05	5	0.0027	0.0027	0.003
NGC 3109	...	-15.18	1.3	0.20	7.77±0.07	8	0.0019	...	0.002
IC 5152	...	-15.55	2.1	0.08	7.92±0.07	9	0.0022	...	0.002
NGC 2366	...	-15.85	3.2	0.11	7.91±0.05	10	0.0027	0.0010	0.003
Ho II	UGC 4305	-16.57	3.4	0.10	7.92±0.10	11	0.0027	0.0008	0.003
NGC 4214	...	-17.07	2.9	0.07	8.22±0.05	12	0.0055	...	0.006
IC 2574	UGC 5666	-17.17	4.0	0.11	7.93±0.05	6	0.0028	0.0g	0.003
NGC 3077	...	-17.44	3.8	0.22	8.64±0.20	8	0.0144	...	0.014
NGC300	...	-17.66	2.1	0.04	8.73±0.04	8	0.0177	...	0.018
NGC 55	...	-17.77	2.1	0.04	8.05±0.10	9	0.0037	...	0.004
NGC 2403	...	-18.77	3.3	0.13	8.39±0.10	8	0.0081	...	0.008
NGC 253	...	-20.04	3.6	0.06	8.99±0.31	8	0.0323	...	0.030
M81	NGC 3031	-20.09	3.6	0.27	9.00±0.13	8	0.0330	...	0.030

Table 3.1 Properties of the 33 sample galaxies. Sources: (1) Piersimoni et al. (1999); (2) van Zee (2000); (3) van Zee & Haynes (2006); (4) van Zee et al. (2006); (5) Berg et al. (2012); (6) Croxall et al. (2009); (7) Kniazev et al. (2005); (8) Marble et al. (2010, and refs. therein); (9) Tüllmann et al. (2003); (10) Saviane et al. (2008); (11) Lee et al. (2003); and (12) Kobulnicky & Skillman (1996)

BHeB sequence becomes redder at fainter magnitudes until it merges with the red clump (RC, see Figure 3.1). MS stars that scatter redwards due to reddening or photometric errors can contaminate the BHeB sequence, biasing the B/R ratio toward higher values. Similarly, photometric errors could scatter BHeB stars bluer than their nominal sequence, merging them with the MS. This contamination would bias the B/R ratio toward smaller values.

The RHeB can suffer similar contamination issues as the BHeB, due to RGB stars at fainter magnitudes and AGB stars at brighter magnitudes. The RHeB sequence emerges from the RC nearly parallel to the RGB, and extends brighter than AGB stars (see Figure 3.1). Near the RC, RHeB stars can merge with RGB stars, while above the RGB tip, RHeB stars can merge with AGB stars in our filter sets.

Following M11 and Dohm-Palmer et al. (1997) before them, we identified HeB sequences by eye based on their position on the CMD. The color and magnitude limits of the red and blue sequences were then refined numerically to reduce contamination from other phases as follows.

To ensure minimal levels of contamination by MS stars in the BHeB region and of incompleteness due to missing BHeB stars to the MS region, we modified the simultaneous double gaussian fitting method introduced by Dohm-Palmer & Skillman (2002) to a three step fitting process. HeB stars are first defined by a polygon on the CMD that encompasses the full region of HeB stars. We divide the region into RHeB and BHeB stars by the median color of the HeB stars in the region. To determine the locations of the HeB sequences, we then divide the RHeB and the BHeB regions into magnitude bins of width 0.2 in $F814W$ and combine bins until there are at least 10 stars per bin. Finally, we take the median color of the stars in each and interpolate a quadratic function to the BHeB or a linear spline to the RHeB. Sample results of this identification scheme are shown in Figures 3.7-3.12.

To assess contamination, we first fit an unweighted gaussian to the MS and a weighted gaussian to the BHeB. The BHeB gaussian fit is weighted by the deviation in color from the median in each magnitude bin, (using 1 mag width bins). Next, we use these best fit parameters as an initial guess to fit a double gaussian to the MS/BHeB. Finally we repeat the double gaussian fit, weighting by the double gaussian model. We are then able to estimate the fraction of contaminants from MS into the BHeB and the BHeB into the MS. The

average contamination of the MS into BHeB region is 3%, and the average contamination of the BHeB into the MS region is 7%.

We apply the same double gaussian fitting from above to these phases to separate the RHeB stars from the RGB and AGB. The average contamination of RGB and AGB stars into the RHeB is 3%, and the average contamination of the RHeB into the regions of the RGB and AGB is 5%.

Stars found on the CMD between the main locii of the BHeB and RHeB are surely HeB stars. However, their identification as either a "blue" or "red" HeB star is not well defined. For simplicity, we divide the blue and red HeB stars by the median color value in each magnitude bin of the HeB region.

Many variable stars fall in the region between the HeB sequences, due to their passage through the instability strip. These stars will not necessarily be measured with their true time-averaged color and magnitude, making them hard to assign to a specific evolutionary phase based solely on cmd position. However, for common variables (such as Cepheids, and at fainter magnitudes, possibly RR Lyrae stars), the star's magnitude changes more than its colors. Their classification as RHeB or BHeB will therefore be correct, but they will not necessarily be assigned to the proper magnitude. The overall effect is small (see Dohm-Palmer & Skillman, 2002).

3.4.4 HeB Sequences of the Galaxy Sample

Figures 3.7-3.12 show CMDs and observationally determined HeB sequences for a subset of the galaxy sample, grouped together by metallicity. Figures 3.13 and 3.14 show all the measured HeB tracks. The RHeB sequence slopes are in close agreement at all metallicities but become redder with increasing metallicity. This behavior is expected for stars on the Hayashi line, for which higher metallicity gives rise to higher opacities. The BHeB sequences, however have a larger spread in color than do the RHeB sequences, though those too follow the red-ward trend with increasing metallicity.

UGC5336 (Figure 3.12) is a very interesting case, where the HeB sequence is not populated at all magnitudes, suggesting a short burst of star formation. This galaxy may provide

strong constraints on overshooting because one can simultaneously constrain the MSTO and the HeB.

3.5 Analysis

From a theoretical perspective, we have shown there is a wide range in possible CMD space available for intermediate mass HeB sequences. We have also introduced observationally determined HeB sequences in many nearby galaxies. We now compare the observations both to previous observational analyses as well as to the B12 model predictions.

Recently, M11 studied 19 nearby star-bursting dwarf galaxies with thousands of resolved HeB stars. They found significant differences between models for HeB stars and the observed CMDs. In particular, they found color offsets in all HeB sequences, including fainter BHeB stars that were observed to be bluer, and brighter RHeB stars that were redder than isochrone predictions (using the Padova stellar evolution library, which sets $\Lambda_c = 0.5$; Girardi et al., 2000; Marigo et al., 2008). Their findings could not be explained by reddening or extinction. M11 also measured the B/R ratio as a function of age in their galaxy sample. They found good agreement in general, with the exception of a high B/R ratio for high mass, younger stars with ages $\lesssim 50$ Myr.

We now add to the M11 analysis by performing similar tests using our larger galaxy sample. For this analysis we model the galaxies in the sample with PARSEC calculated with three values of the core overshooting parameter.

Figures 3.15 and 3.16 show theoretical HeB sequences color-coded by metallicity and separated in panels by Λ_c (increasing to the bottom). The sequences in the middle panel are roughly comparable to those used in M11 (B12 with $\Lambda_c = 0.5$). These HeB sequences are not stellar evolutionary phases in the classical sense (e.g., the MS). Instead, they mark the CMD locations of the BHeB or RHeB for masses $2.5 - 12 M_{\odot}$. They are also not an evolutionary sequence and are instead the superposition of stars with a range of masses typically formed in the last 25-900 Myr (though in our observations <250 Myr). We define these sequences by interpolating the HeB extrema on several isochrones ranging in age from 10 Myr -1 Gyr.

There are four main effects of core overshooting that can be seen by comparing the three

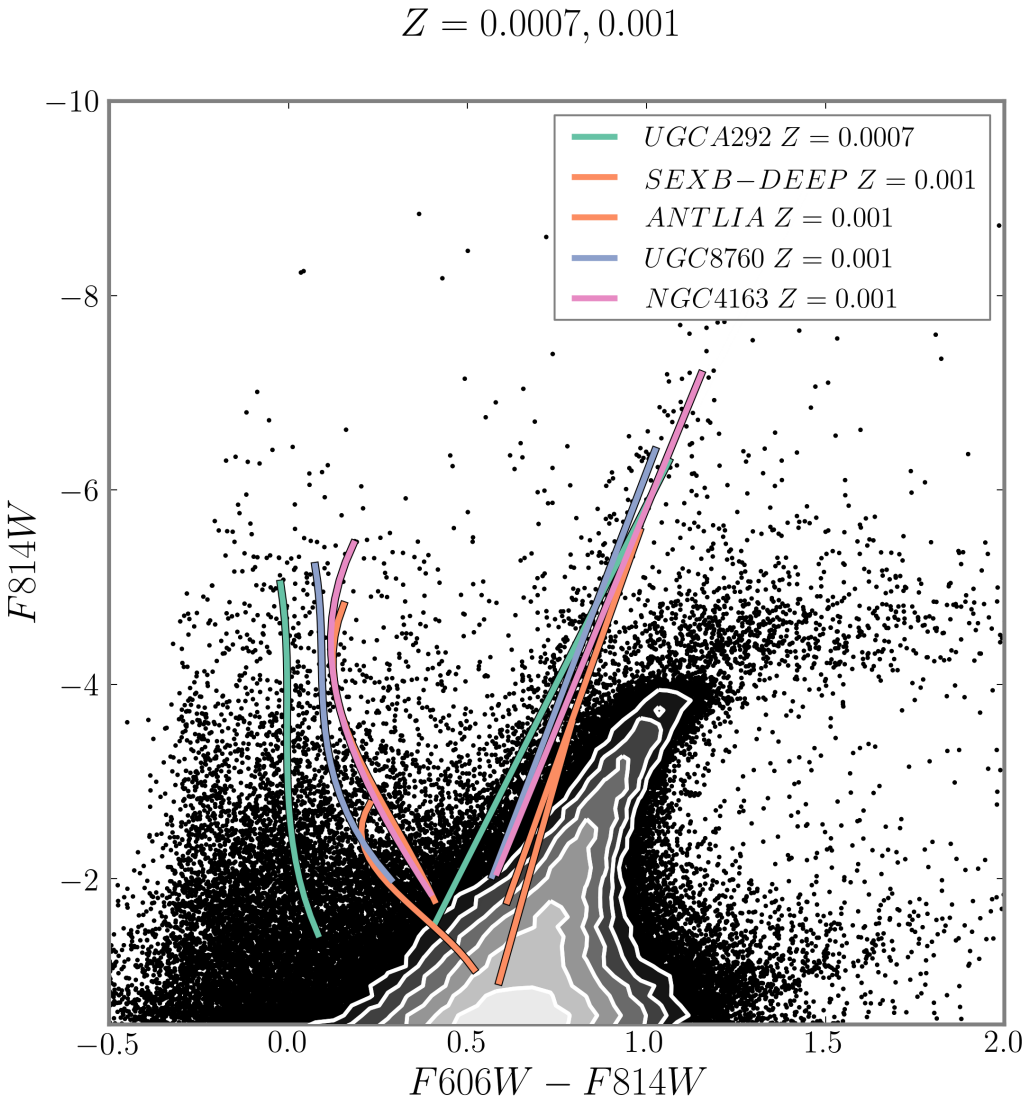

Figure 3.7 Optical ($F606W - F814W$) CMDs of sample galaxies with the BHeB and RHeB sequences identified with isochronal metallicities of 0.0007 and 0.001 (colored lines). Combined photometry of the galaxies are plotted below. Contours are drawn on areas of the cmd with a stellar density of at least 100 per CMD box of color width, 0.05 and mag height, 0.1. Contours are spaced logarithmically.

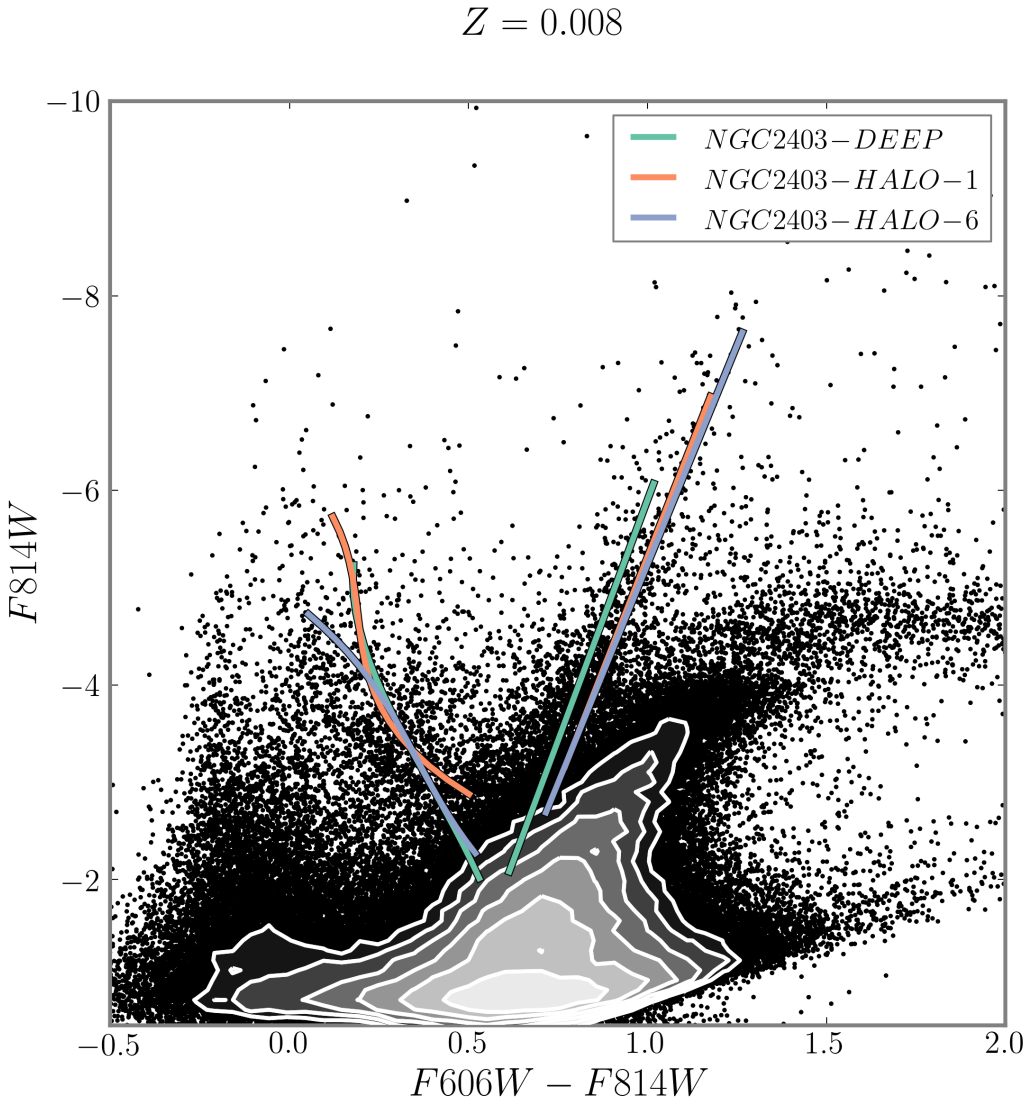

Figure 3.8 Same as Figure 3.7 but for $Z = 0.008$.

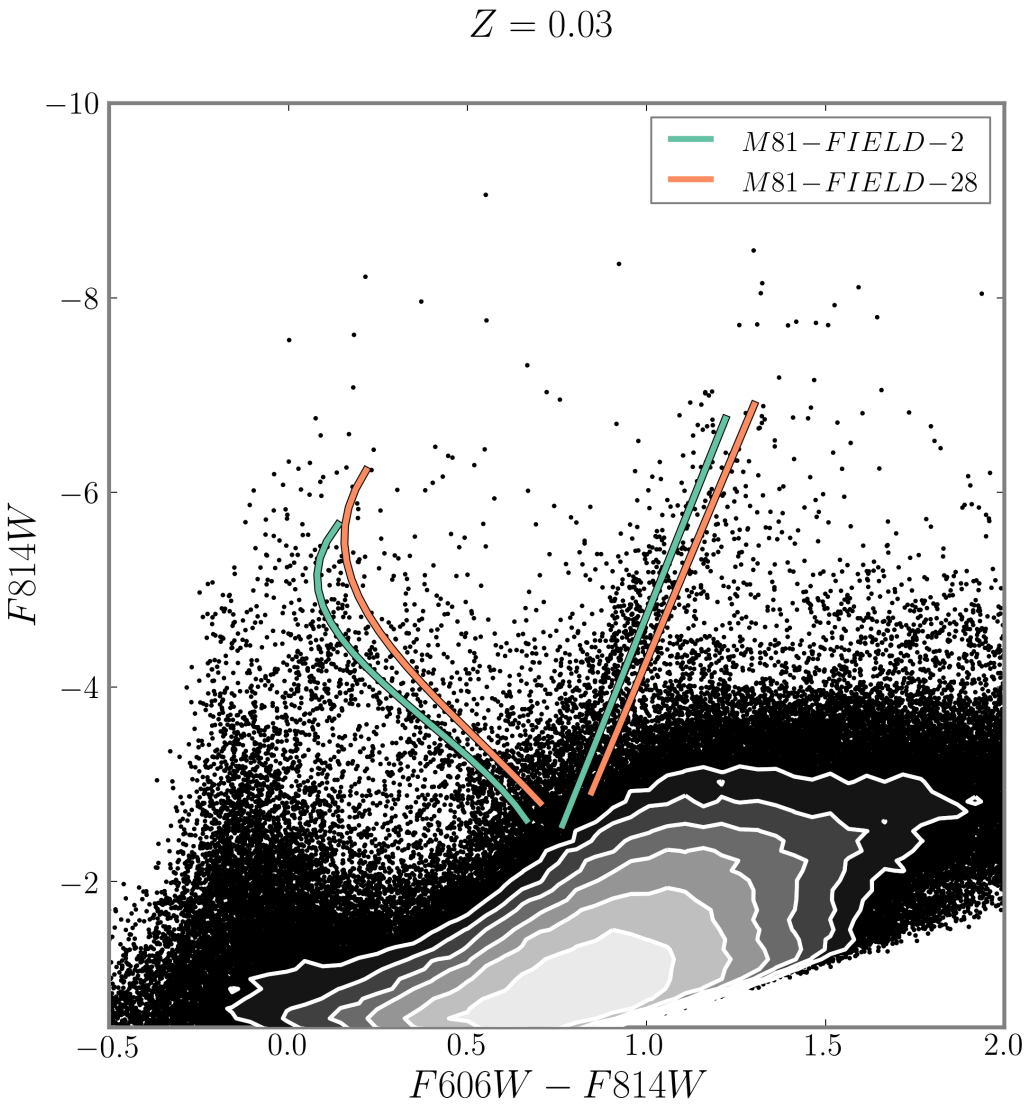

Figure 3.9 Same as Figure 3.7 but for $Z = 0.03$.

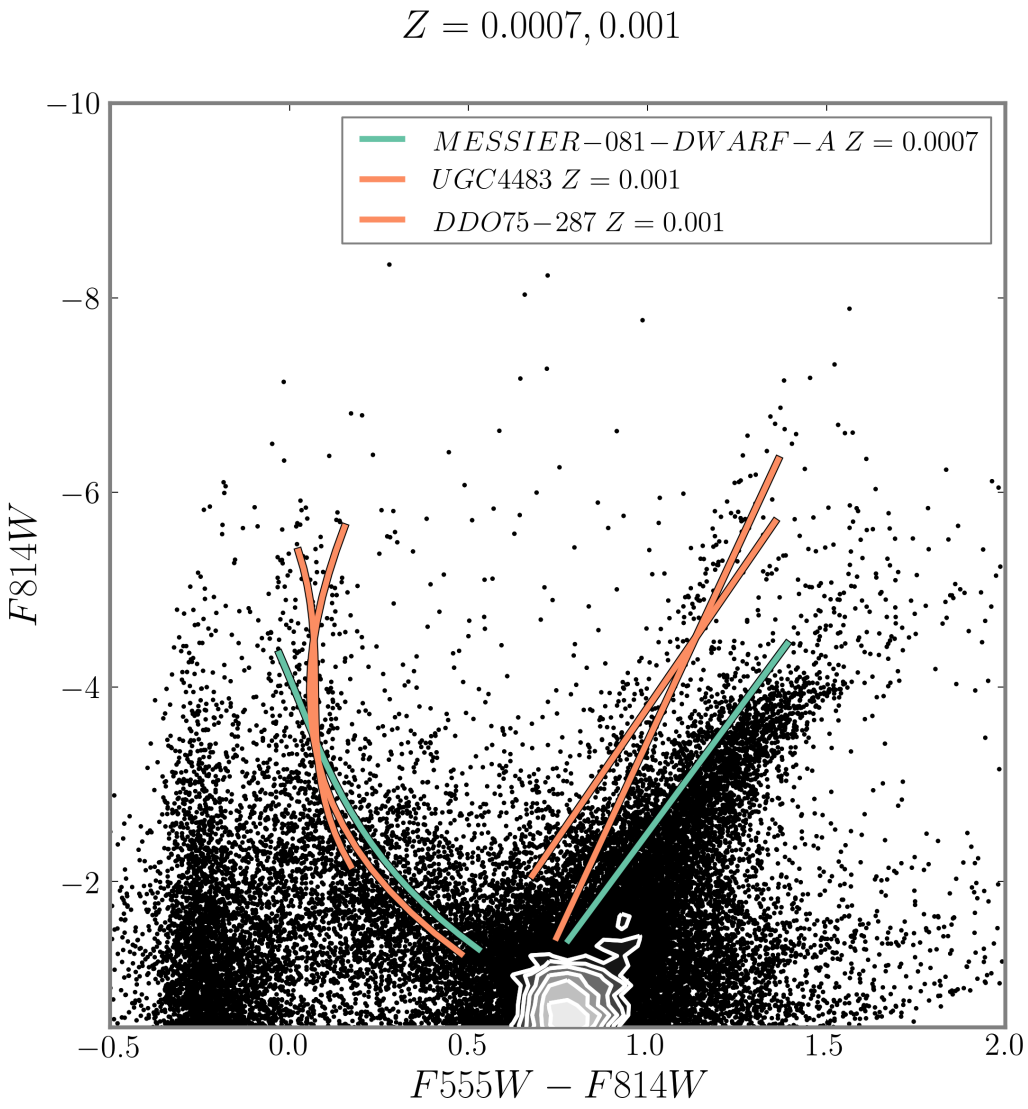

Figure 3.10 Same as Figure 3.7 but with $F555W - F814W$ and for $Z = 0.007$ and 0.001.

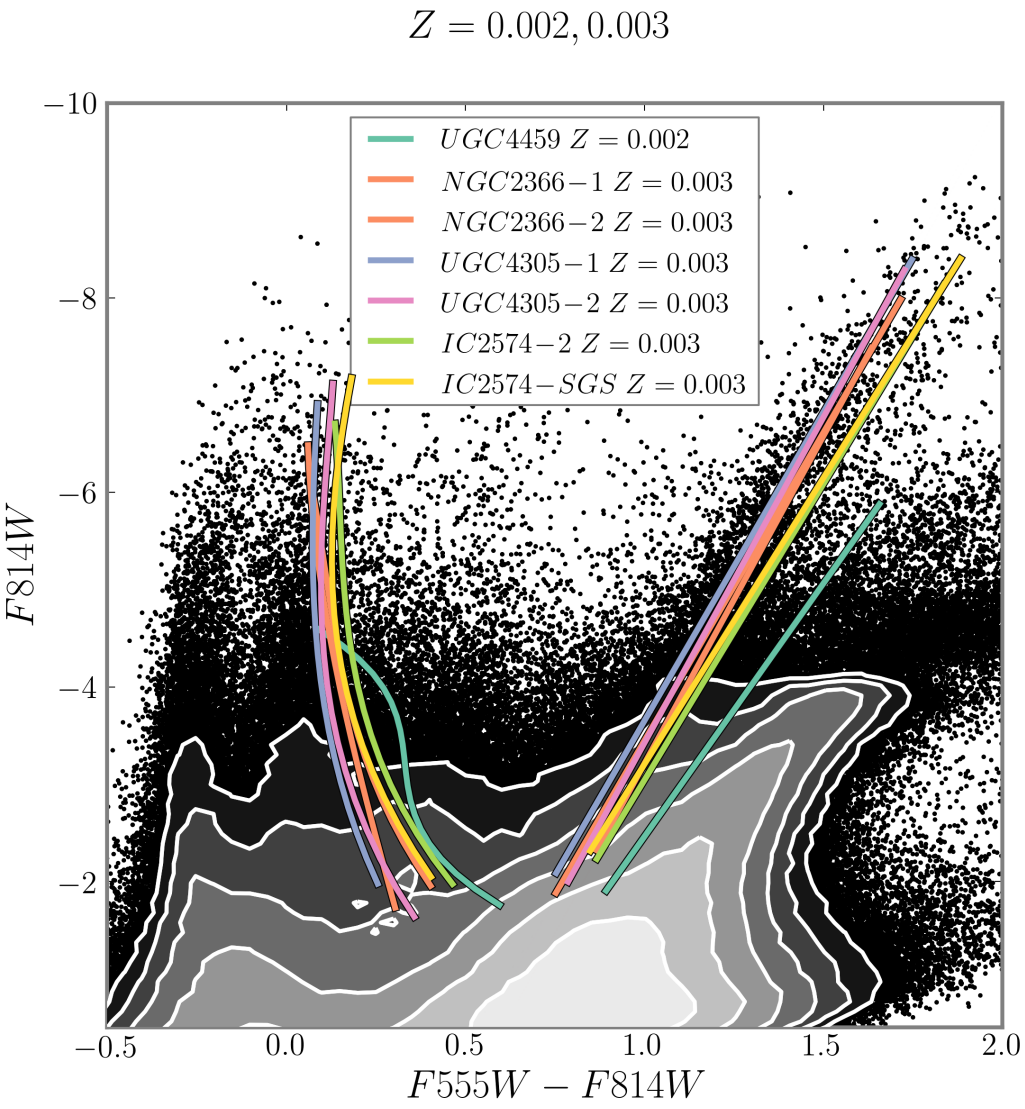

Figure 3.11 Same as Figure 3.10 but for $Z = 0.002$ and 0.003.

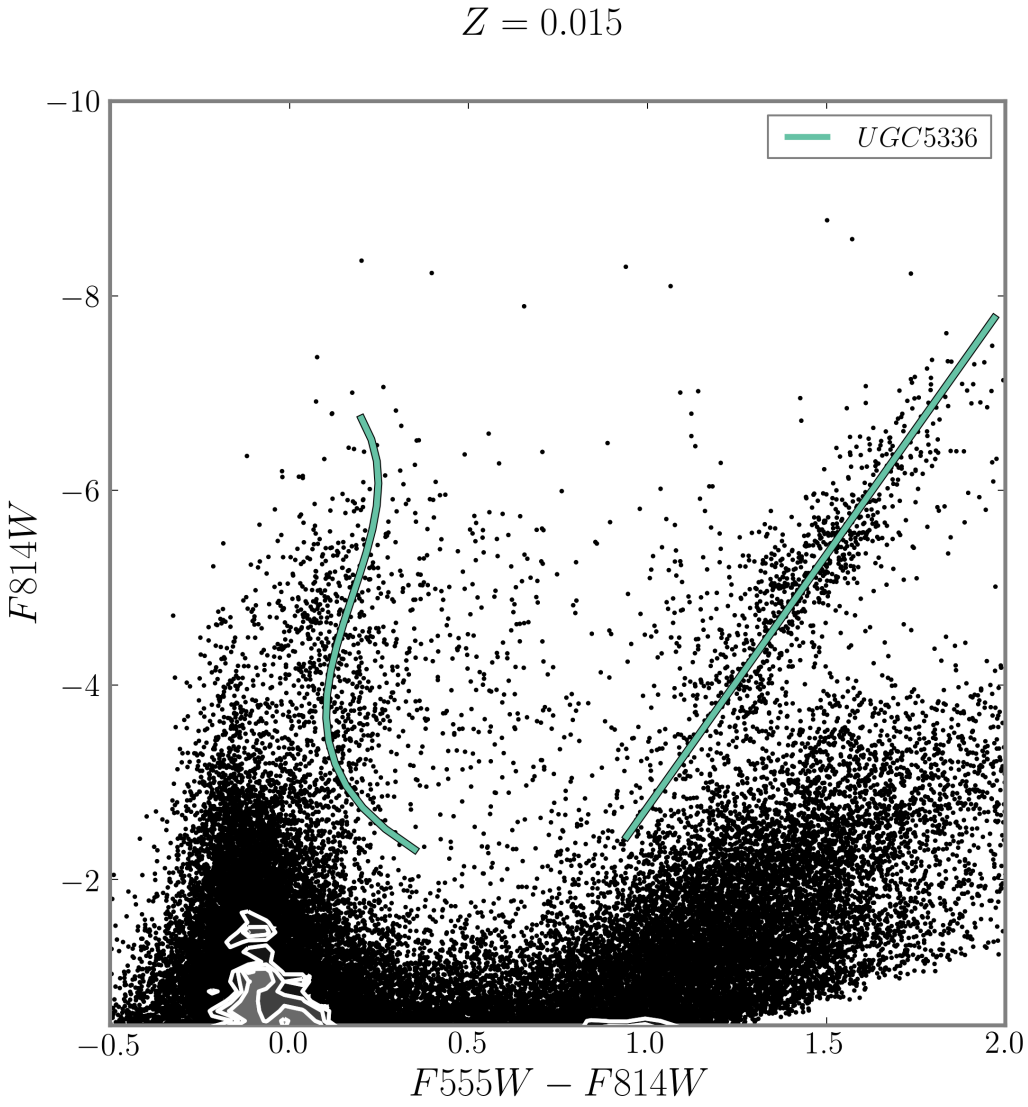

Figure 3.12 Same as Figure 3.10 but for $Z = 0.15$.

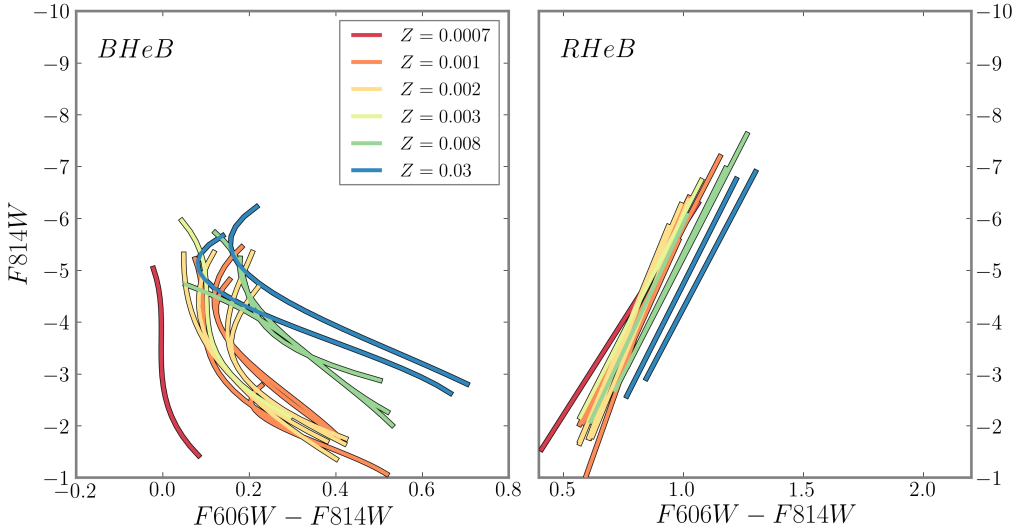

Figure 3.13 Optical ($F606W - F814W$) CMDs of all the BHeB and RHeB sequences identified in the data colored by nearest isochrone metallicity.

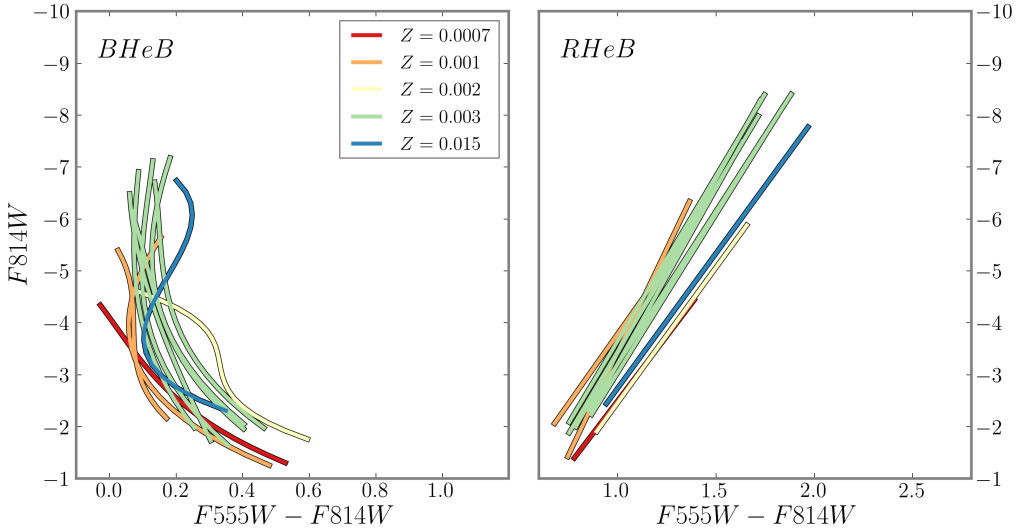

Figure 3.14 Optical ($F555W - F814W$) CMDs of all the BHeB and RHeB sequences identified in the data colored by nearest isochrone metallicity.

panels of Figures 3.15 and 3.16. First, low Λ_c tends to reduce the spread in color among isochrones of different metallicity. Second, low Λ_c tends to reduce the luminosity of the HeB stars, particularly at high metallicity. Third, the color separation of the RHeB and BHeB increases with increasing Λ_c. And finally, there is a slight increase in the RHeB slope as Λ_c increases.

With the differences in HeB sequences, we continue to the other observation test, the B/R ratio. For brevity, we initally limit our B/R ratio analysis to B12 models, and not each value of Λ_c. In addition, our method of determining the B/R ratio differs from M11 who did not have direct access to the stellar evolutionary tracks. To find the theoretical B/R ratio, M11 used Padova Stellar Evolution isochrones and populated simulated CMDs with SFHs previously derived using MATCH (McQuinn et al., 2009, 2010). Below, we show a method that avoids possible complications that are a result of mixing observational uncertainties with theoretical stellar evolution predictions (Section 3.5).

However, our method to measure the observed B/R ratio, is very similar to M11, though instead of populating simulated HeB sequence using isochrones, to find the age-magnitude relationship, we calculate stellar age-magnitude relationships directly from the stellar evolution models (transformed to magnitudes following Girardi et al., 2008a) for the BHeB and RHeB sequences. The observed B/R ratio is then calculated by taking the BHeB and RHeB stars' $F814W$ magnitudes and assigning them an age based on the age-magnitude relationship, and creating histograms of each sequence versus age. We chose to use the same age binning as M11, which is a span of log age (yrs) from 7 to 9 with steps of log age (yrs) 0.15.

The Theoretical B/R Ratio

The blue loops seen in Figure 3.2 are a relatively short lived phase, given that the He-burning lifetimes are typically $\sim 20\%$ of the H-burning lifetimes. Nevertheless, they contain a great deal of information because at a given mass, the amount of time spent in any evolutionary phase after the MSTO is proportional to the number of stars observed in that phase; see, for example, the fuel consumption theorem of Renzini & Buzzoni (1986a).

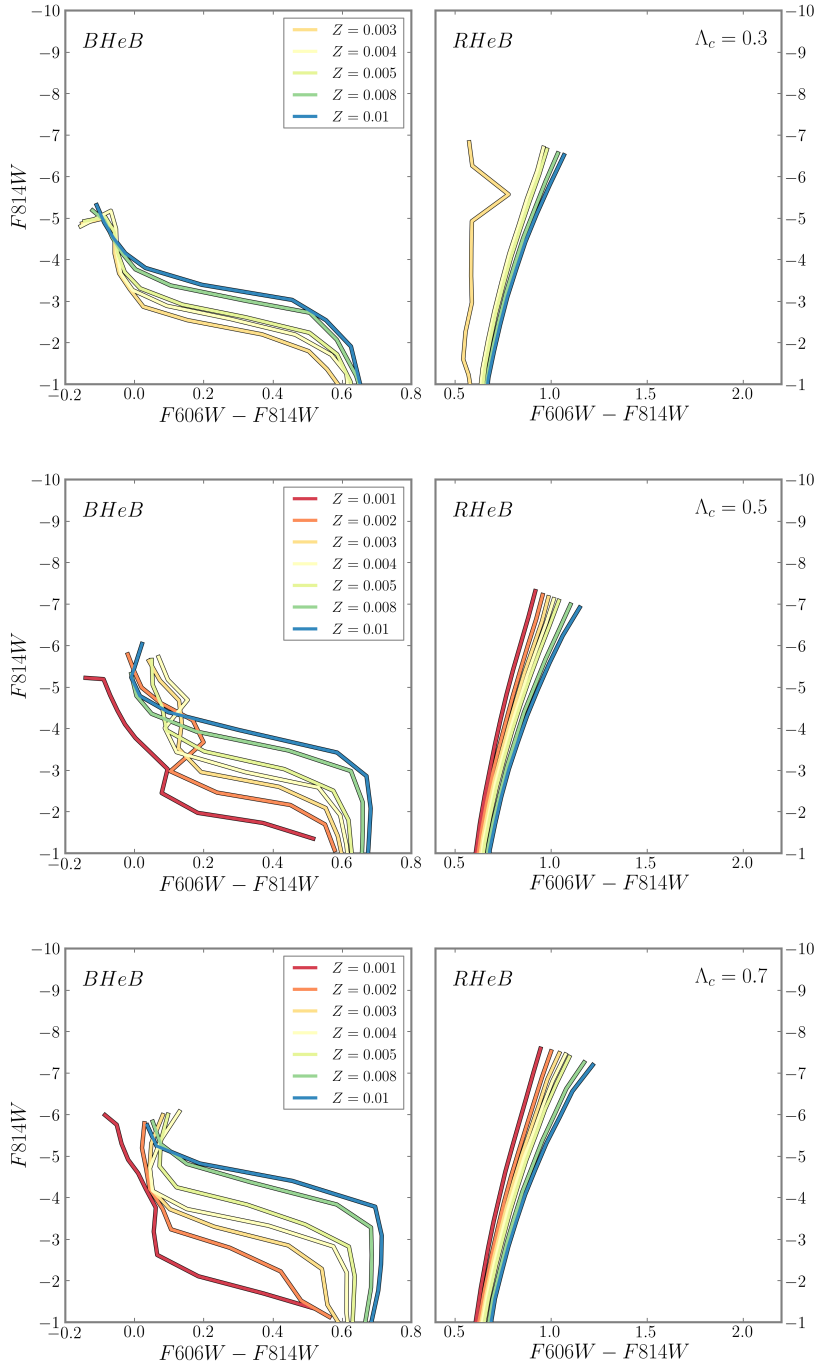

Figure 3.15 HeB Sequences ranging from $2 - 12 M_{\odot}$ for different Z and different Λ_c in *HST* optical filters (with no reddening or extinction). Increasing overshoot decreases the extension of the loops, as shown in Figure 3.5. Isochrone values of $M_{\rm bol}, L$ $T_{\rm eff}$ and $\log g$ were converted to HST filters with bolometric corrections from Girardi et al. (2008a).

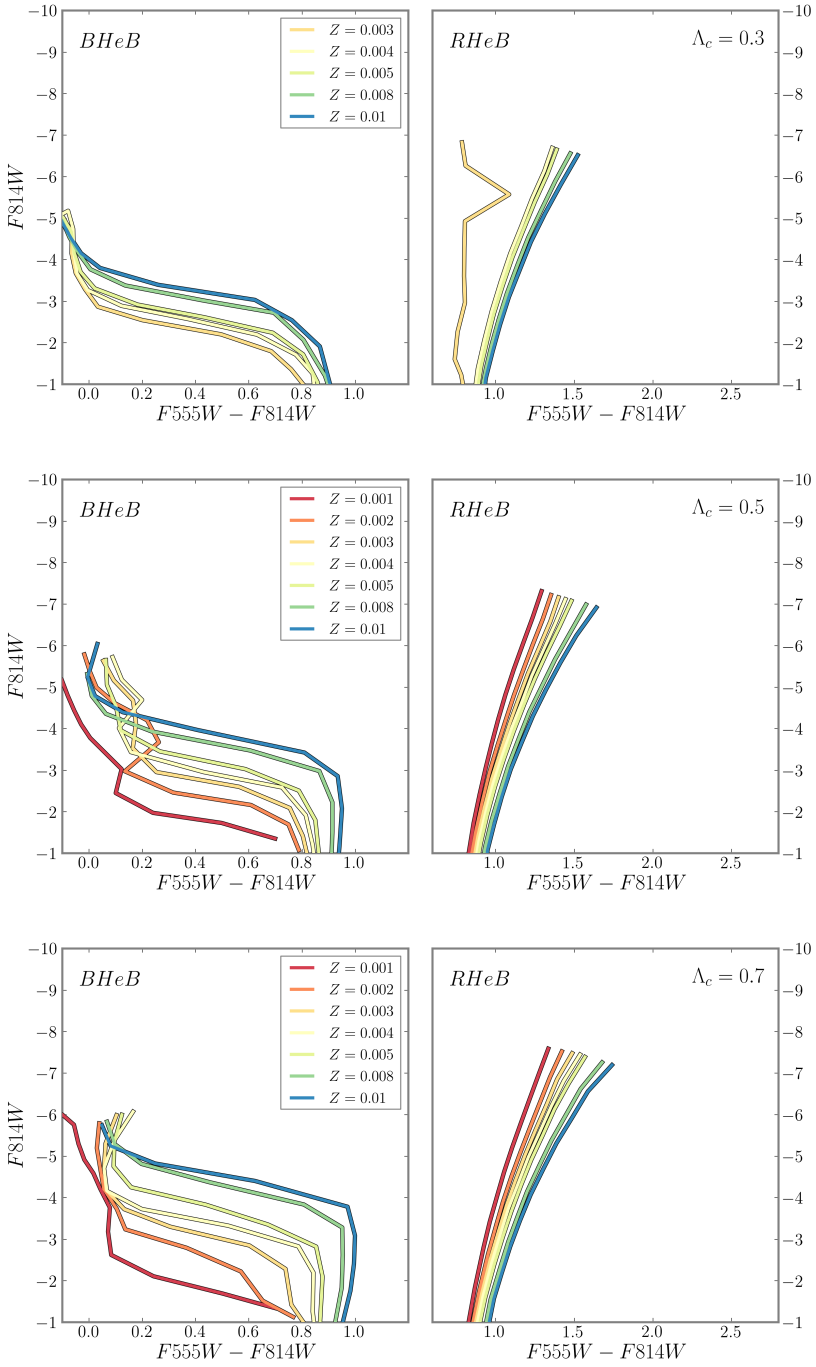

Figure 3.16 Same as Figure 3.15 but with $F555W - F814W$ CMDs.

While the observational B/R ratio is mostly concerned with counting stars in the BHeB and RHeB sequences, the theoretical B/R ratio can simply be a measurement from the stellar evolutionary tracks of the relative amount of time spent on the blue side of the loop compared to that on the red. Figures 3.17 and 3.18 shows this fraction as a function of main sequence turn-off age, defined as,

$$B/R \equiv \frac{\tau_{BHeB}}{\tau_{RHeB_1} + \tau_{RHeB_2}}, \tag{3.3}$$

where τ_{RHeB_1} is the time from the beginning of the loop to the median $T_{\rm eff}$ of the loop (T_{med}), τ_{BHeB} is the time from T_{med} to the maximum $T_{\rm eff}$ and back to T_{med}, and τ_{RHeB_2} is the time from T_{med} back to the Hayashi line. We only plot ages between 50 and 250 Myr because observations of nearby galaxies can only measure the B/R ratio of ages younger than 250 Myr, due to the BHeB merging with the RHeB near the RC (see discussion in Section 3.3 of M11).

The exact values of B/R clearly will depend on the age and metallicity of the stellar populations being analyzed. Indeed, the observed values of B/R cover a wide range, spanning between ~ 0.2 and ~ 1.5 in the observational literature. The lowest values of the B/R ratio are often seen in clusters of old, low mass stars (e.g., Woo & Demarque, 2001; VandenBerg et al., 2006), while higher values have come from asterosiesmology and binary star studies of younger, higher mass stars (e.g., Kamath et al., 2010).

The effects of varying strengths of core overshooting can be seen in Figures 3.17 and 3.18, which show the theoretical B/R ratio calculated from models with different values of Λ_c. Low Λ_c causes more extended loops with fractionally longer time spent on the BHeB. This trend is evident in the left panel, where the B/R ratio for $\Lambda_c = 0.3$ hardly dips below 2, that is, the BHeB lifetimes are at least twice as long as RHeB stars of the same age. On the other hand, for higher values of core overshooting, ($\Lambda_c = 0.7$, right panel), the opposite effect is seen, B/R is almost always less than 2 at all ages. In short, if observations suggest that B/R ratio is smaller or larger than expected, Λ_c should be increased or decreased compared to the fiducial $\Lambda_c = 0.5$ in the B12 models.

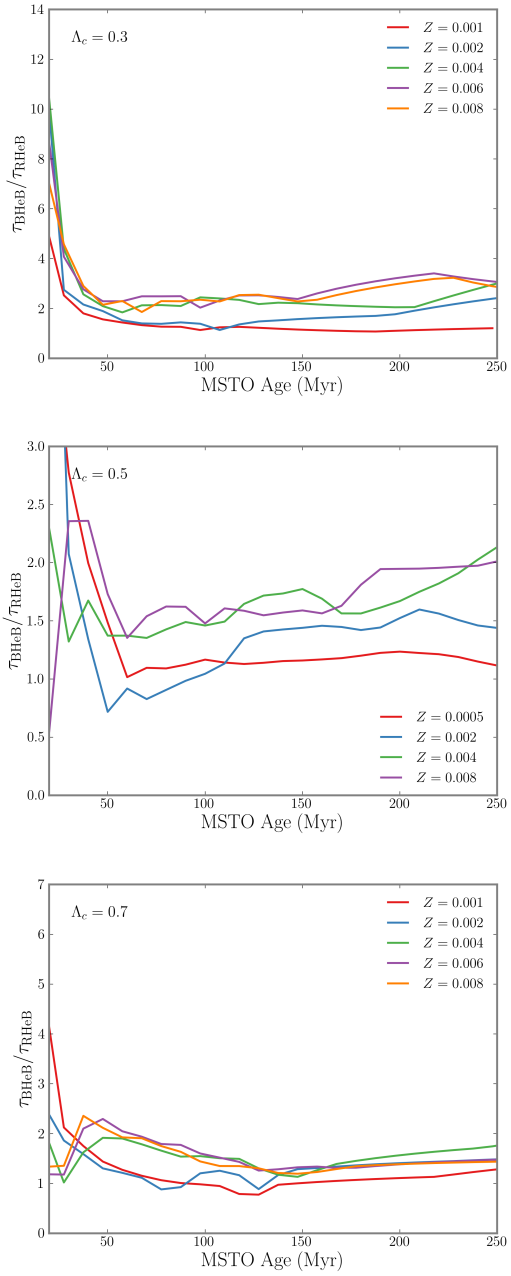

Figure 3.17 The predicted B/R ratio with $\Lambda_c = 0.3, 0.5$ and 0.7 (top to bottom) at lower metallicities. High ratio values at young ages and missing data are evidence of the HeB failing to undergo a blue loop. A slight metallicity effect can be seen at old ages, where the B/R ratio increases with increasing metallicity. Vertical axes are not at the same scale to emphasize the dynamic range of each panel)

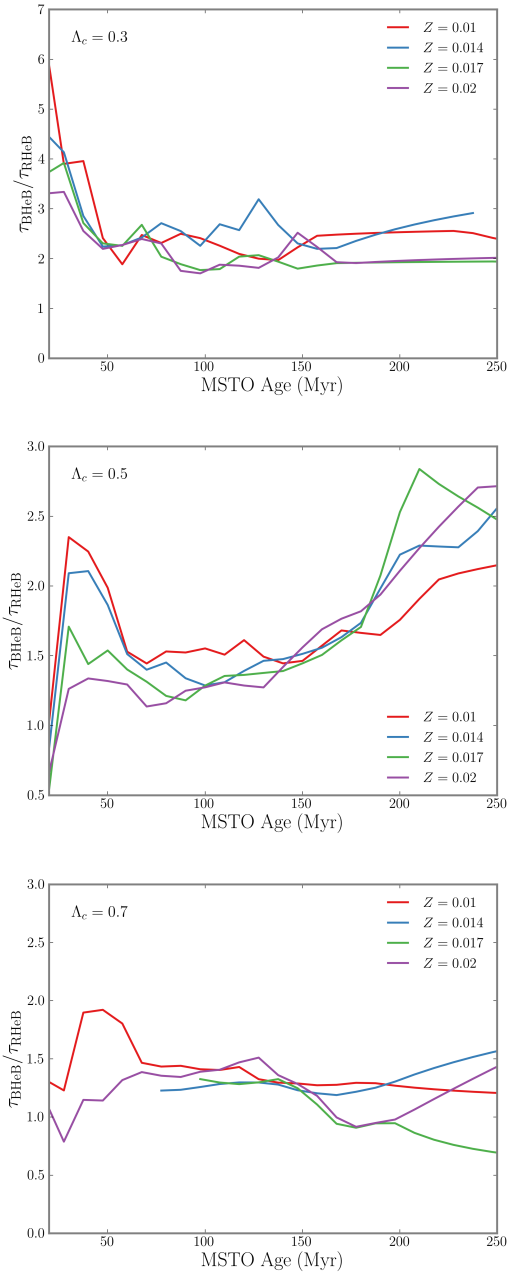

Figure 3.18 The predicted B/R ratio with $\Lambda_c = 0.3, 0.5$ and 0.7 (top to bottom) at higher metallicities. High ratio values at young ages and missing data are evidence of the HeB failing to undergo a blue loop. Unlike the lower metallicities (Figure 3.17, the does not seem to be a metallicy effect. Vertical axes are not at the same scale to emphasize the dynamic range of each panel)

Age-Magnitude Relationships with $\Lambda = 0.5$

As we have seen, the theoretical age-magnitude relationship for HeB stars underpins observational B/R ratio measurements. To measure B/R one wishes to compare the numbers of BHeB and RHeB stars of the same age (or nearly the same mass). However, the magnitudes of BHeB and RHeB stars are different for the same mass, with the exact magnitude difference dependent on the metallicity and the details of the stellar model. It is therefore necessary to correct for the fact that RHeB stars do not follow the same age-magnitude relationship as BHeB stars.

To compare the B/R ratios in our galaxy sample consistently with those reported in M11, we use only the B12 models to calculate the age-magnitude relationship and then the B/R ratio.

Figure 3.19 shows the age-bolometric magnitude relationship of the BHeB (left) and RHeB (middle) sequences. Shown on the right-most panel is the color difference in bolometric magnitude between the RHeB and BHeB as a function of isochronal age. At low metallicities, the color separation of the models is monotonically bluer with increasing age. However after $Z = 0.002$, the color separation at old ages instead becomes redder. This variation is determined by whether or not convection in the envelope of the star is quenched during the BHeB.

With these age-magnitude relationships we can assign a probable age to every HeB star, in the same way described in M11 and Dohm-Palmer & Skillman (2002).

3.5.1 B/R Ratios of the Galaxy Sample with B12

Figures 3.21 - 3.25 show the B/R ratio calculated for each galaxy (with random uncertainties, shaded light grey) and averaged (solid black), as well as the theoretical B/R ratio (dashed). The bottom of each panel has an comparison of the data and model, $B/(B+R)_{\rm data} - B/(B+R)_{\rm model}$. We now examine the B12 B/R ratios.

We see the same effect at young ages in the B12 theoretical B/R ratios as seen in the Padova models in M11. Namely, a B/R ratio too high at young ages and general agreement elsewhere. Further, the observed and theoretical B/R ratios do not change appreciably as

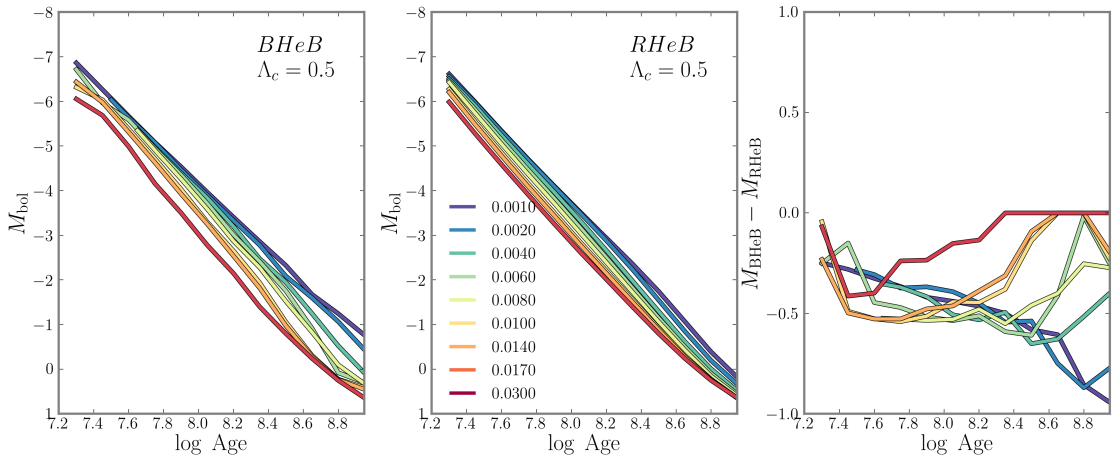

Figure 3.19 Age magnitude relationships for B12 models for the BHeB (left) and RHeB (right). Also plotted is the change in HeB magnitude as a function of BHeB age.

a function of age, at least in the recent 250 Myr examined here.

The observed B/R ratio does not seem to change appreciably as a function of metallicity, and is always between $\sim 0.5 - 1.0$. However, the B12 theoretical B/R ratio increases in metallicity from $\sim 0.75 - 2$. There seems to be a slight metallicity dependence in the observed and theoretical matching at ages older than ~ 50 Myr. The B12 theoretical B/R ratios seem to agree better with the observed B/R ratios at lower metallicities than at higher.

In summary, the observed B/R ratios with the B12 age-magnitude relationship broadly agree with M11 where the metallicities in the samples overlap, that is, the B/R ratio we measure using the B12 models follows the same trends in age for each metallicity within observational uncertainties (which include photometric uncertainties and Poisson errors, and can be a large percentage of the value, see M11). Specifically, M11 found the B/R ratio can begin high at young ages, and tends to drop to B/R $\sim 1 - 1.5$ at older ages. This is evidence that the model HeB stars have incorrect lifetimes.

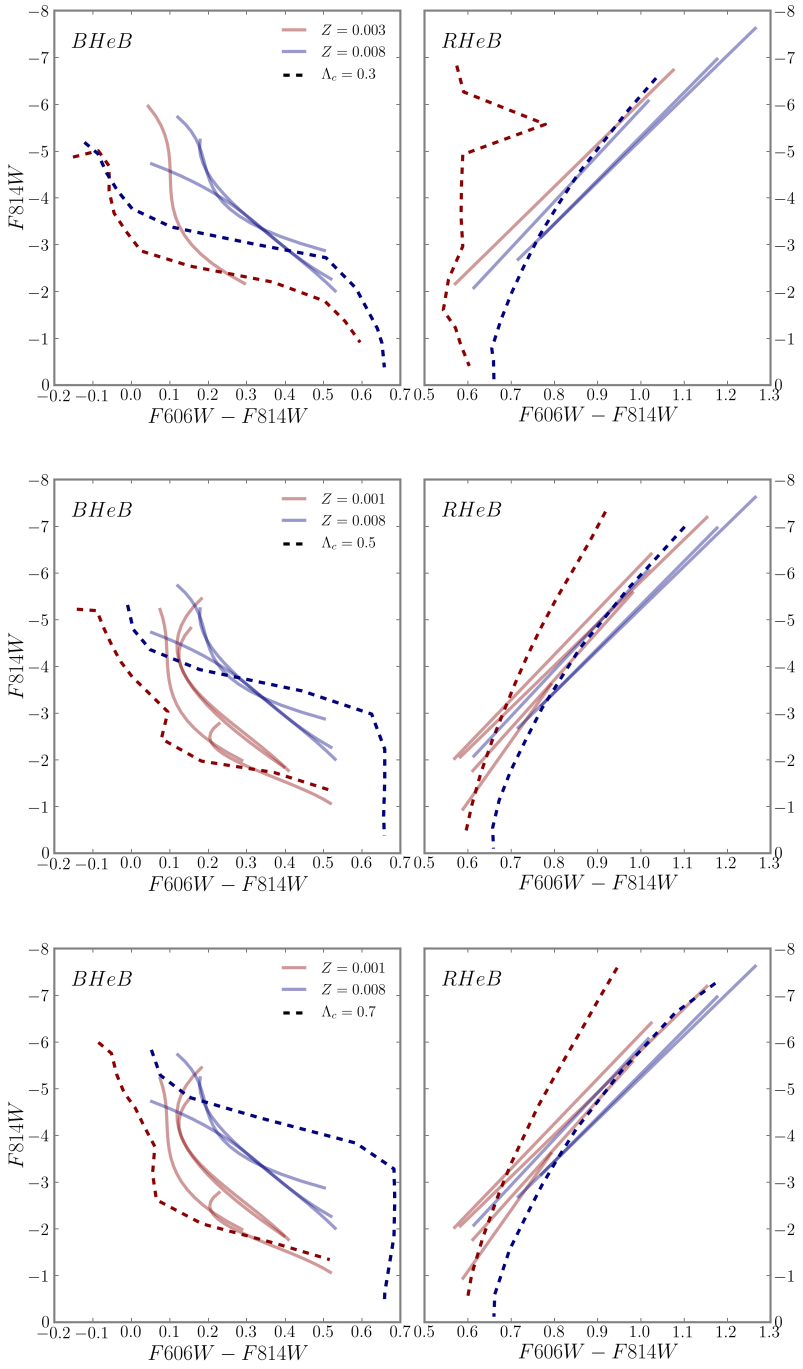

Figure 3.20 Theortical HeB Sequences ranging from $2-12M_{\odot}$ for different Z (dotted) and different Λ_c (increasing from top to bottom) in HST optical filters (with no reddening or extinction). Observationally measured HeB sequences are shown in solid lines). Increasing overshoot decreases the extension of the loops, as shown in Figure 3.5. Isochrone values of $M_{\rm bol}, L$ $T_{\rm eff}$ and $\log g$ were converted to HST filters with bolometric corrections from Girardi et al. (2008a).

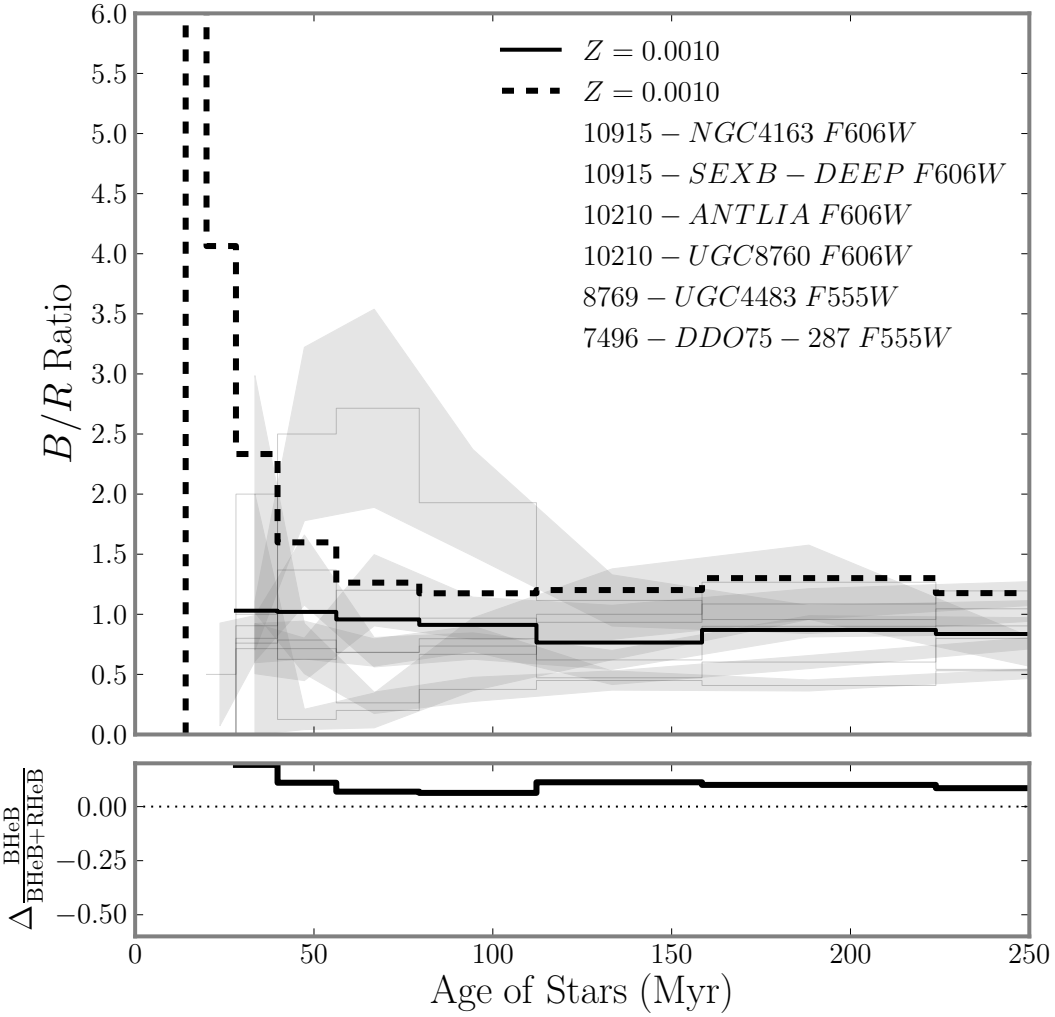

Figure 3.21 Measurements of the B/R ratio binned into sub-figures by isochronal metallicity. Two panels for each sub-figure. Top panel shows the observed B/R ratio (measured by applying the age-magnitude relationship to HeB stars) for each field (light gray) and the mean B/R ratio of the combined fields (black, solid). Over-plotted is the theoretical B/R ratio (black, dashed). The bottom panels show the fraction difference between the observed and theoretical B/R ratio. The theoretical B/R ratio was calculated directly from the stellar evolution tracks, if tracks were not calculated at the exact metallicity, the nearest metallicity calculated is shown.

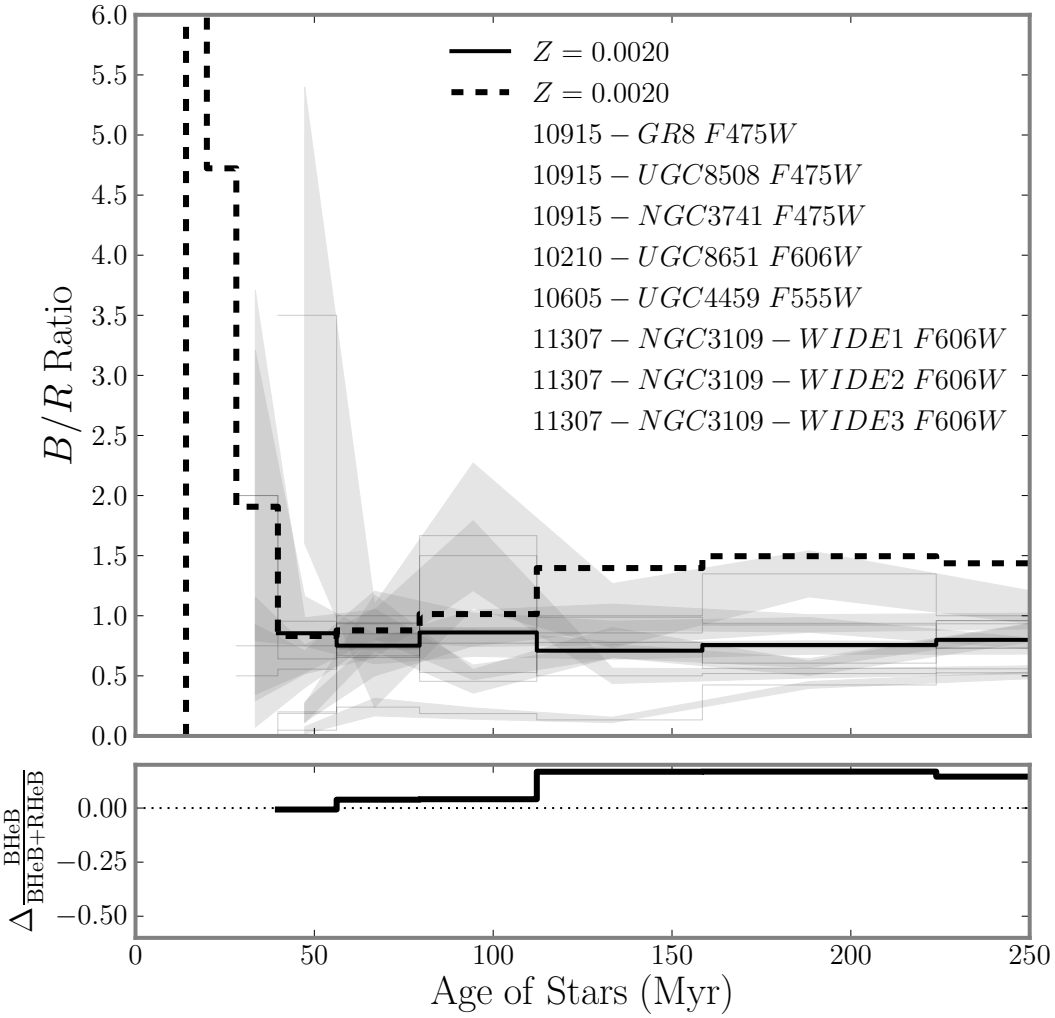

Figure 3.22 Same as Figure 3.21 but for galaxies with isochronal metalicity $Z = 0.002$.

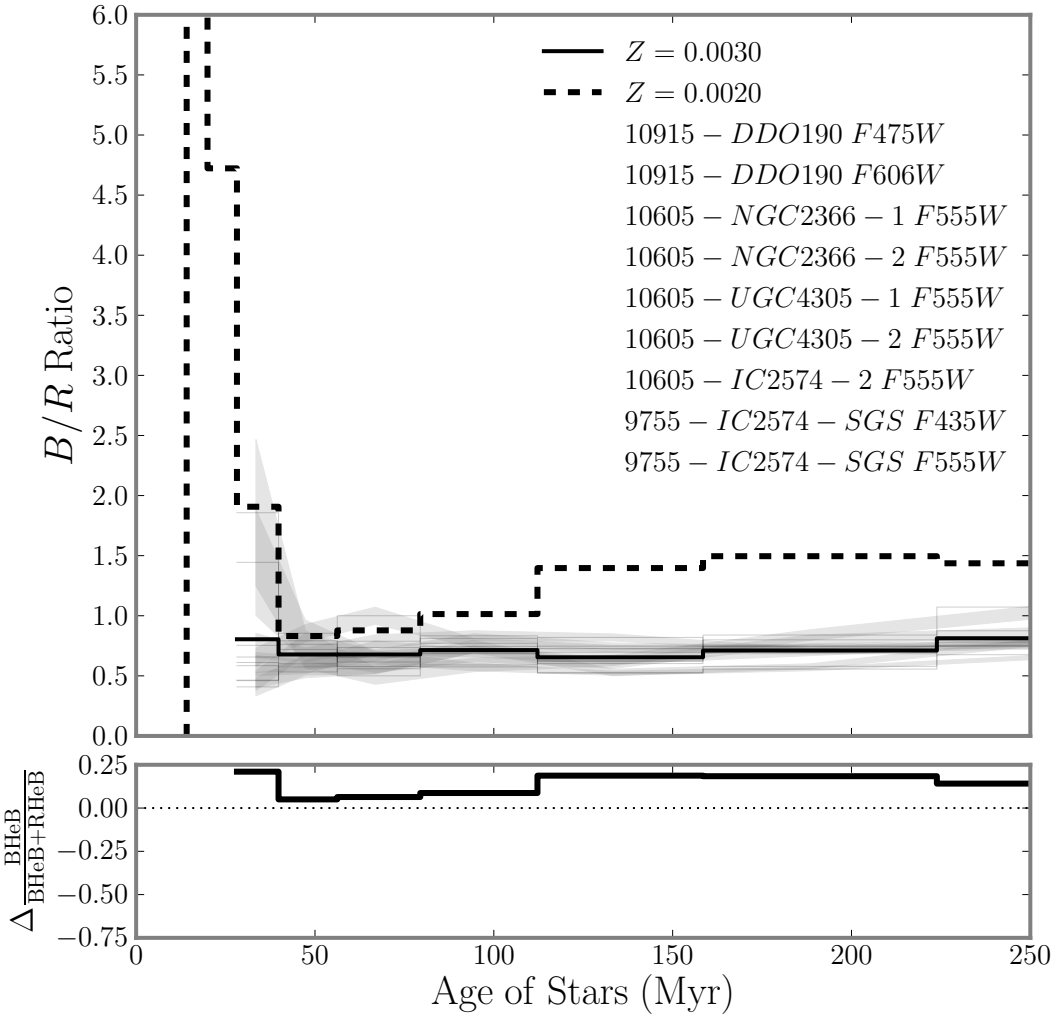

Figure 3.23 Same as Figure 3.21 but for galaxies with isochronal metalicity $Z = 0.003$.

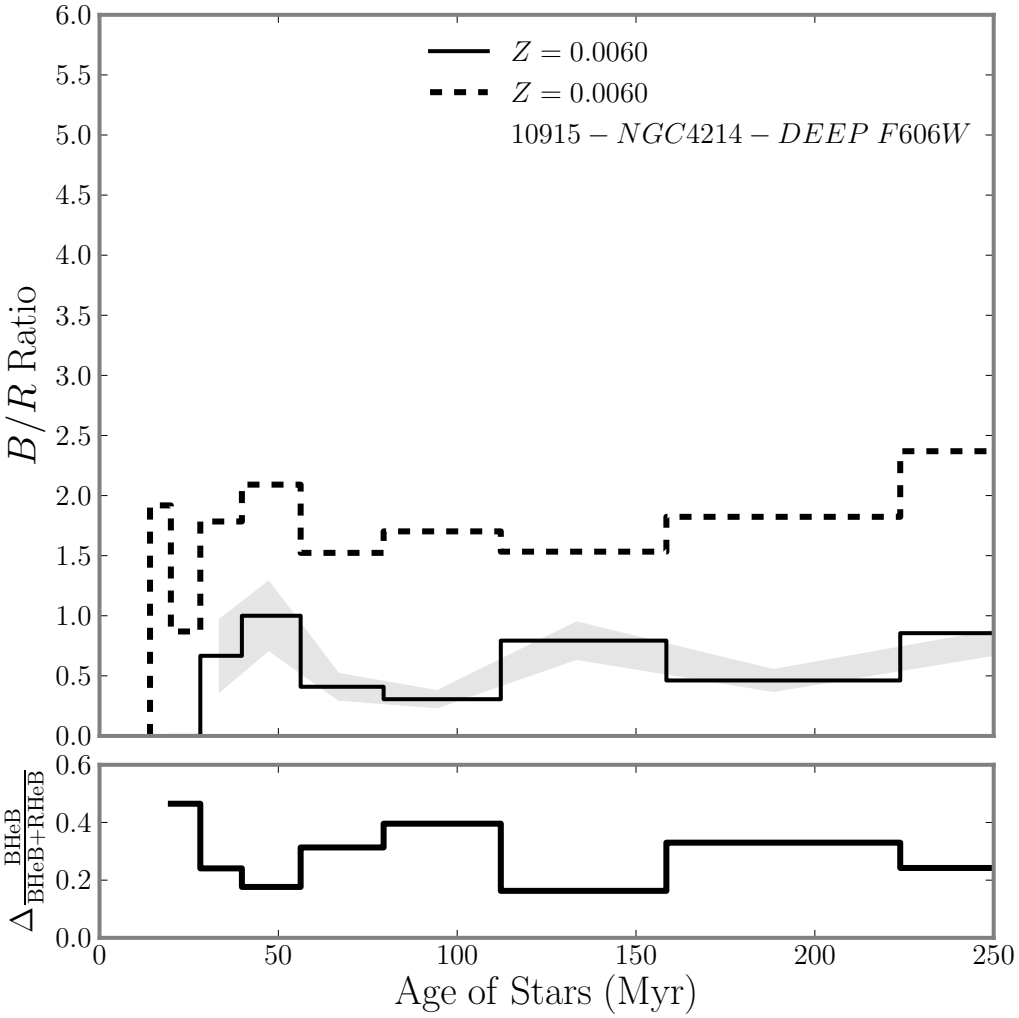

Figure 3.24 Same as Figure 3.21 but for galaxies with isochronal metalicity $Z = 0.006$.

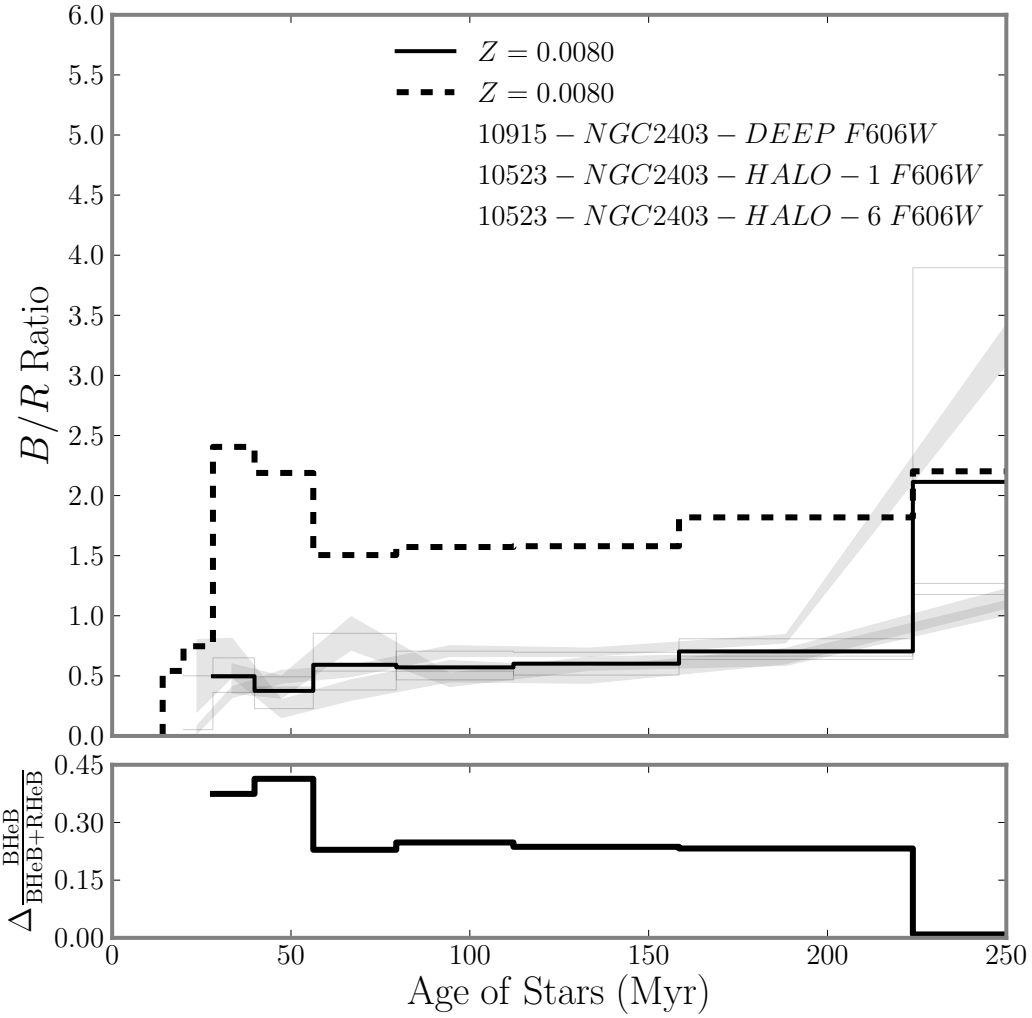

Figure 3.25 Same as Figure 3.21 but for galaxies with isochronal metalicity $Z = 0.008$.

3.6 Discussion

The deviations from the B12 model B/R ratios and HeB sequences in our nearby dwarf galaxy observations agree with those of M11. M11 reported four major conflicts with models: 1) color offsets for the bright ($M_V \sim -4$ mag) BHeB (of order +0.15); 2) for young ($\lesssim 50$ Myr) stars, the theoretical B/R ratio is higher than observed (in this case, the theoretical B/R ratio is calculated from simulate CMDs created by populating isochrones with a chosen IMF, binary fraction, photometric uncertainties, and previously determined observationally derived star formation history); 3) faint BHeB stars are observed to be bluer than isochrones predictions; and 4) the RHeB slope is shallower than isochrones by a factor of ~ 3 which was also observed as bright ($M_V \sim -4$ mag) RHeB color offsets (~ -0.5 mag).

To rephrase the findings in terms more relevant to stellar interiors, for stars with $0.001 < Z < 0.008$: 1) The BHeB temperature is too high for stars with $M \gtrsim 5 - 6M_{\odot}$; 2) Stars with $M \gtrsim 7M_{\odot}$ spend relatively too long on the BHeB sequence; 3) The BHeB temperature is too low for stars with $M \lesssim 4 - 5M_{\odot}$; and 4) The RHeB sequence does not simply follow a Hayashi line.

We will now address these issues, in view of what adjustments to the core overshooting parameter can improve the model to data fitting.

Items 1 and 2 could both be allayed with a higher value of the core overshooting parameter. As we have seen in Figure 3.5, an increase in core Λ_c decreases the extent of the loop and shortens the total HeB lifetime, as well as the fraction of the HeB lifetime spent on the BHeB sequence.

However, increasing core overshooting would further exacerbate the $T_{\rm eff}$-mismatch stated in Item 3, since it would decrease even further the predicted maximum temperature of the lower mass blue loops. Instead, a decrease in Λ_c is necessary to mitigate the differences seen at lower masses. In other words, M11's findings suggest that, at least for the HeB phase, the strength of core overshooting should be increased at high masses ($M \gtrsim 7M_{\odot}$) but decreased in lower masses ($M \lesssim 5M_{\odot}$), compared to the standard models with $\Lambda_c = 0.5$.

Implementing such a mass-dependent prescription will change the predicted colors of the HeB sequences. For example, BHeB stars of lower mass with lower Λ_c will have bluer colors,

while BHeB stars with higher masses and higher Λ_c will be redder, with less extended loops (both in color and time). The net effect will be a more vertical BHeB sequence, whereas the RHeB will have a slightly decreased slope compared to the current PARSEC models. These are both welcome changes when attempting to reproduce the observed HeB sequences in the data.

As an aside, for Item 4, the mismatch in slope of the RHeB on a CMD is problematic and its origin is unclear. It may have little to do with stellar interior models because these stars are all essentially on the Hayashi line, and have little freedom in their models. Instead the mismatch seems to more likely be a result of inadequate stellar atmosphere models and synthetic colors.

As a first attempt to quantify mass dependent core overshooting (MDCOS), we implement a simple prescription for using modifications of the PARSEC models. We combined the three stellar evolutionary grids at different mass ranges:

$$\Lambda_c = 0.3 : 2.5 < M < 5.M_{\odot} \tag{3.4}$$

$$\Lambda_c = 0.5 : 5. < M < 5.6M_{\odot} \tag{3.5}$$

$$\Lambda_c = 0.7 : 5.6 < M < 20M_{\odot}, \tag{3.6}$$

for the range of metallicities from $Z = 0.001 - 0.03$. As before, we create HeB sequences by interpolating isochrones of these new models. Then we created a sequence of isochrones to match the metallicities found in the data. In some cases ($Z = 0.011, 0.015, 0.018$) we interpolated between two sets of differing compositions to find the isochrones at that metallicity. This is an initial implementation, which is motivation for future stellar evolution codes to include and test mass dependent core overshooting.

We now discuss the color and magnitude distributions of the HeB sequences with this new model, followed by the age-magnitude relation which leads to the B/R ratio.

HeB Sequences with MDCOS

Figure 3.26 is the same as Figure 3.20 except with models calculated with the MDCOS prescription above. Perhaps the most obvious change in the HeB sequences with MDCOS

is the color separation between the BHeB and RHeB. As expected, the BHeB now follows a much more vertical sequence in the right panel of Figure 3.26, a feature which is also seen in the data (Figures 3.7 -3.12 and also the galaxies studied in M11). In other words, less massive (fainter) HeB stars have more extended loops while more massive (brighter) BHeB stars have less extended loops.

Individually,the BHeB sequences show several differences between MDCOS and B12. For MDCOS, the BHeB is bluer than B12 for $F814W > -4$ and redder at brighter magnitudes. In the lowest metallicity tracks however the MDCOS BHeB sequence is redder than the BHeB sequence of B12. These changes explain the better fit of the MDCOS prescription.

While MDCOS follows the same trends as the observed BHeB, it possibly becomes too blue as metallicity increases. To illustrate this, in Figure 3.27 we show the bolometric color difference between the BHeB and RHeB sequences as a function of bolometric magnitude. The bluer BHeB sequences are evident by the left panel shifted to positive values in color, in other words, much redder. It is also clear the metallicity variations are diminished in MDCOS compared to B12. Metallicity variations are also not obvious in the data (see Figures 3.15 and 3.15). These trends in MDCOS are a direct result of the changing core overshooting with mass.

Implementing MDCOS, however, does not solve the mismatches between the model and observed RHeB color and magnitude sequences. MDCOS has little impact on the RHeB, such that whatever discrepancies exist with B12 will also exist with MDCOS. The fact that MDCOS fails to fix the model RHeB suggests we must look elsewhere for possible resolutions. For example, model atmospheres are notoriously complex for cool evolving stars, and also the mixing length parameter, which is calibrated with Solar data (Bressan et al., 2012), may be incorrectly extended to RHeB stars.

It is possible the data-MDCOS model matching is more offset with increasing metallicity, suggesting there may be a smaller order metallicity dependency on Λ_c. Alternatively, the increasing offsets with increasing metallicity may be a sign that another convective parameter, namely the strength of overshooting at the base of the convective envelope, is more sensitive to metallicity than it is to mass. Higher amounts of envelope overshooting can increase the temperature extension of the blue loop, but generally has little effect compared

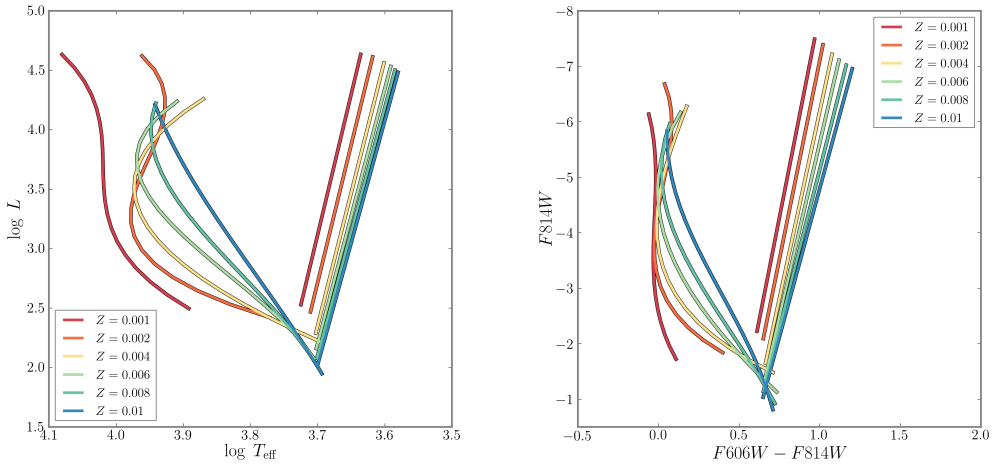

Figure 3.26 HeB sequences with MDCOS. Left: HRD, right: CMD in HST filters. Compared to Bressan et al. (2012, See Figure 3.20 middle panel), fainter loops are more extended, while brighter loops are less extended.

to overshooting in the core. Whether or not this parameter is degenerate with Z would help to constrain models, but is beyond the scope of this chapter.

Age-Magnitude Relationships MDCOS

This revised MDCOS prescription changes the relationship between stellar mass and position in a CMD, and will thus have a direct impact on inferring the SFHs from the populations of the HeB sequences. In star formation history modeling, the recent SFH is adjusted to match the number of stars in the HeB sequence as a function of magnitude. Revisions in HeB models will therefore produce changes in the inferred ages.

Figure 3.28 shows the age-bolometric magnitude relationships for models with MDCOS. For young, high mass stars with $M_{bol} < -3$, this relationship is steeper compared to B12 , and changes slope when Λ_c is abruptly changed. In addition, MDCOS is brighter at older ages compared to the current PARSEC models.

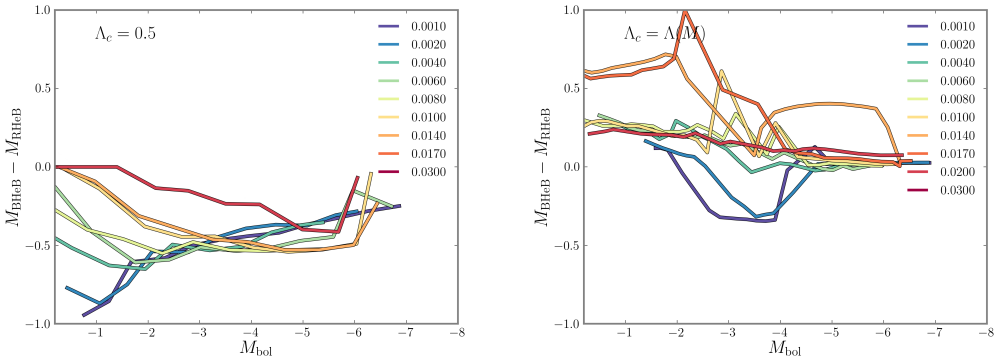

Figure 3.27 Change in bolometric mag on the BHeB and RHeB as a function of BHeB magnitude for B12 (left) and MDCOS (right)

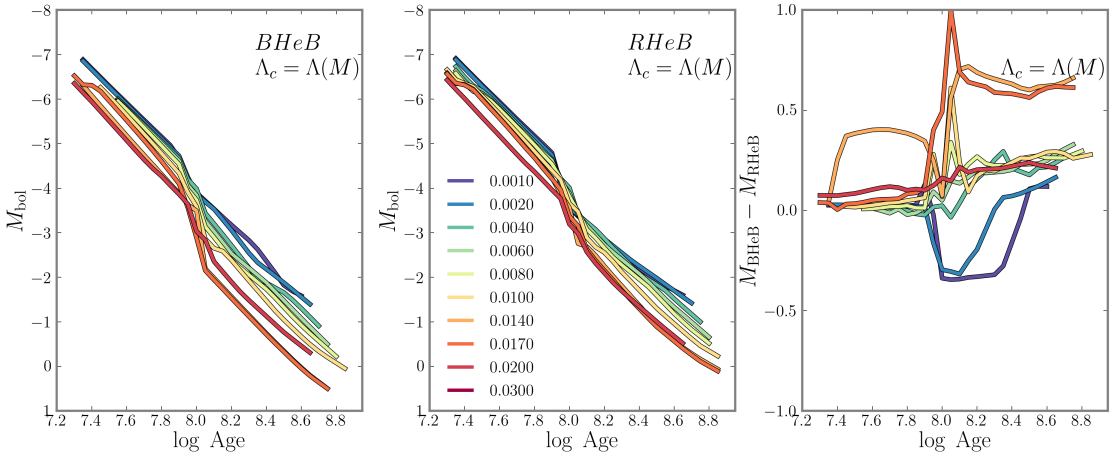

Figure 3.28 Age magnitude relationships for MDCOS for the BHeB (left) and RHeB (right). Also plotted is the change in HeB magnitude as a function of BHeB age.

The B/R Ratios with MDCOS

With this age-magnitude relationship, we can now measure the observed B/R ratio in our galaxy sample with a MDCOS prescription.

Figures 3.29 - 3.36 are the same layout as Figures 3.21 -3.25. They show the B/R ratio as a function of age for each galaxy field (light grey) grouped by metallicity. To decrease uncertainties due to limited numbers of stars in a given age bin, we also plot the averaged observed B/R ratio for all the galaxies of a given metallicity (solid black). The theoretical B/R ratio is shown as a dashed black line. We plot the fractional difference between the observed and theoretical B/R ratio in the bottom panels. In all panels we have converted magnitudes to age using the theoretical relationship of the model being used in the comparison.

The RHeB changes very little with these models since we only are changing the strength of core overshooting. Stars with the largest convective envelopes possible will adjust to any core overshooting changes because core overshooting effects mixing much more than it does energy transport. Therefore, all B/R ratio changes are driven almost entirely by changes in the BHeB lifetimes.

As we have shown and M11 have found, the B/R ratio from low metallicity nearby galaxies generally match the Padova models for ages between ∼50 and ∼250 Myr. Younger than ∼ 50 Myr, however, the B12 model and Padova models over predicted the B/R ratio at all the metallicities in their galaxy sample ($0.001 \lesssim Z \lesssim 0.009$). These conclusions as far as the B/R ratio go may be suspect as they depend on the propagation of HeB models that did not describe the HeB sequences in the data. Nevertheless, the theoretical B/R ratio in the PARSEC models show a similar trend at low metallicities, that is, a very high B/R ratio at young ages. However, using higher core overshooting for higher masses shortened the relative amount of time spent on the BHeB, lowering the B/R ratio for the youngest HeB stars, bringing them into closer agreement with our and M11's observations.

However, one consequence of lowering the core overshooting strength is that it makes the B/R ratio higher for the oldest HeB stars. There is no compelling evidence in our data or from M11 for an increase or decrease in the B/R ratio at ages $\gtrsim$150 Myr, due to the

increasing difficulty in distinguishing between the faint RHeB and BHeB as the sequences merge with the RC. A large sample of stellar clusters would be the best means to test core overshooting at ages $\gtrsim$ 250 Myr.

3.7 Conclusions

In this chapter, we have extended the galaxy sample of M11 and tested new models that increase the strength of convective overshooting with mass. These models better match the nearly vertical BHeB sequences seen in optical CMDs of nearby dwarf galaxies while remain consistent with the high B/R ratio observed younger ages. MDCOS is a long awaited improvement to HeB models, though there are still significant discrepancies in the locus of the RHeB sequence which are unchanged by the MDCOS prescription. The increase in B/R ratio for low stellar masses, introduced by MDCOS, needs to be verified. The contributions from less important physical parameters also need to be further explored.

The fact that the B/R ratios did not show obvious variations as a function of metallicity does not rule out that there is a metallicity dependence in HeB star models, as we see increasing offsets in data and MDCOS model matching with increasing metallicity. Increasing the complexity of the age magnitude relationship to force the fitting of the second CMD filter will help to further calibrate models and explore this possibility. Morefover, stellar evolution models calculated with a higher resolution in the Λ_c parameter space (i.e, $0.3 \lesssim \Lambda_c \lesssim 0.7$ will help constrain the functional form the Λ_c-mass dependence.

We have shown that this simple model of abruptly changing core overshooting in intermediate mass, low metallicity stars, drastically improves the model's ability to match the location of the BHeB on optical CMDs. It also alleviates the issue of over production of BHeB stars predicted at young ages. In other words, not only does the MDCOS prescription better match the observed HeB sequences, it also better matches the relative lifetimes on the RHeB and BHeB, especially for young HeB stars.

While this prescription has improved the BHeB fitting situation, the RHeB of the models are still problematic. The RHeB sequence is comprised of stars with large convective envelopes. However, the observed Hayashi line does not coincide with the theoretical one. The origin of this problem is unclear; it could be due to the mixing length parameter, which

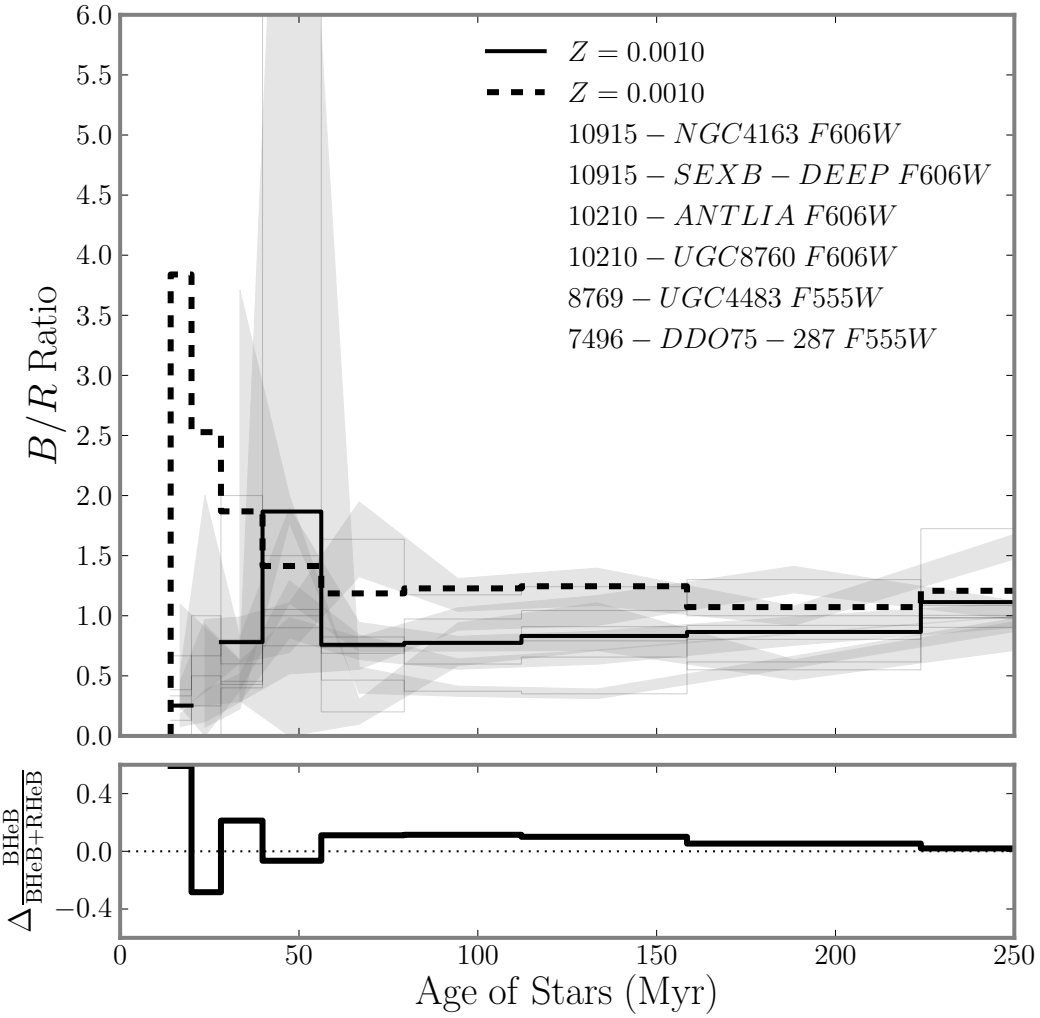

Figure 3.29 Same as Figure 3.21, but using MDCOS models.

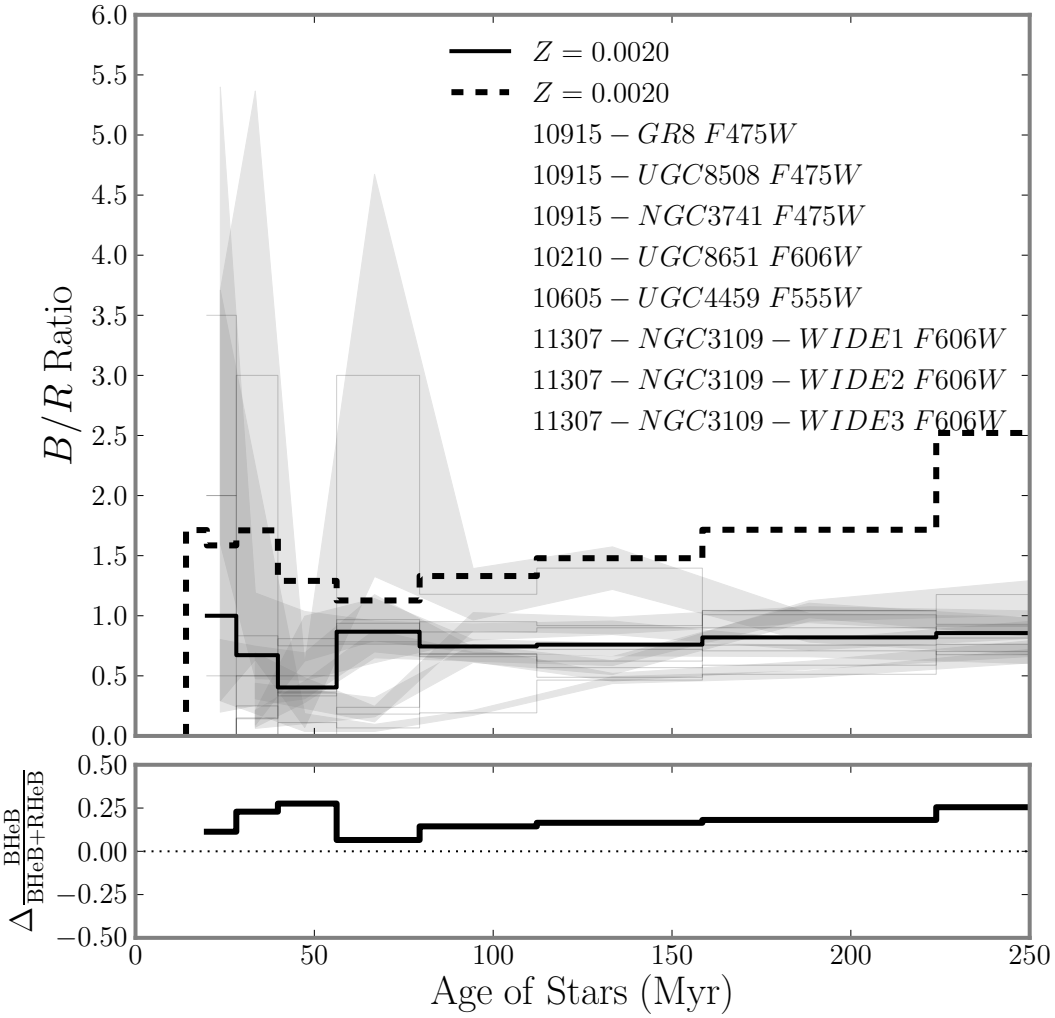

Figure 3.30 Same as Figure 3.29, but with galaxies with measured metallicity $Z = 0.002$.

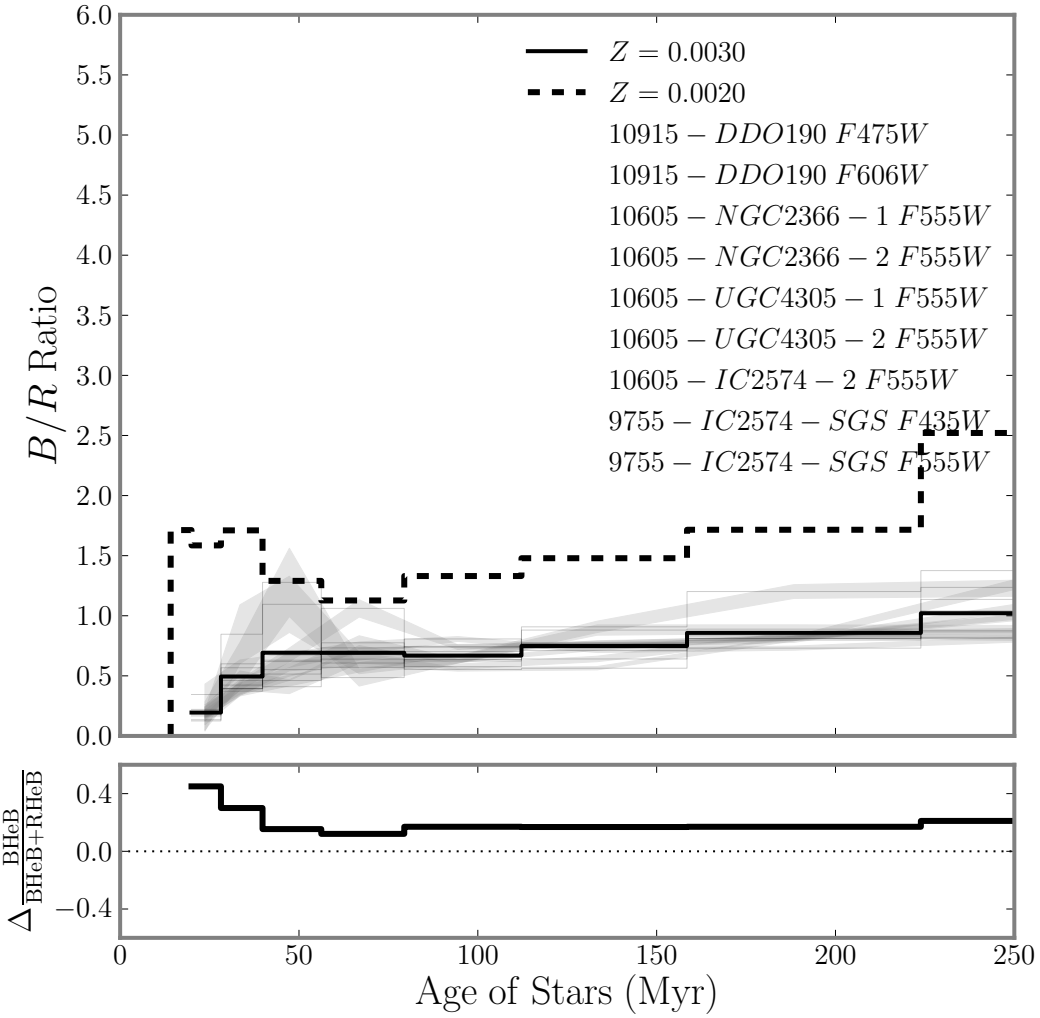

Figure 3.31 Same as Figure 3.29, but with galaxies with measured metallicity $Z = 0.003$.

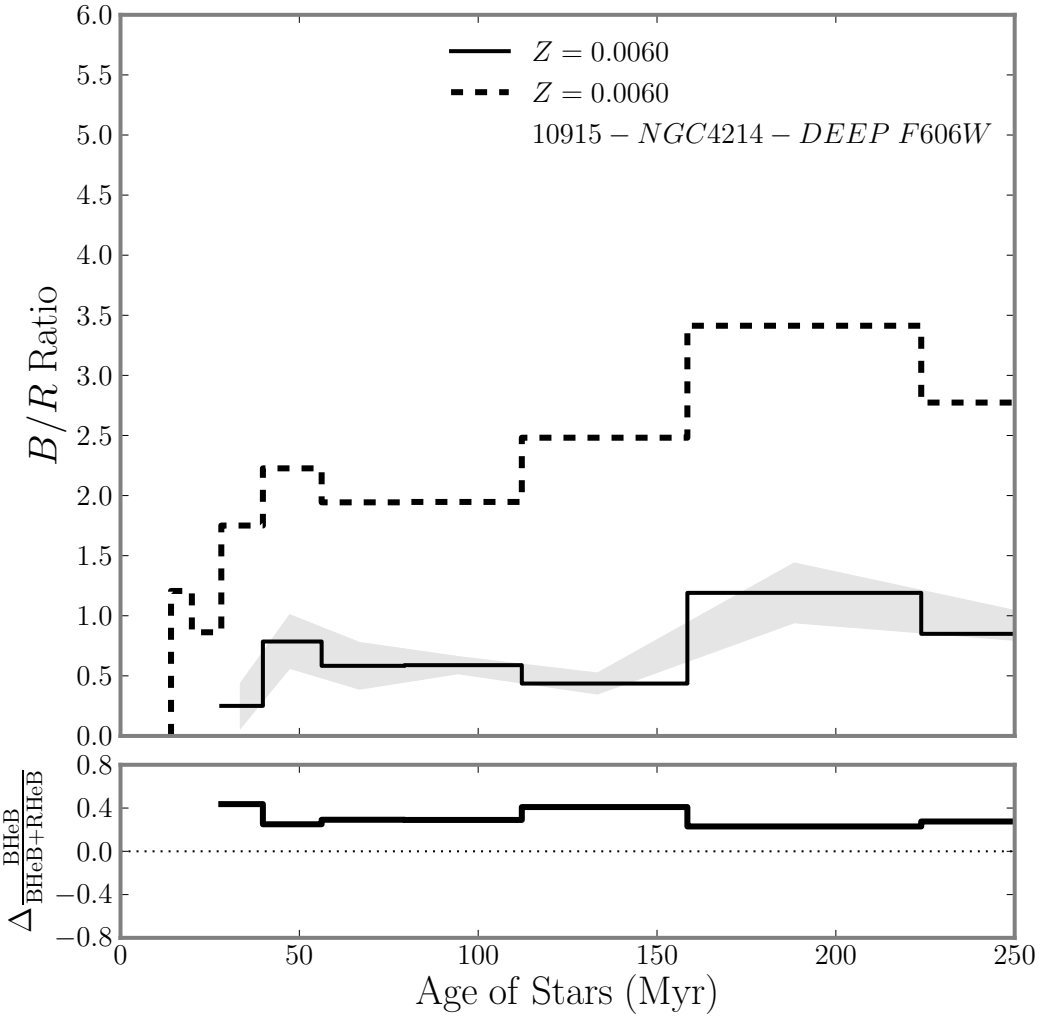

Figure 3.32 Same as Figure 3.29, but with galaxies with measured metallicity $Z = 0.006$.

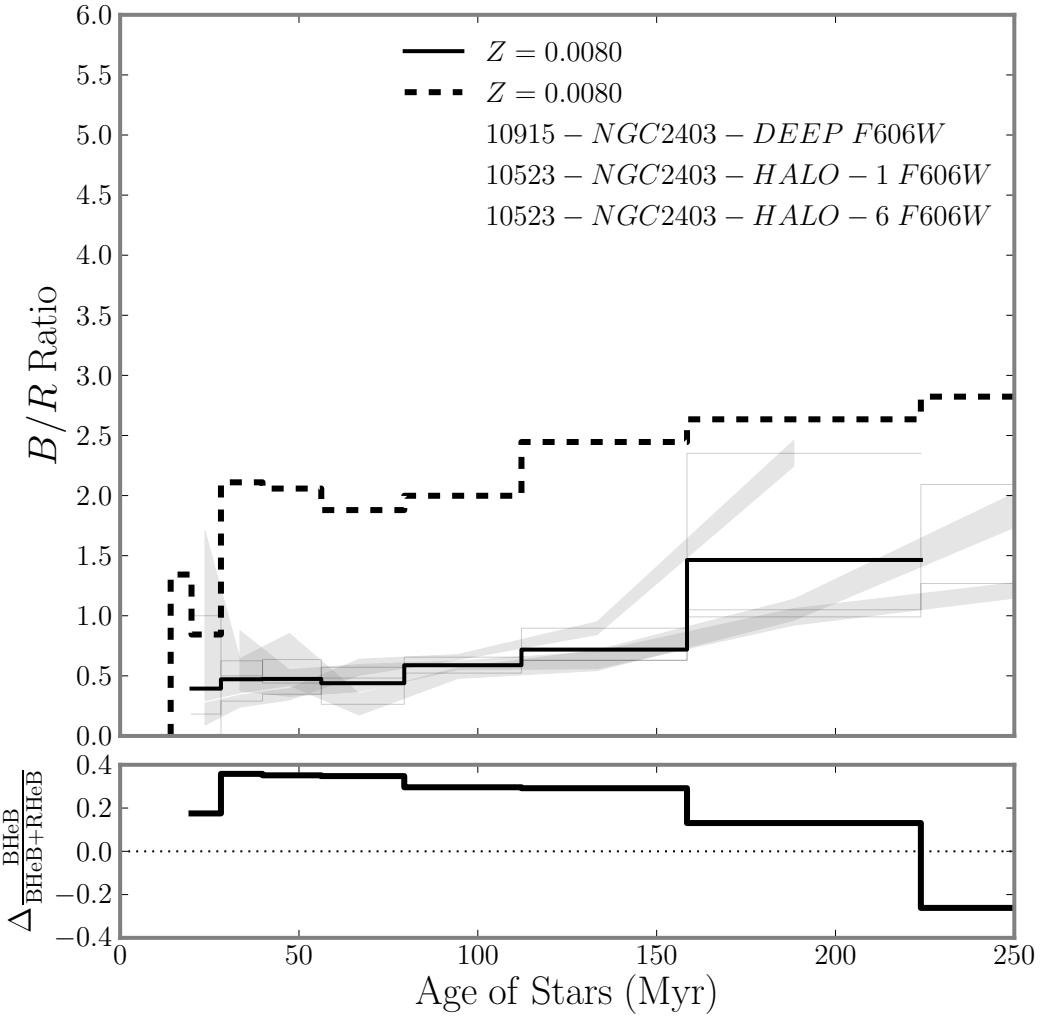

Figure 3.33 Same as Figure 3.29, but with galaxies with measured metallicity $Z = 0.008$.

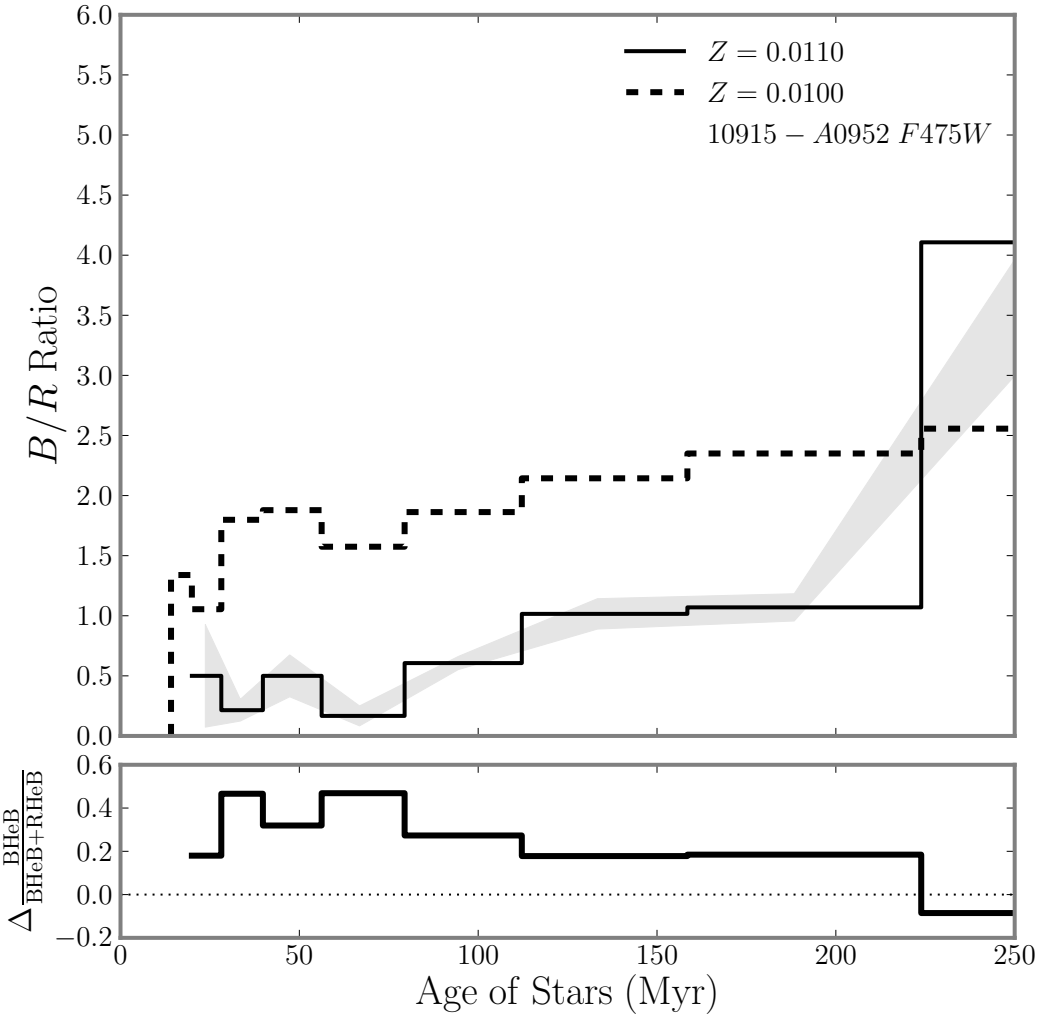

Figure 3.34 Same as Figure 3.29, but with galaxies with measured metallicity $Z = 0.011$.

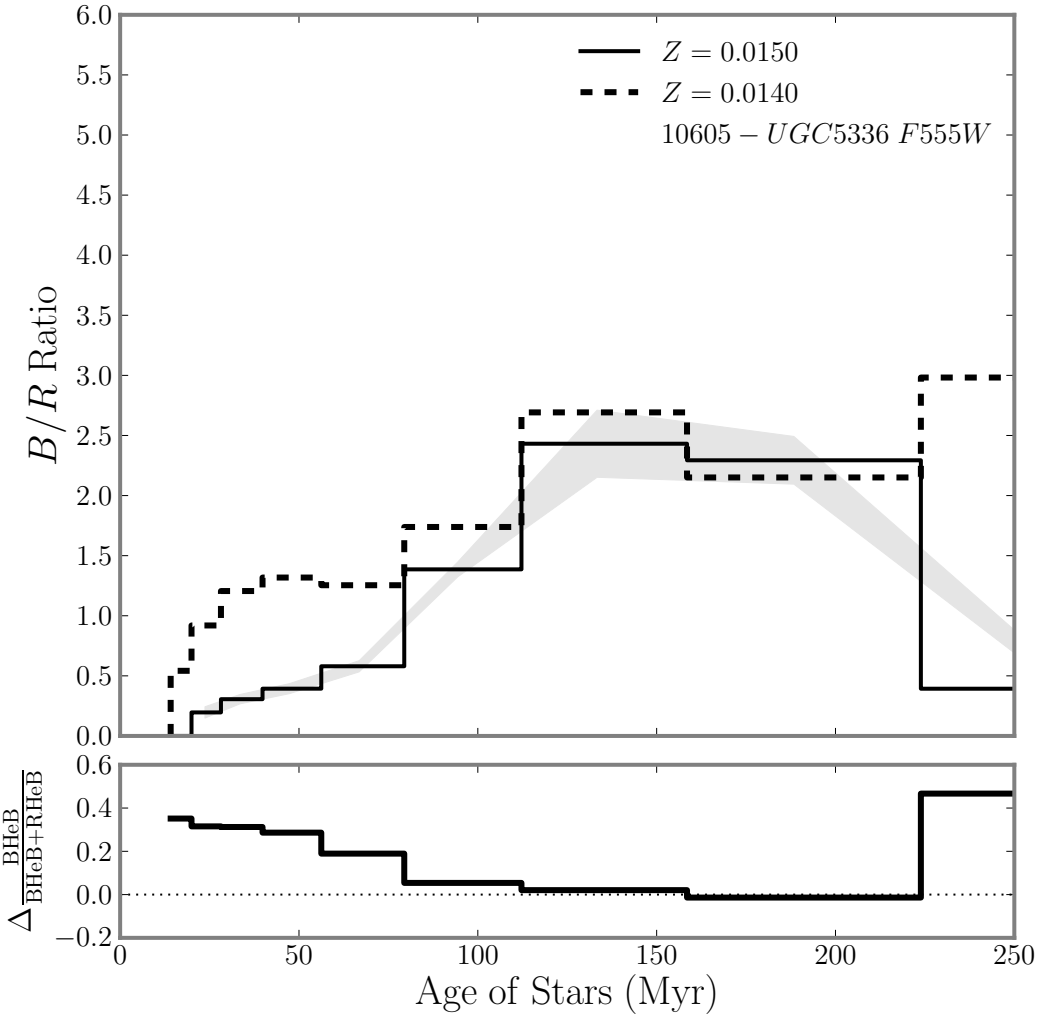

Figure 3.35 Same as Figure 3.29, but with galaxies with measured metallicity $Z = 0.015$.

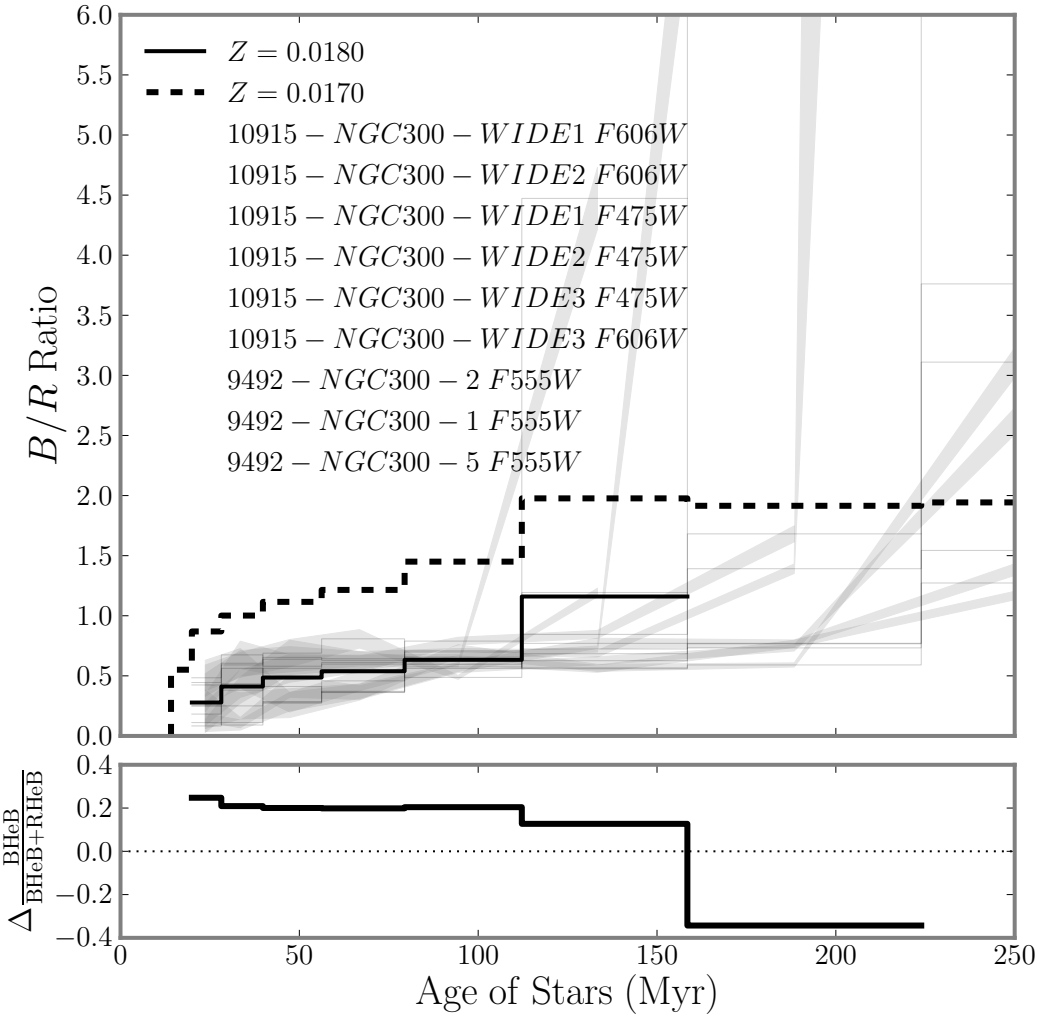

Figure 3.36 Same as Figure 3.29, but with galaxies with measured metallicity $Z = 0.018$

has been calibrated to the Sun and is perhaps improperly invoked for red giants, however this would have much larger implications on all evolutionary phases from the upper MS to the timing of the TP-AGB. On the other hand, it may have little to do with stellar interior models. Deeper investigations into the stellar atmospheric models and their synthetic colors are necessary to constrain the RHeB.

There are three other parameters that are of less importance to the HeB evolution but should be included to improve future models. In order of their importance: 1) the strength of overshooting at the base of the convective envelope which change when a RHeB star becomes a BHeB star as well as increase the temperature extent of the blue loop; 2) The temperature dependency of the $^{12}\mathrm{C}(\alpha,\gamma)^{16}\mathrm{O}$ reaction, which may be important in determining when a BHeB star will return to the Hayashi line. This reaction becomes more important the higher the mass of the HeB star; and 3) mass loss on the HeB, although mass loss does not have a large effect on stars with $M \lesssim 12 M_{\odot}$. Unfortunately, due to the IMF and short lifetimes, there are few massive HeB stars in dwarf galaxies to provide the statistical constraints necessary in calculating the B/R ratio. However, the Panchromatic Hubble Andromeda Treasury (Dalcanton et al., 2012, see Chapter 2[) is a promising source of high quality young stellar complexes.

Chapter 4

CONSTRAINING TP-AGB LIFETIMES WITH LOW-METALLICITY DWARF GALAXIES

4.1 Context

The final project of this thesis constrains mass loss prescriptions for a very uncertain phase of stellar evolution, the asymptotic giant brach (AGB). As in Chapter 3, we find observational constraints using nearby galaxy data of a large sample of low metallicity AGB stars.

4.2 Introduction

The thermally pulsating asymptotic giant branch (TP-AGB) is the most uncertain evolutionary phase of low and intermediate mass ($\sim 1-8M_{\odot}$) stars. These stars ascend the AGB during double shell fusion around a degenerate core. As they evolve, AGB stars undergo a series of He-flashes (called thermal pulses). During the thermal pulses, the base of the convective envelope may deepen inside the inter-shell region, dredging nuclear material up from the interior and expelling it into the interstellar medium through chemically enriched stellar winds (e.g., Herwig, 2005).

Although the TP-AGB's lifetimes are generally very short (less than a few Myr), their high luminosities contribute significantly to the integrated spectral energy distribution of galaxies (e.g., Maraston, 2005b; Conroy et al., 2009; Melbourne et al., 2012), particularly at redder wavelengths. Therefore, understanding the AGB phase of stellar evolution is critical for interpreting the integrated light of distant galaxies, as well as the chemical evolution of local galaxies.

There have been many successes in constraining aspects of TP-AGB star evolution with observations (e.g., see Kerschbaum et al., 2007, 2011, and refs. therein.). However, AGB lifetimes are still uncertain, especially in metallicity regimes found outside the Milky Way and Magellanic Clouds. The most popular method to constrain TP-AGB lifetimes is through

determining the relative number densities of evolutionary phases on a color-magnitude diagram (CMD). However, small numbers of observed TP-AGB stars can hamper the usefulness of the derived model constraints (e.g., Frogel et al., 1990; van Loon et al., 2005; Girardi & Marigo, 2007; Boyer et al., 2009), particularly in stellar clusters.

To increase the sample size of TP-AGB stars, several studies have carried out detailed analyses of individual clusters in the Large and Small Magellanic Clouds (LMC, SMC) and the Milky Way (MW) (e.g., Lebzelter & Wood, 2007; Kamath et al., 2010; van Loon et al., 2006; Boyer et al., 2010). Another method, described in Girardi & Marigo (2007), combined star counts from LMC and SMC clusters in age and metallicity bins to measure TP-AGB lifetimes with reduced uncertainties due to small number statistics. These studies have proven very useful for TP-AGB model calibrations in the specific ages and metallicities of the MW and MCs cluster populations.

In the intermediate-metallicity MCs (Z=0.004 and 0.008) Marigo et al. (2008) successfully calibrated TP-AGB lifetimes based on the observationally-derived C-star luminosity functions and C- and M-star lifetimes (using data from Groenewegen et al., 2002; Girardi & Marigo, 2007). However, these derived lifetimes seem to be overestimated when extrapolated to metallicities found in dwarf galaxies (Gullieuszik et al., 2008; Held et al., 2010; Melbourne et al., 2010). In other words, TP-AGB models calibrated only with MC observations do not describe AGB star populations at low metallicities. Therefore, we need model constraints at even lower metallicities than the MCs.

To extend to low metallicities, Girardi et al. (2010, hereafter, G10) further constrained the Marigo et al. (2008) TP-AGB models using optical observations of low-metallicity nearby, non-Local Group galaxies. These samples were from the ACS Nearby Galaxy Survey Treasury (ANGST; Dalcanton et al., 2009) and the Archival Nearby Galaxies: Reduce, Reuse, Recycle (ANGRRR; Gilbert et al., 2013) database. ANGST is a volume limited sample of ~ 70 non-Local Group galaxies to $\lesssim 4$ Mpc. Using a subset of 12 dwarf galaxies from the ANGST sample that showed little to no recent star formation, G10 compared LF for each galaxy with simulations, and updated the mass-loss prescriptions for low-mass, low-metallicity, TP-AGB stars before the onset of dust driven winds. This correction resulted in good data-model agreement. Moreover, the revised TP-AGB models reproduced

the measured lifetimes and initial-to-final mass relationship of the Galactic globular cluster M4.

The success of the G10 method, however, was limited by the optical filter-set available. The reddest filter in the ANGST survey is $F814W$, which requires higher bolometric corrections for cooler TP-AGB stars (Girardi et al., 2008a). This limitation allowed for a complete AGB sample only for TP-AGB stars with $T_{\rm eff} > 4000$K, corresponding to a mass range of $0.8 - 1.4 M_{\odot}$, leaving the lifetimes of higher mass stars unconstrained.

To generate a complete sample of TP-AGB stars up to $3 M_{\odot}$, near-infrared (NIR) filters are necessary. In this chapter, we build upon the analysis of G10 by calculating the luminosity functions (LFs) of modeled TP-AGB stars using the near-infrared $WFC3/HST$ "snapshot" follow-up survey to ANGST (Dalcanton et al., 2012, hereafter AGB-SNAP). This sample includes 26 NIR fields of 23 ANGST galaxies, with 10,000s of TP-AGB stars. This filter set allows us to probe TP-AGB masses from 1 to 5 $M_{\odot}$ with $T_{\rm eff} > 3000$K.

Specifically, this chapter focuses on the AGB SNAP galaxies with observationally measured metallicities near $Z = 0.002$, as well as galaxies from the G10 sample with AGB SNAP observations. By limiting this analysis to a narrow metallicity range and still including both young and old galaxies, we include a larger range in TP-AGB masses in the low metallicity analyses. The oldest galaxies will tell us the TP-AGB lifetimes at $\sim 1 M_{\odot}$ while the youngest will tell us the lifetimes at $\sim 2 - 3 M_{\odot}$.

Mass loss determines the rate of evolution on the AGB. So as an initial calibration, we find constraints on the lifetimes of AGB stars based on three mass loss prescriptions, discussed below.

The chapter is structured as follows. Section 4.3 provides a summary of the data sample, including its photometric reduction, metallicity measurements, and star formation histories. We describe the stellar evolution models and TP-AGB models with several mass loss prescriptions in Section 4.4. We summarize the procedure of producing population synthesis models of the galaxy sample in Section 4.5. In Section 4.6 we discuss the observational constraints on the models. We examine the adequacy of each mass loss prescription in Section 4.7 and conclude in Section 4.8.

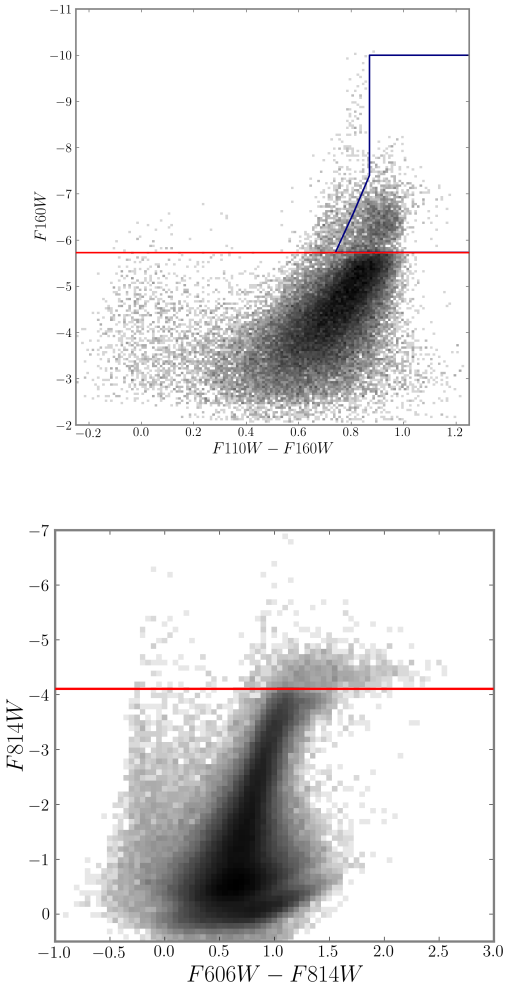

Figure 4.1 Composite Hess diagrams of the $Z \sim 0.002$ galaxy sample (see Table 4.1). Each galaxy was first converted to absolute magnitudes using A_V and $m-M_0$ derived in Dalcanton et al. (2012) (and refs. therein. Parameters are also listed in Table 4.1). To create a single region each galaxy was then shifted in $F160W$ or $F814W$ to match the average M_{TRGB} (thick horizontal line), and the color and magnitude offsets of the RGB and AGB regions were applied to each individual galaxy. The separation between RHeB stars and AGB stars were chosen by eye and then assessed for contamination from other stellar phases (blue polygon).

4.3 Data

4.3.1 Resolved Stellar Populations in Optical and NIR

We now briefly summarize the data reduction and photometry of the AGB-SNAP sample. For full details, we refer to the ANGST survey paper (Dalcanton et al., 2009) and the AGB-SNAP survey paper (Dalcanton et al., 2012).

Optical data from the STScI ACS pipeline data were photometered using DOLPHOT2.0 (Dolphin, 2002) including the ACS module. Cosmic rays were rejected after combining all images into a single drizzled image using the `multidrizzle` task within PyRAF (Koekemoer et al., 2003). We use the conservative ANGST photometric catalog (`*gst`), which only includes objects with DOLPHOT parameters `SNR < 4`, $((\texttt{sharp}_1 + \texttt{sharp}_2)^2 \leq 0.075)$, and crowding $((\texttt{crowd}_1 + \texttt{crowd}_2) \leq 0.1)$ in both filters. ANGST data obtained following the ACS camera failure as well as ANGRRR data followed the WFPC2 pipeline of Holtzman et al. (2006), which processes STScI baseline output through HSTphot, a WFPC2 optimized predecessor of DOLPHOT but updated to July 2008 CTE corrections (derived by A. Dolphin).

The NIR AGB-SNAP data were also reduced using the DOLPHOT package, however, with a significant update of the WFC3 module (among other enhancements). We again use the conservative photometry (`*gst`), in this case with DOLPHOT parameters `S/N < 4,` $((\texttt{sharp}_{F110W} + \texttt{sharp}_{F160W})^2 \leq 0.12)$ and $((\texttt{crowd}_{F110W} + \texttt{crowd}_{F160W}) \geq 0.48)$.

4.3.2 Star Formation Histories of the Galaxy Sample

Star formation histories were the same as those used in G10 which were derived using the CMD-fitting MATCH package (Dolphin, 2000) using the optical data (though over a slightly larger field, as the optical CMDs used here were trimmed to the WFC3/IR footprint, see Dalcanton et al., 2012). MATCH finds the most probable CMD that fits the optical CMD based on a given IMF, binary fraction, artificial star tests, and stellar isochrones. Specifically, G10 adopted a Salpeter (1955) IMF and a binary fraction of 0.35. The best-fit CMD is a product of the most probable star formation history as a function of metallicity.

The SFHs were then used as input to the stellar population synthesis program TRILE-

GAL (Girardi et al., 2005b, see Section 4.5). One major caveat needs to be addressed. The SFHs used as input for TRILEGAL in G10 were derived using isochrones from Girardi et al. (2000) with updates from Marigo et al. (2008). However, in this study, we adopt the same SFHs, but generate CMDs using new stellar evolution models in TRILEGAL (described in Section 4.4). Using different models than the ones used to derive the SFH could be problematic. To test the adequacy of using the same SFHs as G10, we compare the TRILEGAL simulations using the new models and the Girardi et al. (2000); Marigo et al. (2008) models.

These tests are fully discussed in Appendix A; briefly, there does not appear to be a significant problem with using any single SFH. The optical behavior of stellar isochrones is much better calibrated so we can assume that the optically-derived SFH as likely to be more accurate than one derived from the NIR CMD because the SFH would compensate for likely deficiencies in the NIR calibrations (largely through shifting to lower metallicities to match the bluer colors). However, almost all the differences in the model NIR CMD arise in color, rather than luminosity, suggesting that the calibration is more due to stellar atmospheres, which are known to be highly complex in the NIR. Fortunately, a complete census of the AGB depends far more on luminosity than color, and the examination of the LFs between models and data suggests that a luminosity-based comparison should be fine.

4.3.3 Mean Metallicities of the Galaxy Sample

We constrain the metallicities of the AGB stars in two ways. First, we use the current gas phase oxygen abundances taken from Berg et al. (2012, and refs. therein) when available. Assuming that the metallicity increases monotonically with time, these oxygen abundances are upper bounds on the metallicity of the intermediate age TP-AGB stars. Second, in the absence of spectroscopic data, we use the SFH-weighted average value from the best-fitting MATCH solution. The metallicities from MATCH are constrained primarily from the shape and color of the RGB, which contains stars with a wide range of ages. MATCH metallicities are therefore most likely to be more characteristic of the typical ages of the AGB stars. Even if both the oxygen gas phase abundance and the MATCH-based abundances are not exact matches to the metallicities of the AGB stars, low metallicity galaxies naturally have

a limited range in metallically, guaranteeing that any estimate will be close to the actual metallicity of the intermediate age stars.

From either the Oxygen abundance or the MATCH estimate [Fe/H], we estimated the metallicity of each galaxy,

$$Z_{\rm galaxy} = Z_{\odot} * 10^{[{\rm Fe/H}]_{\rm galaxy}} \tag{4.1}$$

where

$$[{\rm Fe/H}]_{\rm galaxy} \approx [{\rm Fe/O}] + [{\rm O/H}]. \tag{4.2}$$

Assuming solar abundance patterns (e.g., Anders & Grevesse, 1989), [Fe/O] is negligible, so

$$[{\rm Fe/H}]_{\rm galaxy} \approx \log({\rm O/H}) - \log({\rm O/H})_{\odot}, \tag{4.3}$$

using the value of Solar oxygen abundance, $\log({\rm O/H})_{\odot} = 8.76$ from Caffau et al. (2008), and $Z_{\odot} = 0.015$ for the value of Solar metallicity.

We limit the initial galaxy sample to galaxies with metallicities, $Z \sim 0.0020 \pm 0.0001$, which restricts our sample to nine fields of eight galaxies. Five of them have measured gas metallicities (DDO82, IC2574-SGS, UGC-4305, NGC4163, and UGC-8508), and the remainder are derived from MATCH. Three of the galaxies were also analyzed in G10, (SCL-DE1, DDO78, and DDO71). The basic properties of the low metallicity galaxies analyzed in this chapter are listed in Table 4.1.

4.3.4 Selecting AGB and RGB Stars

To prepare a complete sample of AGB stars, we first minimize contamination from RGB and RHeB stars. Selecting the AGB stars is done using the NIR filters, where the bolometric corrections vary little with $T_{\rm eff}$ (c.f. Girardi et al., 2008a). It is therefore safe to assume that no stars above the TRGB are RGB stars. Separating the RHeB stars however, is done by comparing simulations to data. In Figure 4.1, all six $Z \sim 0.002$ galaxies are plotted as a Hess diagram in M_{F160W} and aligned to their average $M_{TRGB} = -5.73$. The division between the RHeB and AGB is apparent, with the AGB region defined to be redder than $(M_{F110W} - M_{F160W},\ M_{F160W})$: $(0.74, -5.73), (0.81, -6.6), (0.87, -7.4)$. Fitting a double

gaussian shows a maximum of 3% RHeB contamination of the AGB region and 3% AGB contamination of the RHeB region.

RGB stars are used to aid in creating realistic population synthesis models (discussed in more detail in Section 4.5). We scale the mass of the simulated galaxy to match the number of RGB stars found in the data. Because of the known issues with the overall NIR calibration (see Appendix A), we select RGB stars from the optical data where the models are better calibrated and the RHeB is well separated on the CMD. For galaxies that show little to no recent star formation (UGC-8508, NGC-4163, DDO82, SCL-DE1, DDO71, and DDO78), we count all stars that are 1.5 magnitudes below the TRGB (c.f., G10) since no color-cut is needed in the absence of MS or RHeB stars. For the remainder of the galaxy sample, we select RGB stars in the same magnitude range, and make color cuts to separate the MS and RHeB, first by eye, and then refined by the double gaussian technique discussed above.

Target	Optical Filters	A_V	Mean NIR Color	$m_{\rm F160W}$ TRGB	$m_{\rm F160W}$ 50% complete	$(m-M)_0$	$\log[O/H]$	$N_{\rm RGB}$	$N_{\rm AGB}$	$\frac{N_{\rm AGB}}{N_{\rm RGB}}$
1	2	3	4	5	6	7	8	9	10	11
DDO82	F606W, F814W	0.133	0.909	22.062±0.028	24.69	27.900	7.950±0.200	23796	1235	0.052
IC2574-SGS	F555W, F814W	0.112	0.859	22.209±0.019	24.68	27.900	7.930±0.050	15823	1501	0.095
UGC4305-1	F555W, F814W	0.098	0.850	21.917±0.071	24.76	27.650	7.920±0.100	6242	662	0.106
UGC4305-2	F555W, F814W	0.098	0.835	21.927±0.025	24.79	27.650	7.920±0.100	7814	652	0.083
NGC4163	F606W, F814W	0.062	0.875	21.558±0.014	24.71	27.290	7.910±0.200	10747	631	0.059
UGC8508	F475W, F814W	0.047	0.847	21.402±0.024	24.83	27.060	7.890±0.200	3047	251	0.082
DDO78	F475W, F814W	0.066	0.901	22.031±0.027	25.04	27.820	7.88	6542	284	0.043
DDO71	F606W, F814W	0.303	0.853	22.080±0.064	25.03	27.740	8.04	3665	183	0.050
SCL-DE1	F606W, F814W	0.046	0.793	22.560±0.037	25.09	28.110	7.69	1554	59	0.038

Table 4.1 Columns 3–7 from Dalcanton et al. (2012), column 8 from Berg et al. (2012); Marble et al. (2010, and refs. therein). $\log[O/H]$ for DDO78, DDO71, and SCL-DE1 were taken from the SFH weighted average calculated by MATCH.

4.4 Models

Mass loss dominates an AGB star's evolution and fate, though its physical mechanism is still uncertain. It is clear from observations of Mira and OH/IR stars that mass loss rates on the AGB increase with time until they reach $\sim 10^{-4} M_{\odot}$/yr (e.g., review by Willson, 2000).

For a star to have a wind, there must be either an outward force that provides momentum input, lifting the stars surface layers, or some energy source that provides sufficient heat input, such as magneto-acoustic waves generated above the photosphere (e.g., Lamers & Cassinelli, 1999).

We can divide mass loss into three regimes, before the dust-driven winds, during dust-driven winds, and the super wind phase.

Before the onset of dust driven winds, we take two choices of mass loss rates, the traditional Reimers (1975) mass loss, which was based on the properties of a few red supergiants, and Schröder & Cuntz (2005) which physically motivates Reimers' law, using mechanical energy as the input heat to cause the wind (plausibly from Alfvén waves in the turbulent chromosphere). In effect, Schröder & Cuntz (2005)'s prescription adds $T_{\rm eff}$ and log g dependencies to Reimers' law.

During the dust-driven phase, winds are caused by the momentum input from radiation absorbed by dust in the diffuse atmospheres of AGB stars. This wind is enhanced by pulsations. As the AGB star pulsates, the surface is levitated to a cooler region around the star, which causes more dust as well as molecules to form, allowing for more material to absorb the momentum from the radiation. This is a very uncertain phase and the prescriptions we adopt are briefly described below.

Finally, the super wind phase occurs when the maximum amount of radiation energy is transferred to the wind, we use the equations found in Vassiliadis & Wood (1993), in which the mass loss is proportional to the stellar luminosity and escape velocity of the gas far from the central star, which itself is proportional to the pulsation period.

4.4.1 Stellar Evolutionary Codes: PARSEC and COLIBRI

The **Pa**dova and T**r**ieste **S**tellar **E**volution **C**ode (PARSEC; Bressan et al., 2012) is a thoroughly revised version of the popular Padova stellar evolution code used to compute stellar evolution tracks. We use its v1.1 release (Bressan et al., 2013, see also http://stev.oapd.inaf.it), which offers new stellar tracks spanning the ranges $0.0001 \leq Z \leq 0.06$, $0.1M_{\odot} \leq M \leq 12M_{\odot}$, and from the Pre-MS phase to either the TP-AGB or core Carbon ignition phase.

Following the first thermal pulse on the AGB, COLIBRI (Marigo, 2013) takes over the stellar evolution calculations from PARSEC. COLIBRI is an "almost-full" TP-AGB modeling code, that is, it relaxes many of the analytic forms of other synthetic TP-AGB models. Full details are found in (Marigo, 2013), the most relevant to this study include: 1) a spherically symmetric deep envelope model from the bottom of the quiescent H-burning shell up to the atmosphere, 2) molecular chemistry and Rosseland mean opacities calculated on-the-fly and consistent with surface abundances, 3) compete nuclear network to follow the nucleosynthesis occurring during fusion occurring at the base of the convective envelope (hot-bottom burning; HBB) in more massive AGB stars ($M > 4M_{\odot}$) and in the pulse-driven convective zone at thermal pulses, and 4) efficiencies of the third dredge-up[1] and HBB treated as free parameters to be calibrated by observations. In this chapter, we test two mass-loss prescriptions along with the mass-loss prescription adopted in G10.

4.4.2 COLIBRI Mass Loss Prescriptions

For the purposes of constraining the lifetimes of TP-AGB stars, we have calculated three sets of TP-AGB models using the COLIBRI code and different mass loss prescriptions. A sample comparison of these mass loss prescriptions are shown in Figure 4.2, and they are summarized in Table 4.2.

$\dot{M}_{G10}$ The mass loss prescriptions presented G10. Briefly, two main mechanisms are responsible for driving mass loss before and after the dust-driven winds take over, magneto-acoustic waves originating from below the stellar chromosphere (a semi-empirical re-

[1]The efficiency of third dredge-up as a function of the stellar mass and metallicity is described by the relations of (Karakas et al., 2002)

lationship from Schröder & Cuntz, 2005), and winds caused from radial pulsation and radiation pressure on dust grains (introduced by Bedijn, 1988).

$\dot{M}_{BS95}$ An extremely efficient mass loss rate from Blöcker & Schönberner (1995), in which a Reimers-like mass loss increases with increasing luminosity, due to pulsations. We adopt the efficiency of Reimers (1975) mass loss set to $\eta = 0.4$.

$\dot{M}_{VW93}$ The mean empirical mass loss rate of Vassiliadis & Wood (1993). Briefly, $\dot{M}_{VW93}$ increases exponentially with the period of pulsation, until the period is 500 days which marks the onset of the super wind phase.

Label	Pre-Dust Wind	Dust-Driven Wind	Super-Wind
$\dot{M}_{G10}$	Schröder & Cuntz (2005)	G10	Vassiliadis & Wood (1993)
	with $\eta = 4.0$	(a Bedijn (1988)-like formula)	(eqs. 1 and 3)
	Reimers (1975)	Blöcker & Schönberner (1995)	Vassiliadis & Wood (1993)
$\dot{M}_{BS95}$	with $\eta = 0.4$	with $\eta = 0.4$	(eqs. 1 and 3)
		(activated if $P > 100$ days)	
$\dot{M}_{VW93}$	Reimers (1975)	Vassiliadis & Wood (1993)	Vassiliadis & Wood (1993)
	with $\eta = 0.4$	(eqs. 2 and 4)	(eqs. 1 and 3)

Table 4.2 Mass loss prescriptions used in this chapter η refers to Reimers (1975)'s efficiency parameter. For every computational step, the mass loss rate is $\dot{M} \equiv \max[\dot{M}_{pre-dust}, \min(\dot{M}_{dust}, \dot{M}_{SW})]$ (see Marigo, 2013).

4.5 Modeling the Data

4.5.1 Population Synthesis with TRILEGAL

To model the photometry of resolved stellar populations we use the TRILEGAL population synthesis code (Girardi et al., 2005b) as in G10. TRILEGAL takes as input the PARSEC and COLIBRI stellar evolution libraries, a specified initial mass function (IMF), binary fraction, and the metallicity and star formation rate as a function of time. Importantly, TRILEGAL also simulates the L–$T_{\rm eff}$ variations due to the thermal pulse cycles on the TP-AGB (Girardi & Marigo, 2007).

The TRILEGAL input parameters are set to remain consistent with the parameters used SFH recovery (see Section 4.3.2). The stars produced by TRILEGAL are converted into absolute magnitudes in *HST* filters used in ANGST-SNAP using the set of bolometric corrections and extinction coefficients described in Girardi et al. (2008a), which are mostly based on ATLAS9 (Castelli & Kurucz, 2003) synthetic spectra, completed with Fluks et al. (1994) for the M giants. For C-type stars, we adopt the Aringer et al. (2009) library of C star models, interpolating inside the grids as a function of $T_{\rm eff}$, $\log g$, [Fe/H] and C/O ratio. Radiation reprocessing by circumstellar dust shells in mass-losing stars are taken into account as in Marigo et al. (2008), using the results of Groenewegen (2006)'s radiation transfer models for mixtures of 60% AlOx and 40% silicate, and of 85% amorphous Carbon and 15% silicon carbide (for M and C stars, respectively). Finally, the synthetic CMDs are corrected for distance and extinction, A_V – using extinction coefficients from Girardi et al. (2008a) – as listed in Table 4.1.

Each simulated stellar catalog is then degraded to statistically match the photometric uncertainties of the data. This is done by randomly assigning the appropriate magnitude offsets between input magnitude and recovered magnitude from artificial star tests (described in e.g., Dalcanton et al., 2009) to the simulated catalog.

Finally, we scale the simulation such that there is the same number of RGB stars (within 1σ) in the data and the simulated CMD. We adopt the number of RGB stars found in the optical data and randomly draw from a very large simulation to match that number of NIR RGB stars, iterating until the number of RGB in the simulation stars agree within 1σ

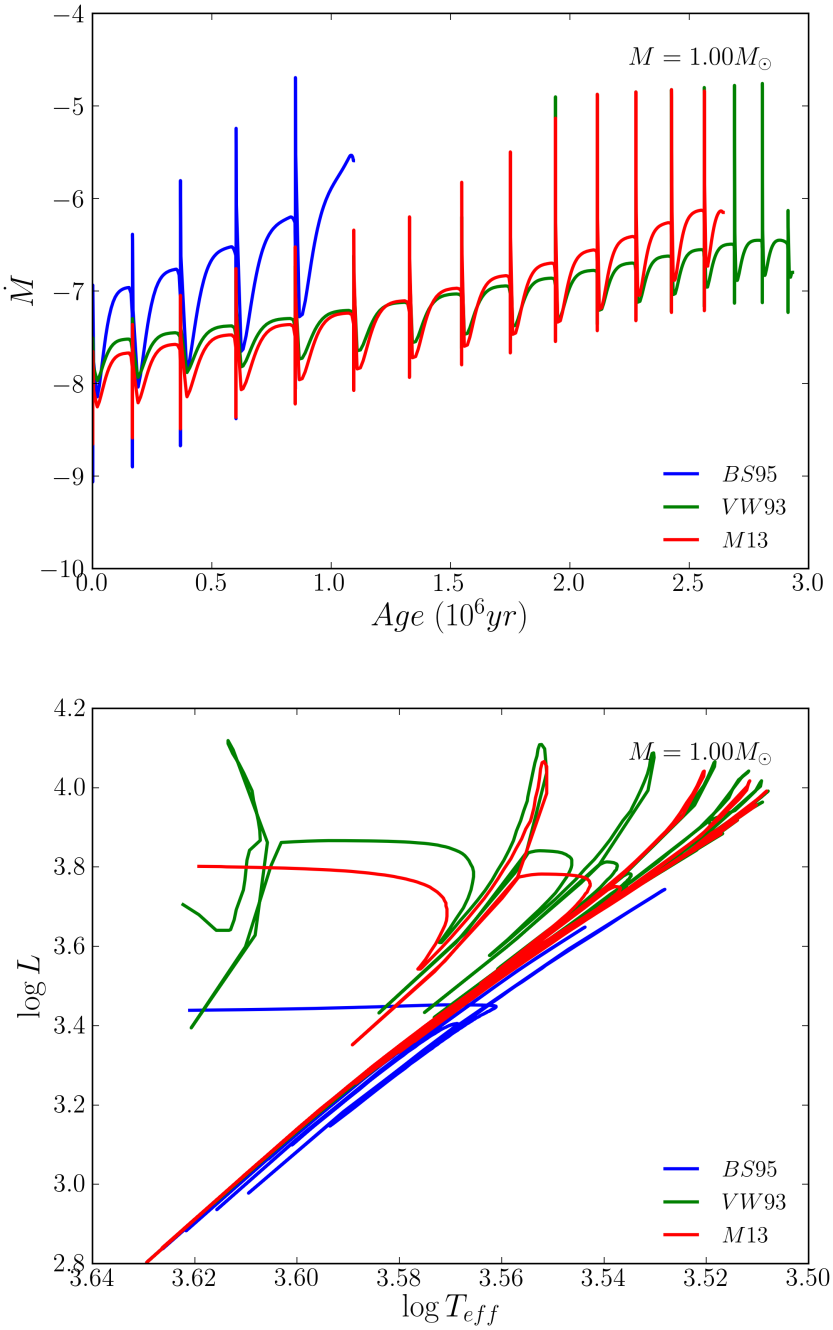

Figure 4.2 Sample evolutionary tracks calculated with COLIBRI for TP-AGB stars under three mass loss prescriptions. Each track has $Z = 0.002, Y = 0.252$. Top: Mass loss rate over time, the increase of $\dot{M}$ with luminosity in BS95 (blue) is evident, as well as the higher efficiency of mass loss, where the TPAGB is reached just after 1 Myr. VW93 (green) has the longest lifetimes of the three. G10 begins with lower mass loss rates than VW93 but steadily increases. Bottom: Example HR diagrams, the three prescriptions follow very similar tracks, however, G10 and VW93 are intrinsically brighter than BS93, and continue to pulsate while becoming PNe.

random error to the number of RGB stars in the optical data.

4.6 Observational Constraints on Models

Luminosity functions are a classic stellar evolution calibrator. Accurately reproducing the LF requires accurately populating the relative lifetimes and luminosities of a given population. As explained in Section 4.3, our simulated LFs are normalized to reproduce the number of stars on the RGB in the data. We also choose the magnitude bin sizes dynamically, in that we start with a minimum size (0.1 mag) but combine adjacent bins until there are at least 10 stars in each bin.

For example, Figure 4.3 shows the NIR data of the galaxies in three panels each. The left panels are CMDs of the data, the middle panels are the scaled-TRILEGAL simulations, and the right panels are the LF of both the data and scaled model. A horizontal line marks the TRGB (see Table 4.1). The numbers on the left of the middle and left panel reflect the number of RGB and AGB stars in the field. This same layout continues in all the following CMD and LF figures.

To assess the LF quantitatively, we measure the number ratio of AGB stars to RGB stars. We define $N_{\rm AGB}$ and $N_{\rm RGB}$ to be number of stars in their respectively defined regions (see Section 4.3.4). The N_{AGB}/N_{RGB} ratio is a modified application of the fuel consumption theorem (Renzini & Buzzoni, 1986a, FCT), which basically states that the number of stars on the AGB is related to the amount of fuel consumed in that phase, and thus proportional to the amount of time a star spends on the AGB (c.f., Girardi & Marigo, 2007).

The LF is a more sensitive constraint on AGB lifetimes than the N_{AGB}/N_{RGB}. As Melbourne et al. (2012) have shown, only a few bright AGB stars are needed to significantly change the integrated NIR flux. This difference would not be captured in the N_{AGB}/N_{RGB}, so even if excellent agreements are found between data and models with this ratio, the model is not complete if it does not reproduce the data as a function of magnitude.

4.7 Analysis

Target	$\frac{N_{\rm AGB}}{N_{\rm RGB}}$ Data	$\frac{N_{\rm AGB}}{N_{\rm RGB}}$ BS95	Frac. Difference	$\frac{N_{\rm AGB}}{N_{\rm RGB}}$ VW93	Frac. Difference	$\frac{N_{\rm AGB}}{N_{\rm RGB}}$ G10	Frac. Difference
DDO71	0.038 ± 0.004	0.031 ± 0.004	0.19 ± 0.05	0.095 ± 0.007	1.46 ± 0.26	0.088 ± 0.007	1.29 ± 0.24
DDO78	0.042 ± 0.003	0.078 ± 0.005	0.85 ± 0.12	0.169 ± 0.008	2.98 ± 0.35	0.150 ± 0.007	2.55 ± 0.30
SCL-DE1	0.057 ± 0.008	0.056 ± 0.008	0.02 ± 0.01	0.136 ± 0.014	1.36 ± 0.33	0.128 ± 0.014	1.23 ± 0.31
Results from NIR data							
DDO71	0.064 ± 0.006	0.152 ± 0.012	1.36 ± 0.23	0.303 ± 0.019	3.71 ± 0.58	0.297 ± 0.019	3.62 ± 0.57
DDO78	0.052 ± 0.004	0.182 ± 0.011	2.47 ± 0.34	0.376 ± 0.017	6.17 ± 0.75	0.338 ± 0.016	5.44 ± 0.68
SCL-DE1	0.064 ± 0.009	0.146 ± 0.020	1.30 ± 0.36	0.300 ± 0.032	3.72 ± 0.92	0.273 ± 0.029	3.29 ± 0.81
DDO82 BS95	0.091 ± 0.003	0.133 ± 0.005	0.46 ± 0.03	0.363 ± 0.010	2.97 ± 0.18	0.334 ± 0.010	2.66 ± 0.17
IC2574-SGS	0.169 ± 0.006	0.233 ± 0.007	0.38 ± 0.03	0.402 ± 0.010	1.38 ± 0.08	0.376 ± 0.010	1.23 ± 0.08
UGC-4305-1	0.181 ± 0.010	0.138 ± 0.006	0.24 ± 0.02	0.222 ± 0.009	0.23 ± 0.02	0.221 ± 0.009	0.22 ± 0.02
UGC-4305-2	0.148 ± 0.008	0.106 ± 0.005	0.29 ± 0.03	0.217 ± 0.008	0.46 ± 0.04	0.210 ± 0.008	0.42 ± 0.04
NGC4163	0.132 ± 0.006	0.178 ± 0.009	0.35 ± 0.03	0.344 ± 0.013	1.61 ± 0.13	0.323 ± 0.013	1.46 ± 0.12
UGC8508	0.187 ± 0.014	0.152 ± 0.011	0.18 ± 0.03	0.296 ± 0.017	0.58 ± 0.08	0.275 ± 0.016	0.47 ± 0.06

Table 4.3 The AGB to RGB ratio using several mass loss prescriptions with random uncertainties. From the table we find wide spread over production of all TP-AGB stars, with the least being from the BS95 mass loss prescription and the largest being from VW93.

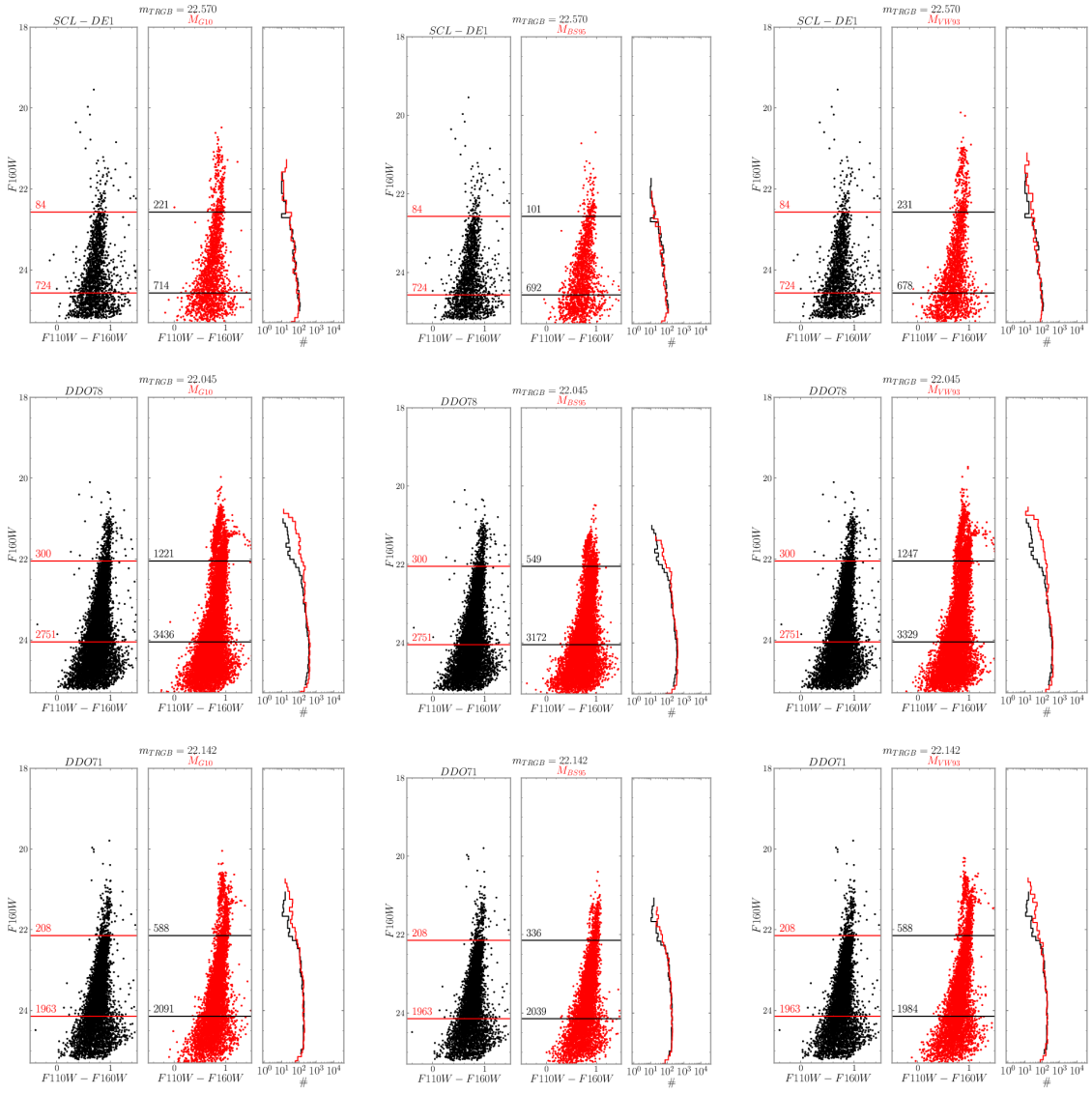

Figure 4.3 CMDs and LFs calculated with each mass loss prescription compared to data for all the galaxies in the sample. Left and middle panels with each frame are $F110W-F160W$ CMDs of data (left) and model (middle), with numbers of RGB and AGB stars indicated. Horizontal lines mark the TRGB (see Table 4.1) and 1.5 mag below. Right panels show LFs of the models and data. The left side of the figure grid is calculated with $\dot{M}_{G10}$; middle with $\dot{M}_{BS95}$; and right with $\dot{M}_{VW93}$. From top to bottom are SCL-DE1, DDO78, and DDO71.

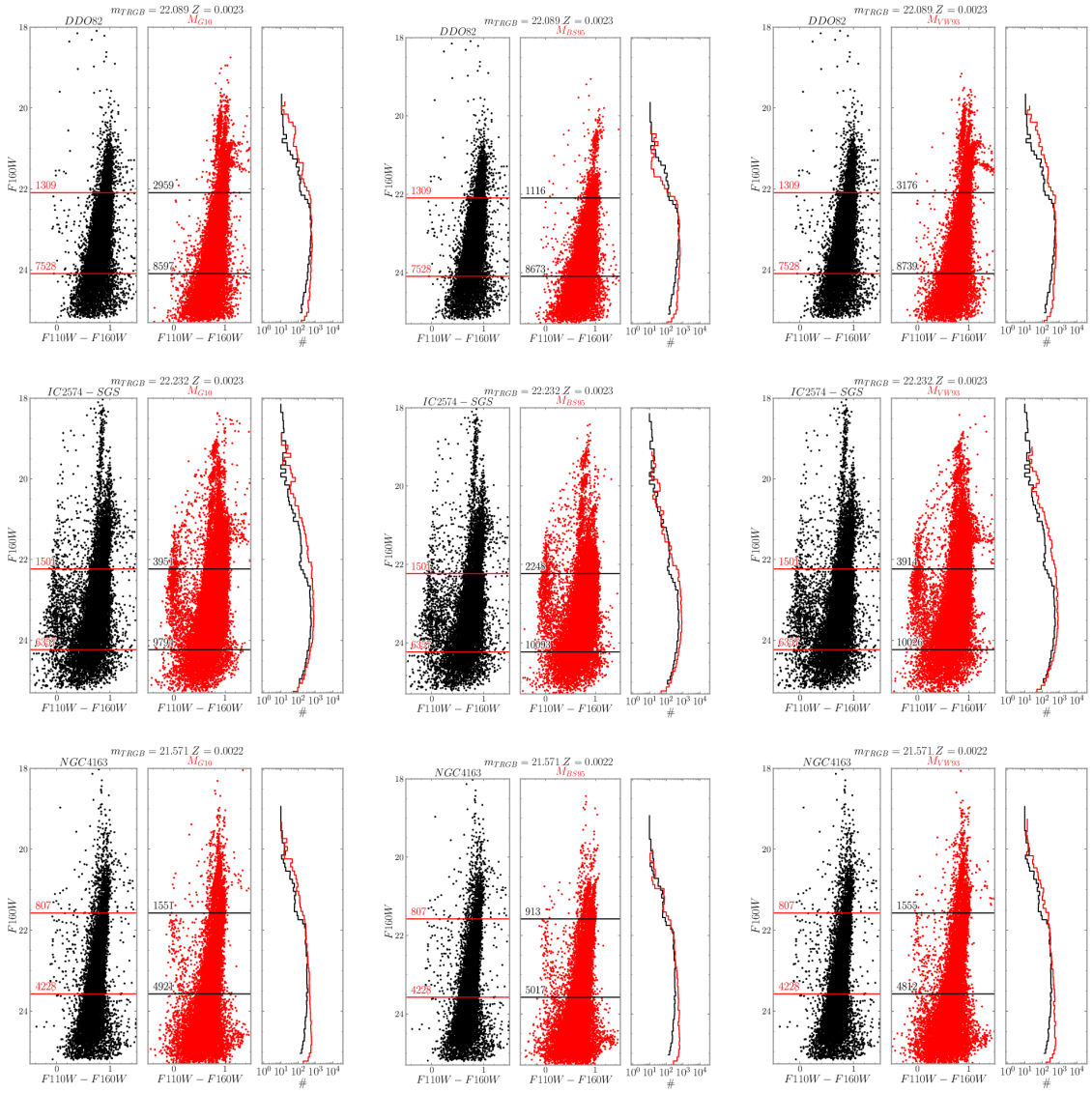

Figure 4.4 Same as Figure 4.3 but with galaxies DDO82, IC2574, and NGC4163 (from top to bottom).

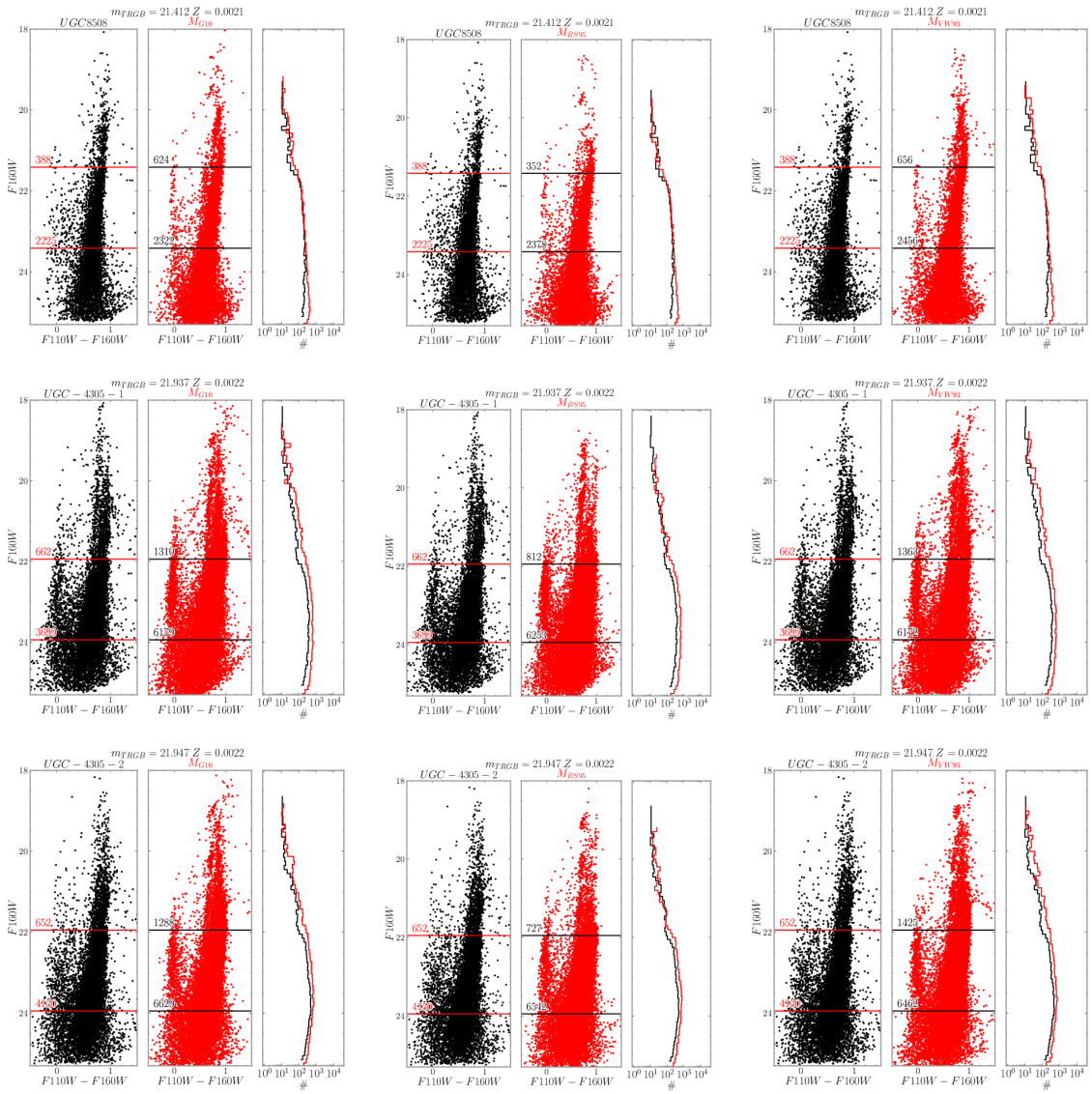

Figure 4.5 Same as Figure 4.3 but with galaxies UGC8508 and two fields of UGC4305 (from top to bottom).

4.7.1 Comparing the Mass Loss Prescriptions

The three mass loss prescriptions produce quantitatively different TP-AGB LFs in the simulated galaxies. Therefore, we can constrain which mass loss prescription is closest to describing the TPAGB stars in our galaxy sample by comparing how well the predicted LFs match the data.

The results of the TRILEGAL and COLIBRI simulations are shown in Figure 4.3, as a series of three-panel figures. In each figure, the left panel (black points) is t he CMD of the data; the middle panel (red points) is the simulated CMD, and the right panel shows luminosity functions of the data (black) and model (red). Horizontal lines mark the TRGB and 1.5 mag below (used to scale the number of model stars, see Section 4.3.4). The left column of figures show simulated CMDs calculated with TP-AGB mass loss following $\dot{M}_{G10}$; the middle column with $\dot{M}_{BS95}$, and the right column with, $\dot{M}_{VW93}$. Galaxies that show little to no evidence of forming stars in the last $\sim$ 1Gyr are considered ancient (DDO71, DDO78, DDO82, and SCL-DE1) and are separated from those with very recent SF (UGC-4305, IC-2574, UGC-8508, and NGC4163; see Weisz et al., 2011). The LF shown excludes bluer stars inconsistent with being RGB or AGB. The equivalent numbers of AGB to RGB stars are annotated on the figures and their ratios are listed in Table 4.3 (see Section 4.3.4).

To compare the mass loss prescriptions, Figures 4.6-4.8 compare the luminosity functions shown in Figure 4.3. They are color-coded by evidence of recent SF. Galaxies with evidence of recent SF are colored blue and the remainder are colored red. The top panels reproduce the right-most panels of Figure 4.3 after converting to absolute magnitudes. The middle panels show the fractional difference between the number of stars in the model (N_{model}) and the data (N_{data}), relative to the data. The closer the fractional difference is to zero, the closer the models are to reproducing the observed AGB magnitude distribution, suggesting more accurate lifetimes. The bottom panels show the residual differences between the model and data. We note that DDO82 is a strong outlier in these plots, which we discuss below (Section 4.7.2).

Mass Loss in the G10 Model

G10 introduced a prescription for the rate of mass loss before the onset of dust-driven winds ($\dot{M}_{\rm pre-dust}$) as a response to the over production of TP-AGB stars in the Padova stellar evolution library (e.g., Gullieuszik et al., 2008; Held et al., 2010; Melbourne et al., 2010). The LFs agree very well in the optical (see Appendix A) and in the NIR for a few of the galaxies (SCL-DE1, UGC 8508, and UGC 4305). However, this model over-produces TP-AGB stars for the rest of the NIR galaxy sample. On the whole, the model creates too many TP-AGB stars compared to those observed for all galaxies, as seen with the N_{AGB}/N_{RGB} ratio (see Table 4.3.

Although it is not good overall, the $\dot{M}_{G10}$ prescription is a better match to the LF when galaxies have more recent star formation (see Figure 4.6). The ancient galaxies show large differences in the number of TP-AGB stars in the simulated CMD and data, especially just fainer than $M_{F160W} = -7$ which corresponds to an initial mass $\lesssim 2M_{\odot}$.

Mass Loss in the VW93 Model

In almost every case, $\dot{M}_{VW93}$ over-predicts the number of AGB stars, and by extension, the lifetimes of the AGB stars. The Vassiliadis & Wood (1993) semi-empirical mass loss description has two regimes, above and below $M = 2.5M_{\odot}$, before they combine again at the onset of the super wind. As shown in Figure 4.7, the VW93 mass loss prescription seems to be over-producing the number of low mass, faint AGB stars more so than the higher mass AGB stars. The N_{AGB}/N_{RGB} ratio shows the same over-production of AGB stars, even more so than the G10 model.

Outside of the outlier DDO82, the fractional differences for high mass luminous $F160W \lesssim -7.5$ AGB stars are between $\sim -10\%$ and $+50\%$. Given that the residuals are high at all magnitudes where the number of AGB stars is well constrained, it seems a more efficient mass loss prescription is needed for stars in this low metallicity regime.

Mass Loss in the BS95 Model

The middle panels of Figure 4.3 shows the predicted LF for the BS95 prescription. These models produce far fewer AGB stars at all magnitudes compared to the other two mass loss prescriptions, for every galaxy in this sample. This is the preferred direction of change, since current TPAGB models over-predict the number of AGB stars compared to RGB stars.

The fractional difference between the observed and predicted LF (shown in Figure 4.8) is consistently small over all magnitudes, and is never more than 50%. For most cases, and at most magnitudes, the percentage difference is zero or a 10% underproduction. At worst, it over-predicts the integrated number of stars brighter than $F160W \sim -7.5$ by 30-50%.

More details can be seen when examining the direct residuals in the number of stars per bin. Below $F160W \sim -6.8$, there are increasing disagreements between the model predictions and observations although at a small % difference. Fainter than $F160W \sim -6.0$, there is a notable overproduction, and between $-6.8 \lesssim F160W \lesssim -6.8$, there is a slight underproduction.

While this seems to be the best fit, it is known that BS95 fails to reproduce the number of TP-AGB stars at SMC and LMC metallicities (Kamath et al., 2011). The best fit a low metallicity can also be interpreted more generally as a constraint on the $\dot{M}$ efficiency needed to match AGB lifetimes at low metallicity, regardless of the underlying wind model.

4.7.2 What is Responsible for the Model-Data Disagreements

Using several galaxies and several mass loss prescriptions allows us to differentiate between problems related to differing mass loss prescriptions and systematic errors in the input SFHs. If a feature in the LF is present in all the models, it's likely related to something in common between all models, and not related to the different mass loss prescriptions. Similarly, if a feature is present in only one galaxy, but all models, it is most likely due to incorrect input parameters, such as the SFH.

In this context, we now evaluate models to constrain where the TP-AGB models are deficient.

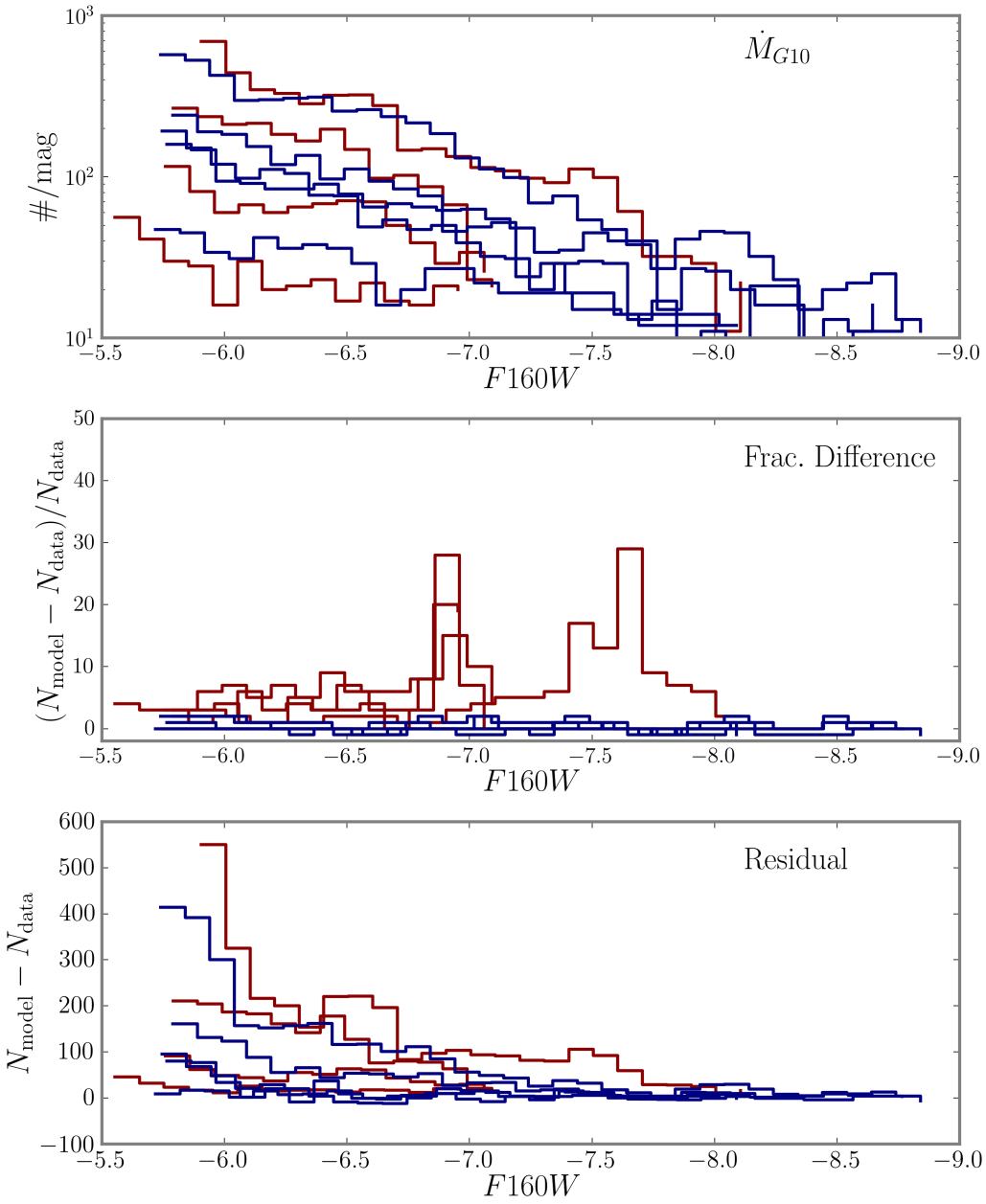

Figure 4.6 A comparison of the LF produced by the $\dot{M}_{G10}$ models. Top panel shows the LF of the models for each galaxy, this is a combination of the right-most panels of Figure 4.3. The percent difference in each magnitude bin is shown in the middle panel, and the bottom panel shows the residuals of the model and data. Galaxies with recent star formation are colored blue, the rest are colored red.

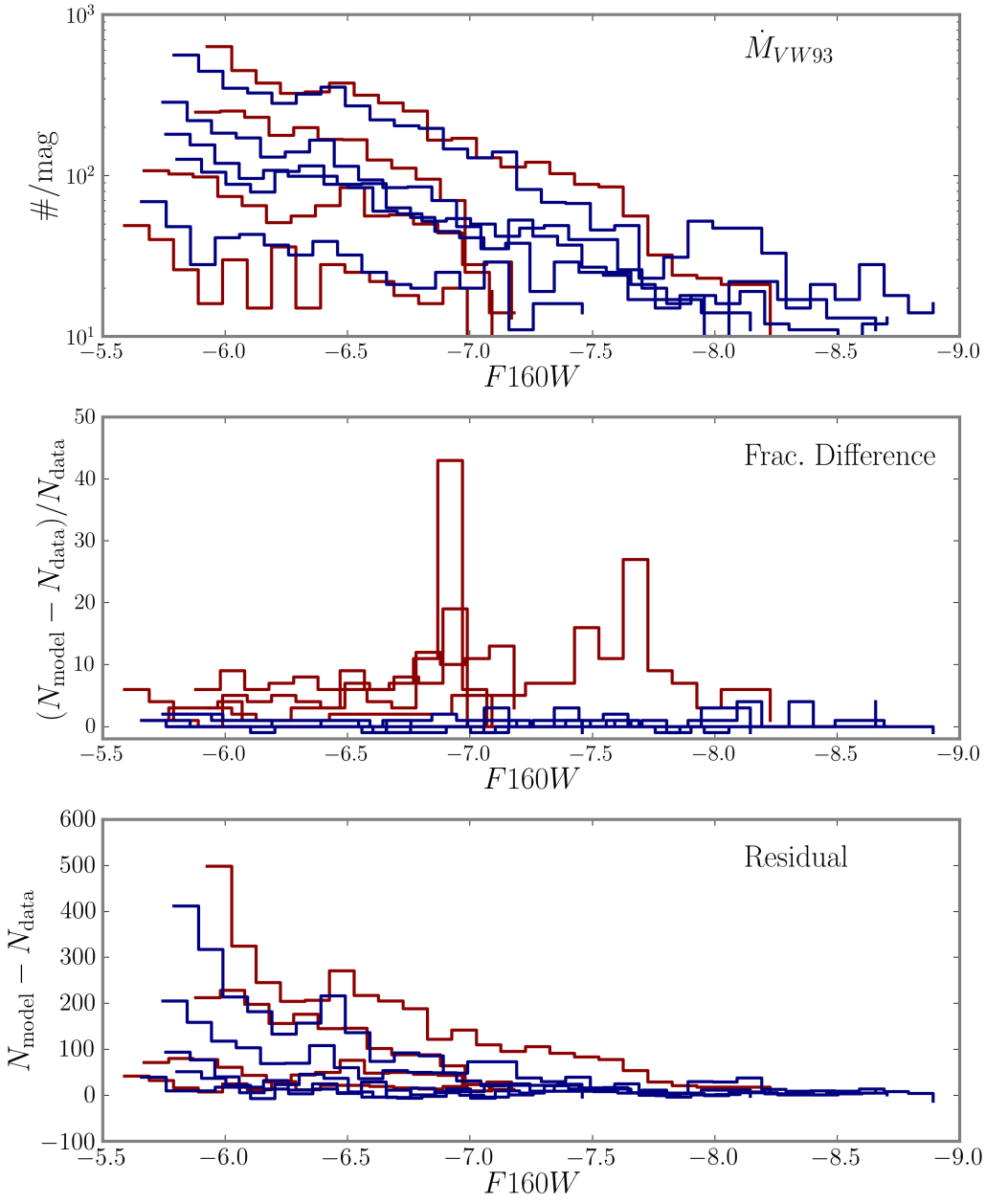

Figure 4.7 Same as Figure 4.6 but with $\dot{M}_{VW93}$.

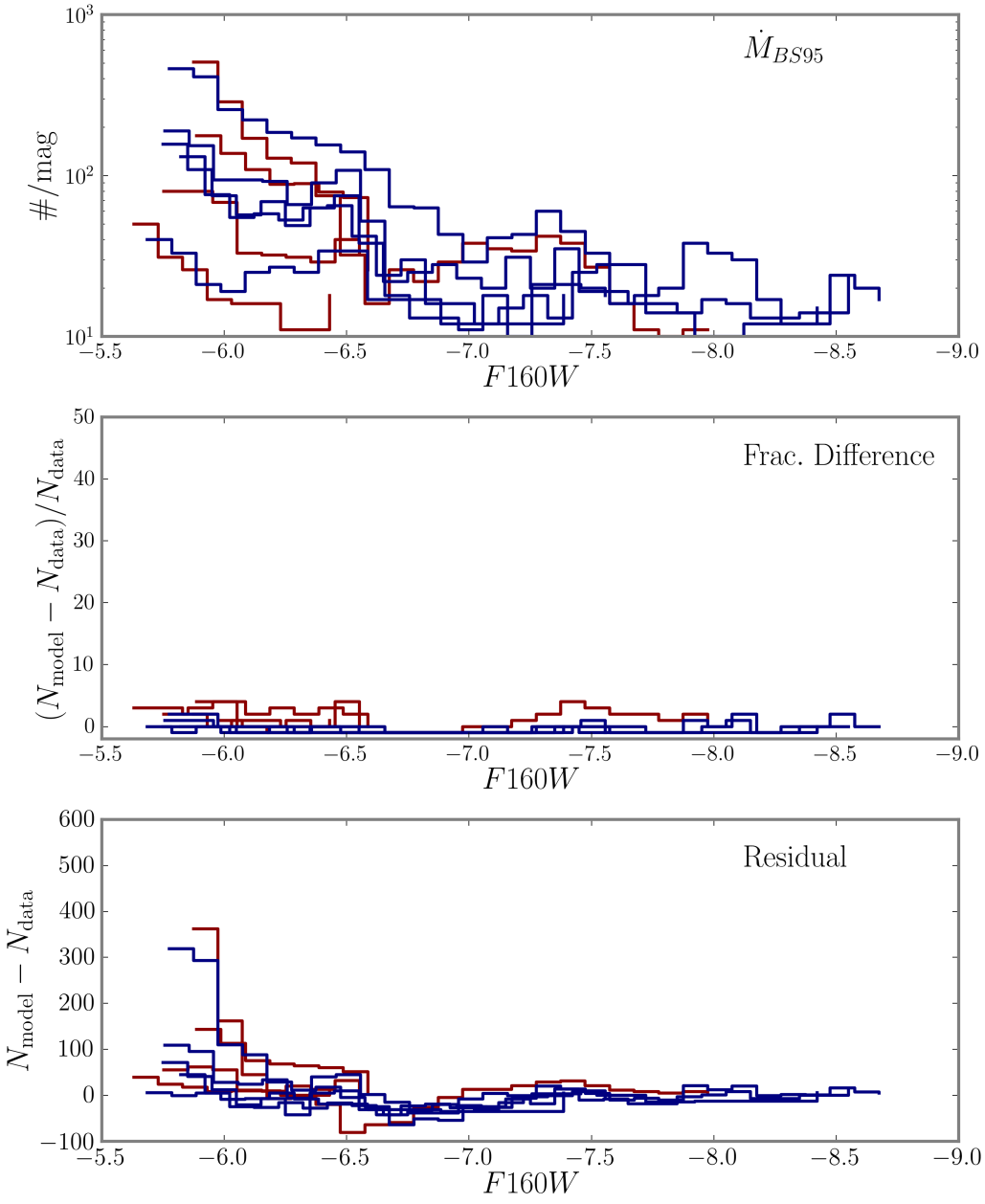

Figure 4.8 Same as Figure 4.6 but with $\dot{M}_{BS95}$.

Some unavoidable artifacts come from the mismatch between the stellar evolution models used to derive the SFH and those used to populate the simulated galaxies. The only appreciable example is DDO82, and it is worth examining. In Figures 4.6-4.7, a large overproduction of AGB stars is concentrated between $-8 \lesssim F160W \lesssim -7$. This feature is present in all models (though to different extremes) and for DDO82, corresponds exactly to a peak in SF at the corresponding age.

This issue is due to how TRILEGAL uses MATCH-derived SFHs. MATCH initially derives the SFH using a high temporal resolution grid that is then typically re-binned to lower resolution, which decreases the number of free parameters to a level consistent with the desired uncertainties (see discussion in Dolphin, 2002). The high temporal resolution SFH has large uncertainties in any individual time bin, for two reasons. First, there are random errors due to the limited number of stars sampled in each time-step in the CMD, and second, there is covariance from adjacent bins, since photometric uncertainties prevent any individual star from being uniquely assigned to an arbitrarily narrow time bin, particularly in the absence of detecting the MSTO. However, we have adopted the high resolution best fitting SFH solution because it allows TRILEGAL (discussed in Section 4.5) to simulate short lived evolutionary phases. We treat this SFH as a correct representation of the relative amount of SF in each time bin as it best reproduces the observed CMD. However, the total mass of stars formed in each time bin may not be correct for the limitations given above. Our choice to adopt the high resolution SFH will therefore introduce systematic errors due to the presence of SF features at specific times that may not in fact be statistically distinguishable from more robust SF spread over multiple adjacent time bins (see Section 4.7.2).

For the case of DDO82 specifically, the MATCH-derived high resolution SFH has a corresponding SF peak at exactly log Age$= 6.8 - 7.0$. However, the re-binned and Monte Carlo tested SFH shown in Figure 3 of Weisz et al. (2011) shows a much lower peak, smoothed over several Myr. Therefore, the large percent difference seen in 4.6-4.7 for DDO82 largely an artifact of using the high resolution SFH file, rather than differences in

the TP-AGB models.

Unfortunately, the only way around systematic errors in SFH is to include many galaxies in the analysis, and do this sort of comparison. For that reason, we have made the same comparisons for each galaxy, and found no significant population of TP-AGB stars that follows the same trend. That is, the LF of DDO82, from $-8 \lesssim F160W \lesssim -7$ is spuriously populated with TP-AGB stars and will be excluded from further comparisons of the mass loss prescriptions.

4.7.3 Bracketing the Mass Loss Prescription

As shown in above, all mass loss models except $\dot{M}_{BS95}$ over-predict the number of stars on the TPAGB. In effect, these three mass loss prescriptions introduce a constraint on the lifetimes of TP-AGB. The lifetimes of $Z = 0.002$ TP-AGB stars as a function of mass are shown in Figure 4.9. In the left panel we show the total TP-AGB lifetimes, and in the right panel, only the amount of time in the TP-AGB phase brighter than $L = 3.4L_{\odot}$, that is, approximately brighter than the TRGB. Shaded in grey in each panel shows the likely lifetimes as a function of mass.

Comparing the two panels of Figure 4.9, it is clear that much of the TP-AGB lifetime of stars with $M \lesssim 2M_{\odot}$ is spent below the TRGB. This result may in fact be reasonable, but must be checked using other constraints in TP-AGB evolution besides mass loss. For example, the speed of evolution from the early AGB to the beginning of the thermal pulses may not be well calibrated. If the speed is faster, the time spent below the TRGB would shorten, though so would the overall lifetime of the TP-AGB phase. Furthermore, the amount of time below the TRGB should make one suspicious of using only the N_{AGB}/N_{RGB} ratio to assess the adequacy of AGB models.

4.8 Conclusions

We have expanded G10 to six more galaxies, to younger SFHs, and thus a larger TP-AGB mass range. We find the PARSEC models with the TP-AGB calculated with COLIBRI still overproduce the number of stars compared to the number observed. From the comparison

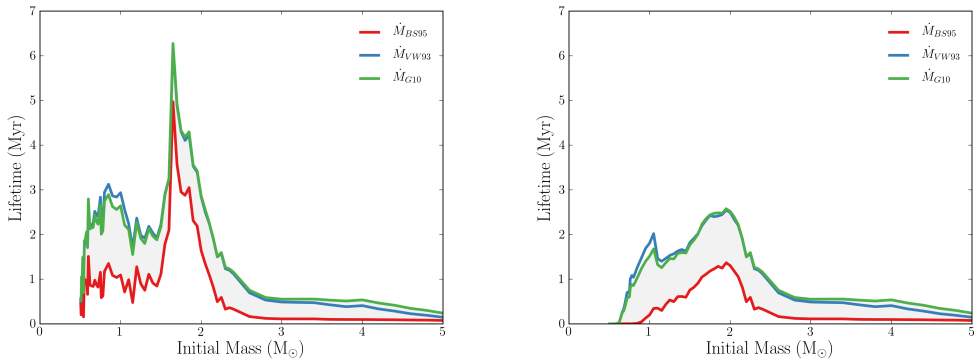

Figure 4.9 The lifetimes of TP-AGB stars with each mass loss prescription vs initial mass. The mass loss prescriptions bracket the probable lifetimes of TP-AGB stars (filled in grey). Left panel: Full TP-AGB tracks, right panel: TP-AGB stars brighter than the TRGB

of three differing mass loss prescriptions we bracketed lifetimes of $Z = 0.002$ TP-AGB stars to a few Myr for masses $1M_\odot \lesssim M \lesssim 3M_\odot$.

This chapter represents the first step in a major calibration of the COLIBRI code which will aid in the understanding of the physics involved in AGB evoluton. Constraining the lifetimes of TP-AGB stars is not possible with only two adjustable parameters (in this case, SFH and mass loss prescriptions). There are other physical relationships that are uncertain in TP-AGB stars, and some are parameterized in COLIBRI. Among the most uncertain is the efficiency of the third dredge up and its effect on the luminosity evolution, which can also limit the lifetimes of TP-AGB stars and be a degenerate parameter with mass loss (e.g., Karakas et al., 2002). These parameters should have the largest impacts at higher masses.

To further constrain low-mass TP-AGB lifetimes, and thus improve the accuracy of TP-AGB models, several steps are clear: 1) mass loss should be examined earlier in AGB evolution, perhaps during the early-AGB (EAGB) phase; 2) the data sample should be extended to include all the galaxies in the ANGST survey, as well as clusters and fields in the LMC; and 3) the data sample should be extended include higher metallicities, using the large database of TP-AGB stars in M31 observed as part of the Panchromatic Hubble Andromeda Treasury Survey.

Chapter 5

CONCLUSION

This thesis has shown the how *HST* observations of resolved stellar populations can be used to improve stellar evolution models. We focused on the extreme horizontal branch and their progeny, luminous core Helium burning stars, and the thermally pulsating AGB.

We showed in Chapter 2, that AGB-manqué and PE-AGB stars are very centrally located in the bulge of the Andromeda Galaxy and their origins are probably due stars with high amounts of He, possibly due to high metallicity. For the first time we provided an estimate of the fraction of evolved stars in the bulge that must go chose the HPHB evolutionary channel to provide the light we detect. These results bring us closer to understanding the origin of the UVX in the bulge of M31, which is the only proxy to an elliptical galaxy we can resolve into stars.

The stellar mass range that can physically become an EHB star and then an HPHB star is so small ($\Delta M \sim 0.02 M_{\odot}$) and the lifetimes of HPHB stars as short enough that there is promise to use the HPHB signature as an age indicator. Dedicated observations in the UV are needed to distinguish between uncertain model parameters, that is high Helium or metallicity, as well as test RGB mass loss prescriptions.

In Chapter 3, we made use of perhaps the best survey of HeB stars to date with sequences in nearby galaxies that are populated from $\sim 2 - 12 M_{\odot}$. We showed that the models better match the data if they include a core convective overshooting prescription that increases with mass. This was a simple first attempt made by interpolating models calculated with different strengths of core overshooting.

To further calibrate HeB models, envelope overshooting needs deeper investigation, especially its variation with metallicity. This is an inherently complex process however, especially at higher masses, when mass loss and rotation become more important and may have the same effect as an increase in envelope overshooting.

The RHeB was left unconstrained by mass dependent core overshooting, largely because a large convective envelope will redistribute such effects. To understand the RHeB, we must look to atmospheric models.

The final project of the thesis was an initial calibration of AGB stars. This time using low metallicity nearby galaxies to constrain low mass TP-AGB models. We used four filter *HST* catalogs and found that even the improvements made by our preceding study, Girardi et al. (2010), the lifetimes of TP-AGB stars were still too long, that is the number of AGB stars to RGB stars were still higher than that seen in the data, and more importantly, large offsets were seen when comparing the luminosity functions.

We also found that Blöcker & Schönberner (1995) mass loss prescription was too effective for many of the galaxies in our sample, leading us to bracket the mass loss prescriptions between that and Girardi et al. (2010)'s prescription.

Other parameters in TP-AGB evolution are now necessary to calibrate. The rate the AGB star begins thermal pulsating, the efficiency of the dredge up process and the effects of hot bottom burning are all uncertain parameters than can help us unravel the physics of the TP-AGB.

In summary, we have used observations from *HST* of nearby galaxies to improve stellar evolution models. We have gained insight into the peculiar UV-bright stars residing in the central regions of M31, we have found a major constraint to improve the modeling of luminous core He-burning stars, and narrowed the parameter space for TP-AGB mass loss in low metallicty systems.

These findings, when incorporated into new stellar evolution models and propagated to analysis packages like MATCH and FSPS, will help extragalactic astronomers better understand the histories of the galaxies they resolve, will help the confidence limits of cosmological simulations, and will further our understanding of the physics of stars in our universe.

BIBLIOGRAPHY

Aerts, C., Thoul, A., Daszyńska, J., et al. 2003, Science, 300, 1926

Anders, E., & Grevesse, N. 1989, Geochim. Cosmochim. Acta, 53, 197

Andersen, J., Clausen, J. V., & Nordstrom, B. 1990, ApJ, 363, L33

Aringer, B., Girardi, L., Nowotny, W., Marigo, P., & Lederer, M. T. 2009, A&A, 503, 913

Barmby, P., Ashby, M. L. N., Bianchi, L., et al. 2006, ApJ, 650, L45

Becker, S. A. 1981, ApJS, 45, 475

Bedijn, P. J. 1988, A&A, 205, 105

Bell, E. F., & de Jong, R. S. 2001, ApJ, 550, 212

Bensby, T., Feltzing, S., Johnson, J. A., et al. 2010, A&A, 512, A41+

Berg, D. A., Skillman, E. D., Marble, A. R., et al. 2012, ApJ, 754, 98

Bertelli, G., Bressan, A., Chiosi, C., & Angerer, K. 1986, A&AS, 66, 191

Bertelli, G., Bressan, A., Chiosi, C., Fagotto, F., & Nasi, E. 1994, A&AS, 106, 275

Bertelli, G., Bressan, A. G., & Chiosi, C. 1985, A&A, 150, 33

Bertola, F., Bressan, A., Burstein, D., et al. 1995, ApJ, 438, 680

Blöcker, T., & Schönberner, D. 1995, in American Institute of Physics Conference Series, Vol. 327, Nuclei in the Cosmos III, ed. M. Busso, C. M. Raiteri, & R. Gallino, 399

Böhm-Vitense, E. 1958, ZAp, 46, 108

Boyer, M. L., Skillman, E. D., van Loon, J. T., Gehrz, R. D., & Woodward, C. E. 2009, ApJ, 697, 1993

Boyer, M. L., van Loon, J. T., McDonald, I., et al. 2010, ApJ, 711, L99

Bressan, A., Bertelli, G., & Chiosi, C. 1986, Mem. Soc. Astron. Italiana, 57, 411

Bressan, A., Chiosi, C., & Fagotto, F. 1994, ApJS, 94, 63

Bressan, A., Marigo, P., Girardi, L., Nanni, A., & Rubele, S. 2013, in European Physical Journal Web of Conferences, Vol. 43, European Physical Journal Web of Conferences, 3001

Bressan, A., Marigo, P., Girardi, L., et al. 2012, MNRAS, 427, 127

Bressan, A. G., Chiosi, C., & Bertelli, G. 1981, A&A, 102, 25

Brocato, E., Castellani, V., Di Carlo, E., Raimondo, G., & Walker, A. R. 2003, AJ, 125, 3111

Brown, T. M., Bowers, C. W., Kimble, R. A., Sweigart, A. V., & Ferguson, H. C. 2000, ApJ, 532, 308

Brown, T. M., Ferguson, H. C., Davidsen, A. F., & Dorman, B. 1997, ApJ, 482, 685

Brown, T. M., Ferguson, H. C., Stanford, S. A., & Deharveng, J.-M., B. 1998, ApJ, 504, 113

Brown, T. M., Smith, E., Ferguson, H. C., et al. 2008, ApJ, 682, 319

Burstein, D., Bertola, F., Buson, L. M., Faber, S. M., & Lauer, T. R. 1988, ApJ, 328, 440

Buzzoni, A., & González-Lópezlira, R. A. 2008, ApJ, 686, 1007

Caffau, E., Ludwig, H.-G., Steffen, M., et al. 2008, A&A, 488, 1031

Cardelli, J. A., Clayton, G. C., & Mathis, J. S. 1989, ApJ, 345, 245

Carollo, C. M., Danziger, I. J., & Buson, L. 1993, MNRAS

Carter, D., Pass, S., Kennedy, J., Karick, A. M., & Smith, R. J. 2011, MNRAS, 656

Castelli, F., & Kurucz, R. L. 2003, in IAU Symposium, Vol. 210, Modelling of Stellar Atmospheres, ed. N. Piskunov, W. W. Weiss, & D. F. Gray, 20P

Catelan, M. 2009, Horizontal Branch Stars and the Ultraviolet Universe, Astrophysics and Space Science Proceedings (Springer New York), 1–16

Chiosi, C., Bertelli, G., & Bressan, A. 1992, ARA&A, 30, 235

Ciardullo, R., Rubin, V. C., Ford, Jr., W. K., Jacoby, G. H., & Ford, H. C. 1988, AJ, 95, 438

Claret, A. 2007, A&A, 475, 1019

Code, A. D. 1969, PASP, 81, 475

Conroy, C., Gunn, J. E., & White, M. 2009, ApJ, 699, 486

Cordier, D., Lebreton, Y., Goupil, M.-J., et al. 2002, A&A, 392, 169

Courteau, S., Widrow, L. M., McDonald, M., et al. 2011, ArXiv e-prints, arXiv:1106.3564

Croxall, K. V., van Zee, L., Lee, H., et al. 2009, ApJ, 705, 723

Dalcanton, J. J., Williams, B. F., Seth, A. C., et al. 2009, ApJS, 183, 67

Dalcanton, J. J., Williams, B. F., Lang, D., et al. 2012, ApJS, 200, 18

Davies, R. L., Sadler, E. M., & Peletier, R. F. 1993, MNRAS, 262, 650

de Meulenaer, P., Carrier, F., Miglio, A., et al. 2010, A&A, 523, A54

Decressin, T., Meynet, G., Charbonnel, C., Prantzos, N., & Ekström, S. 2007, A&A, 1044, 1029

Dohm-Palmer, R. C., & Skillman, E. D. 2002, AJ, 123, 1433

Dohm-Palmer, R. C., Skillman, E. D., Saha, A., et al. 1997, AJ, 114, 2527

Dolphin, A. E. 2000, PASP, 112, 1383

—. 2002, MNRAS, 332, 91

Dorman, B., O'Connell, R. W., & Rood, R. T. 1995, ApJ, 442, 105

Ferguson, H. C., & Davidsen, A. F. 1993, ApJ, 408, 92

Fluks, M. A., Plez, B., The, P. S., et al. 1994, A&AS, 105, 311

Frogel, J. A., Mould, J., & Blanco, V. M. 1990, ApJ, 352, 96

Gallart, C., Zoccali, M., & Aparicio, A. 2005, ARA&A, 43, 387

Gilbert, K., Dalcanton, J. J., Williams, B. F., et al. 2013, to be submitted to PASP

Gim, M., Vandenberg, D. A., Stetson, P. B., Hesser, J. E., & Zurek, D. R. 1998, PASP, 110, 1318

Girardi, L., Bressan, A., Bertelli, G., & Chiosi, C. 2000, A&A, 141, 371

Girardi, L., Groenewegen, M. A. T., Hatziminaoglou, E., & da Costa, L. 2005a, A&A, 436, 895

—. 2005b, A&A, 436, 895

Girardi, L., & Marigo, P. 2007, A&A, 462, 237

Girardi, L., Rubele, S., & Kerber, L. 2009, MNRAS, 394, L74

Girardi, L., Dalcanton, J., Williams, B., et al. 2008a, PASP, 120, 583

—. 2008b, PASP, 120, 583

Girardi, L., Williams, B. F., Gilbert, K. M., et al. 2010, ApJ, 724, 1030

Girardi, L., Williams, B. F., Gilbert, K. M., et al. 2010, ApJ, 724, 1030

Godart, M., Noels, A., & Scuflaire, R. 2013, in European Physical Journal Web of Conferences, Vol. 43, European Physical Journal Web of Conferences, 1008

Gorgas, J., Efstathiou, G., & Aragon Salamanca, A. 1990, MNRAS, 245, 217

Greggio, L., & Renzini, A. 1990, ApJ, 364, 35

—. 1999, Mem. Soc. Astron. Italiana, 70, 691

Groenewegen, M. A. T. 2006, A&A, 448, 181

Groenewegen, M. A. T., Sevenster, M., Spoon, H. W. W., & Pérez, I. 2002, A&A, 390, 511

Gullieuszik, M., Held, E. V., Rizzi, L., et al. 2008, MNRAS, 388, 1185

Han, Z., Podsiadlowski, P., & Lynas-Gray, A. E. 2007, MNRAS, 380, 1098

Han, Z., Podsiadlowski, P., Maxted, P. F. L., & Marsh, T. R. 2003, MNRAS, 341, 669

Han, Z., Podsiadlowski, P., Maxted, P. F. L., Marsh, T. R., & Ivanova, N. 2002, MNRAS, 336, 449

Held, E. V., Gullieuszik, M., Rizzi, L., et al. 2010, MNRAS, 404, 1475

Herwig, F. 2005, ARA&A, 43, 435

Holtzman, J. A., Afonso, C., & Dolphin, A. 2006, ApJS, 166, 534

Horch, E., Demarque, P., & Pinsonneault, M. 1992, ApJ, 388, L53

Jablonka, P., Gorgas, J., & Goudfrooij, P. 2007, A&A, 474, 763

Kalirai, J. S., Bergeron, P., Hansen, B. M. S., et al. 2007, ApJ, 671, 748

Kamath, D., Wood, P. R., Soszyński, I., & Lebzelter, T. 2010, MNRAS, 408, 522

Kamath, D., Wood, P. R., Soszyński, I., & Lebzelter, T. 2011, in Astronomical Society of the Pacific Conference Series, Vol. 445, Why Galaxies Care about AGB Stars II: Shining Examples and Common Inhabitants, ed. F. Kerschbaum, T. Lebzelter, & R. F. Wing, 127

Kang, Y., Bianchi, L., & Rey, S.-C. 2009, ApJ, 703, 614

Karakas, A. I., Lattanzio, J. C., & Pols, O. R. 2002, PASA, 19, 515

Kerschbaum, F., Charbonnel, C., & Wing, R. F., eds. 2007, Astronomical Society of the Pacific Conference Series, Vol. 378, Why Galaxies Care About AGB Stars: Their Importance as Actors and Probes

Kerschbaum, F., Lebzelter, T., & Wing, R. F., eds. 2011, Astronomical Society of the Pacific Conference Series, Vol. 445, Why Galaxies Care about AGB Stars II: Shining Examples and Common Inhabitants

King, I. R., Stanford, S. A., & Crane, P. 1995, AJ, 109, 164

King, I. R., Deharveng, J. M., Albrecht, R., et al. 1992, ApJ, 397, L35

Kippenhahn, R., Weigert, A., & Weiss, A. 2013, Stellar Structure and Evolution, doi:10.1007/978-3-642-30304-3

Kniazev, A. Y., Grebel, E. K., Pustilnik, S. A., Pramskij, A. G., & Zucker, D. B. 2005, AJ, 130, 1558

Kobayashi, C., & Arimoto, N. 1999, ApJ, 527, 573

Kobulnicky, H. A., & Skillman, E. D. 1996, ApJ, 471, 211

Koekemoer, A. M., Fruchter, A. S., Hook, R. N., & Hack, W. 2003, in The 2002 HST Calibration Workshop : Hubble after the Installation of the ACS and the NICMOS Cooling System, Proceedings of a Workshop held at the Space Telescope Science Institute, Baltimore, Maryland, October 17 and 18, 2002. Edited by Santiago Arribas, Anton Koekemoer, and Brad Whitmore. Baltimore, MD: Space Telescope Science Institute, 2003., p.337, ed. S. Arribas, A. Koekemoer, & B. Whitmore, 337

Kroupa, P. 2001, MNRAS, 322, 231

Lamers, H. J. G. L. M., & Cassinelli, J. P. 1999, Introduction to Stellar Winds (Cambridge University Pres)

Langer, N., & Maeder, A. 1995, A&A, 295, 685

Lebzelter, T., & Wood, P. R. 2007, A&A, 475, 643

Lee, H., McCall, M. L., Kingsburgh, R. L., Ross, R., & Stevenson, C. C. 2003, AJ, 125, 146

Maeder, A., & Conti, P. S. 1994, ARA&A, 32, 227

Maeder, A., & Meynet, G. 2001, A&A, 373, 555

Maraston, C. 1998, MNRAS, 300, 872

—. 2005a, MNRAS, 362, 799

—. 2005b, MNRAS, 362, 799

Marble, A. R., Engelbracht, C. W., van Zee, L., et al. 2010, ApJ, 715, 506

Marigo, P. 2013, in IAU Symposium, Vol. 281, IAU Symposium, ed. R. Di Stefano, M. Orio, & M. Moe, 36–43

Marigo, P., Girardi, L., Bressan, A., et al. 2008, A&A, 482, 883

Matraka, B., Wassermann, C., & Weigert, A. 1982, A&A, 107, 283

McConnachie, A. W., Irwin, M. J., Ferguson, A. M. N., et al. 2005, MNRAS, 356, 979

McQuinn, K. B. W., Skillman, E. D., Cannon, J. M., et al. 2009, ApJ, 695, 561

McQuinn, K. B. W., Skillman, E. D., Dalcanton, J. J., et al. 2011, ApJ, 740, 48

McQuinn, K. B. W., Skillman, E. D., Cannon, J. M., et al. 2010, ApJ, 724, 49

Melbourne, J., Williams, B., Dalcanton, J., et al. 2010, ApJ, 712, 469

Melbourne, J., Williams, B. F., Dalcanton, J. J., et al. 2012, ApJ, 748, 47

Melchior, A.-L., Viallefond, F., Guélin, M., & Neininger, N. 2000, MNRAS, 312, L29

Merrett, H. R., Merrifield, M. R., Douglas, N. G., et al. 2006, MNRAS, 142, 120

Meynet, G., Maeder, A., Schaller, G., Schaerer, D., & Charbonnel, C. 1994, A&AS, 103, 97

Norris, J. E. 2004, ApJ, 612, L25

O'Connell, R. W. 1999, ARA&A, 37, 603

O'Donnell, J. E. 1994, ApJ, 422, 158

Oh, S.-H., de Blok, W. J. G., Walter, F., Brinks, E., & Kennicutt, Jr., R. C. 2008, AJ, 136, 2761

Pagel, B. E. J., Simonson, E. A., Terlevich, R. J., & Edmunds, M. G. 1992, MNRAS, 255, 325

Papovich, C., Dickinson, M., & Ferguson, H. C. 2001, ApJ, 559, 620

Peletier, R. F., Davies, R. L., Illingworth, G. D., Davis, L. E., & Cawson, M. 1990, The Astronomical Journal, 100, 1091

Piersimoni, A. M., Bono, G., Castellani, M., et al. 1999, A&A, 352, L63

Reimers, D. 1975, Memoires of the Societe Royale des Sciences de Liege, 8, 369

Renzini, A., & Buzzoni, A. 1986a, in Astrophysics and Space Science Library, Vol. 122, Spectral Evolution of Galaxies, ed. C. Chiosi & A. Renzini, 195–231

Renzini, A., & Buzzoni, A. 1986b, in Astrophysics and Space Science Library, Vol. 122, Spectral Evolution of Galaxies, ed. C. Chiosi & A. Renzini, 195–231

Ribas, I., Jordi, C., & Giménez, Á. 2000, MNRAS, 318, L55

Roediger, J. C., Courteau, S., MacArthur, L. A., & McDonald, M. 2011, MNRAS, 1261

Rosenfield, P., Johnson, L. C., Girardi, L., et al. 2012, ApJ, 755, 131

Rosvick, J. M., & Vandenberg, D. A. 1998, AJ, 115, 1516

Saglia, R. P., Fabricius, M., Bender, R., et al. 2010, A&A, 509, A61

Salpeter, E. E. 1955, ApJ, 121, 161

Saslaw, W. C., & Schwarzschild, M. 1965, ApJ, 142, 1468

Saviane, I., Ivanov, V. D., Held, E. V., et al. 2008, A&A, 487, 901

Schiavon, R. P., Dalessandro, E., Sohn, S. T., et al. 2012, AJ, 143, 121

Schlegel, D. J., Finkbeiner, D. P., & Davis, M. 1998, ApJ, 500, 525

Schröder, K.-P., & Cuntz, M. 2005, ApJ, 630, L73

Seth, A. C. 2010, ApJ, 725, 670

Skrutskie, M. F., Cutri, R. M., Stiening, R., et al. 2006, AJ, 131, 1163

Stothers, R., & Chin, C.-W. 1981, ApJ, 247, 1063

Straka, C. W., Demarque, P., & Guenther, D. B. 2005, ApJ, 629, 1075

Thilker, D. A., Hoopes, C. G., Bianchi, L., et al. 2005, ApJ, 619, L67

Thomas, D., Maraston, C., & Bender, R. 2003, MNRAS, 339, 897

Thomsen, B., & Baum, W. A. 1987, ApJ, 315, 460

Trager, S. C., Faber, S. M., Worthey, G., & González, J. J. 2000, The Astronomical Journal, 119, 1645

Tüllmann, R., Rosa, M. R., Elwert, T., et al. 2003, A&A, 412, 69

Umezu, M. 1995, MNRAS, 276, 1287

van den Bergh, S. 1968, JRASC, 62, 219

van Loon, J. T., Marshall, J. R., & Zijlstra, A. A. 2005, A&A, 442, 597

van Loon, J. T., McDonald, I., Oliveira, J. M., et al. 2006, A&A, 450, 339

van Zee, L. 2000, ApJ, 543, L31

van Zee, L., & Haynes, M. P. 2006, ApJ, 636, 214

van Zee, L., Skillman, E. D., & Haynes, M. P. 2006, ApJ, 637, 269

VandenBerg, D. A., Bergbusch, P. A., & Dowler, P. D. 2006, ApJS, 162, 375

VandenBerg, D. A., & Stetson, P. B. 2004, PASP, 116, 997

Vassiliadis, E., & Wood, P. R. 1993, ApJ, 413, 641

Vassiliadis, E., & Wood, P. R. 1994, ApJS, 92, 125

Voss, R., & Gilfanov, M. 2007a, A&A, 468, 49

—. 2007b, MNRAS, 380, 1685

Walterbos, R. A. M., & Kennicutt, Jr., R. C. 1987, A&AS, 69, 311

Weisz, D. R., Dalcanton, J. J., Williams, B. F., et al. 2011, ApJ, 739, 5

Willson, L. A. 2000, ARA&A, 38, 573

Wirth, A. 1981, AJ, 86, 981

Woo, J.-H., & Demarque, P. 2001, AJ, 122, 1602

Yi, S., Lee, Y.-w., Woo, J.-h., Park, J.-h., & Oemler, A. 1999, ApJ, 1, 128

Appendix A

A NOTE ON THE SFHS USED IN CHAPTER 4

There are two issues that are worth examining in the SFH section of Chapter 4. The first is the mismatch of using old and new stellar evolution models. The former to deduce the star formation histories of the galaxies, and the latter to populate synthetic CMDs. The second issue is using optically derived star formation histories to populate synthetic CMDs in the NIR. We examine the issues together below, finding strong issues in color, but not in luminocity.

G10 presented TP-AGB models that well describe the optical TP-AGB LF of 12 galaxies with very little recent star formation. To determine the SFH of the galaxy sample, they used Padova stellar evolution models (Girardi et al., 2000) with updates from (Marigo et al., 2008) which are part of MATCH software package (Dolphin, 2002). In Chapter 4, we used the same MATCH-derived SFHs as those in Melbourne et al. (2012); Girardi et al. (2010) and depended on the TRILEGAL catalog to predict the correct NIR magnitudes and colors in the synthetic CMD.

We now examine how optically derived models perform in the NIR using three of the galaxies analyzed in G10 (although our optical fields are trimmed to match the NIR footprint, see Dalcanton et al., 2012; Melbourne et al., 2012). We produce two synthetic CMDs (masking all AGB stars), one with the stellar evolution models very similar to those used in G10 of which the SFHs were derived, and the other with the PARSEC models (Bressan et al., 2012), used throughout this thesis.

Figures A.4-A.6 show four panel comparisons of the TRILEGAL simulations made with different stellar evolution models but the same SFHs. There are significant offsets in the NIR color of the RGB, partially due to known issues in the Girardi et al. (2000) models that have since been fixed. For example, if the RGB in the Girardi et al. (2000) models were bluer at low metallicities than are seen in the dwarf galaxy observations, MATCH

will compensate the fit by assigning a higher metallicity to the RGB. With the new models no longer showing these offsets, the RGB when populated by TRILEGAL, will be redder, coinciding with the erroneous increased metallicity from the MATCH derivation. However, these color differences are apparently unrelated to magnitude offsets, which are essentially unchanged between each SFH.

These tests therefore suggest that any conclusions based on the luminosities of predicted AGB stars should be hardly effected by using different stellar evolution models to derive the SFH and then populate the synthetic CMDs.

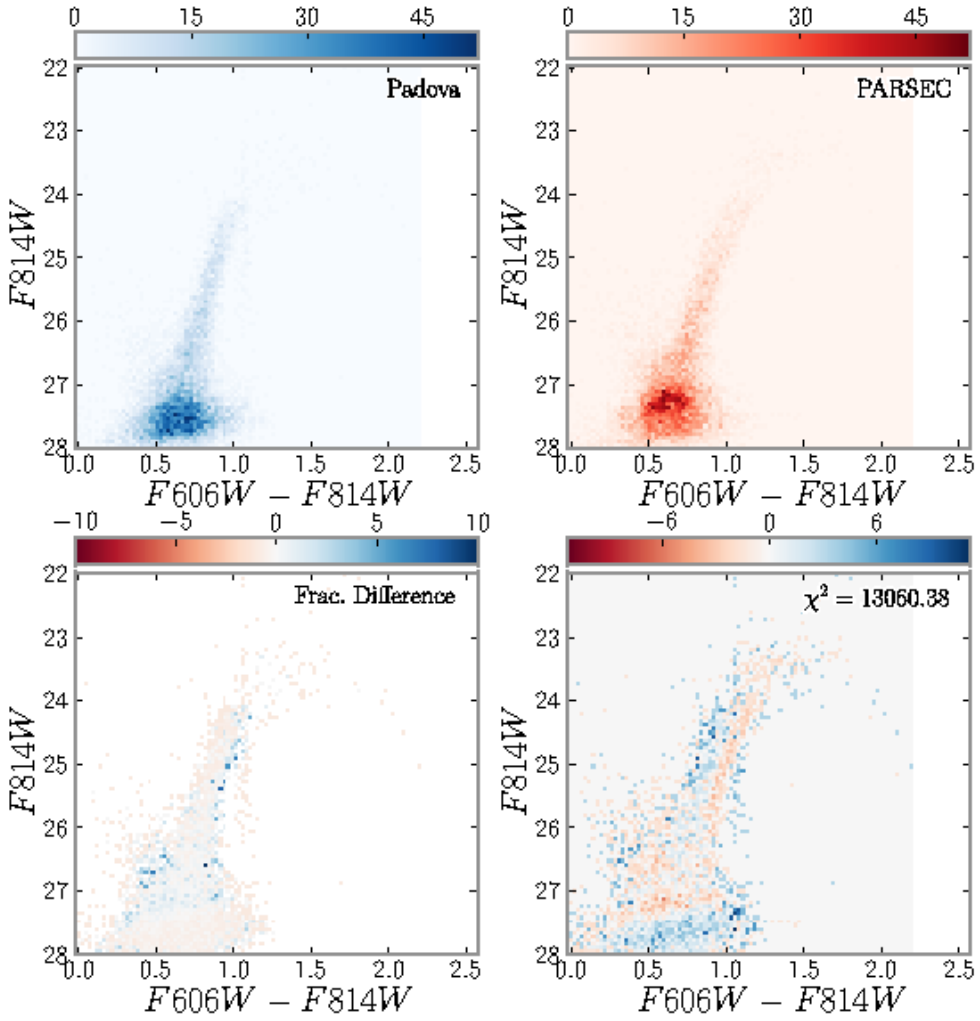

Figure A.1 TRILEGAL simulation using the SFH derived for SCL-DE1 calculated with stellar evolution models similar to those used in G10 (Padova) compared to the same, but calculated with PARSEC and COLIBRI. Top left: G10 models, top right: PARSEC and COLIBRI models, bottom left: fractional difference between the models, and bottom right: significance of difference given by $\text{sign}(n-m)\sqrt{\chi^2}$ where n is the number of stars in top left CMD, m is the number of stars in the top right CMD, and χ^2 is the Poisson-equivalent χ^2 statistic: $2(m + n(\log(n/m) - 1))$ (Dolphin, 2002). The total χ^2 is annotated on the bottom right panel. Differences in the models are discussed in the text.

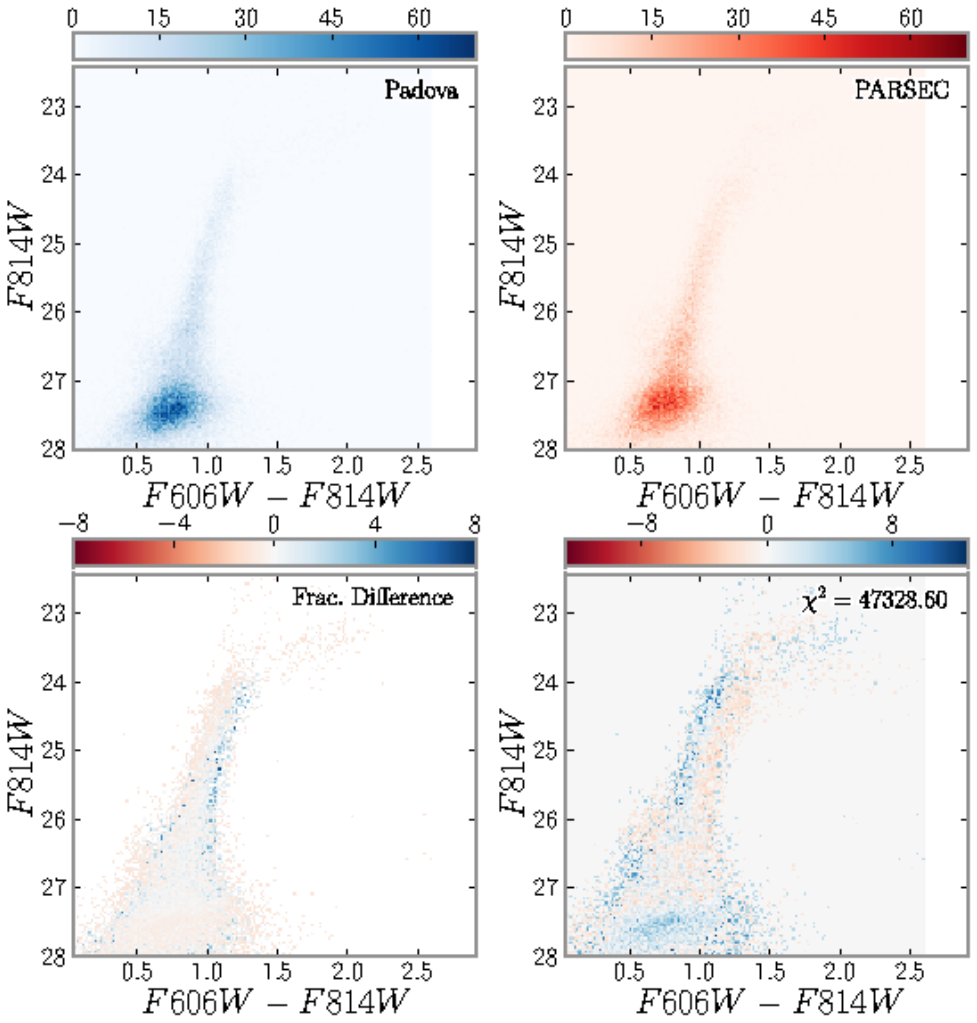

Figure A.2 Same as Fig. A.1 but for DDO71

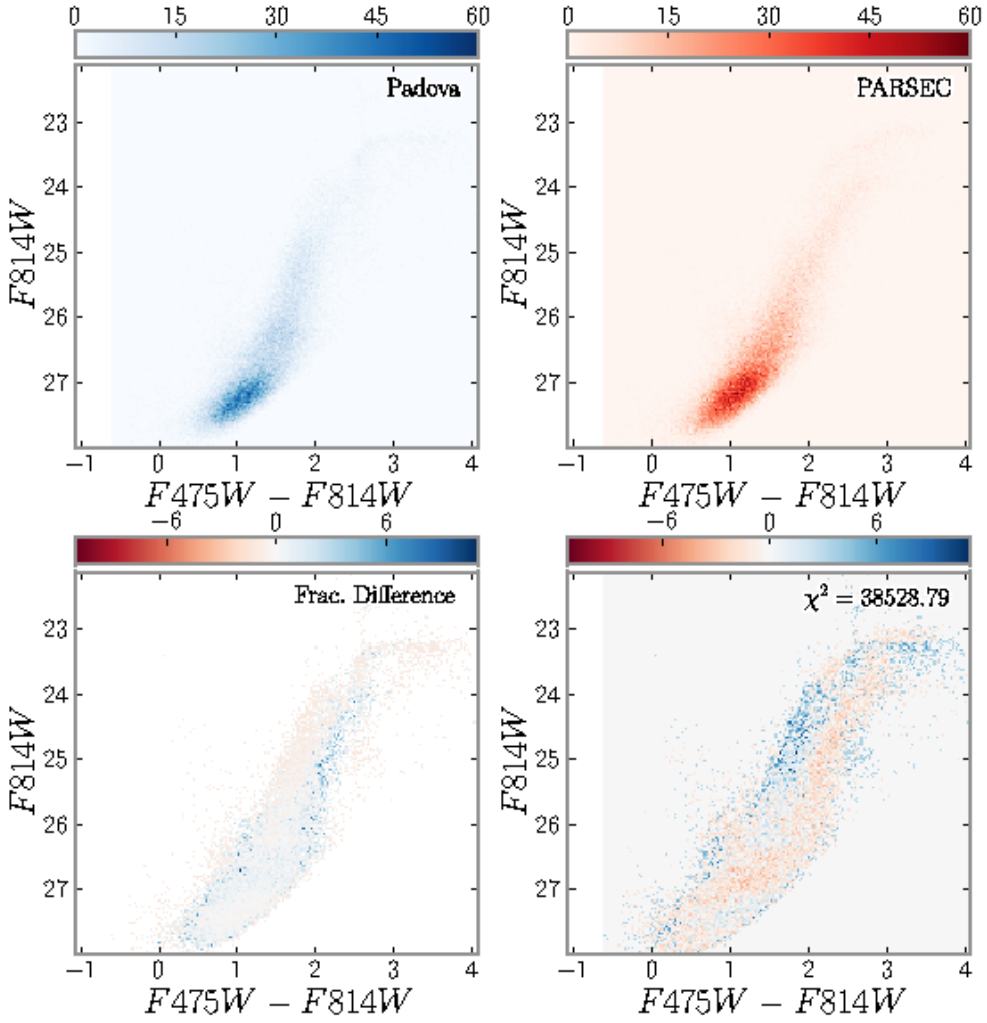

Figure A.3 Same as Fig. A.1 but for DDO78

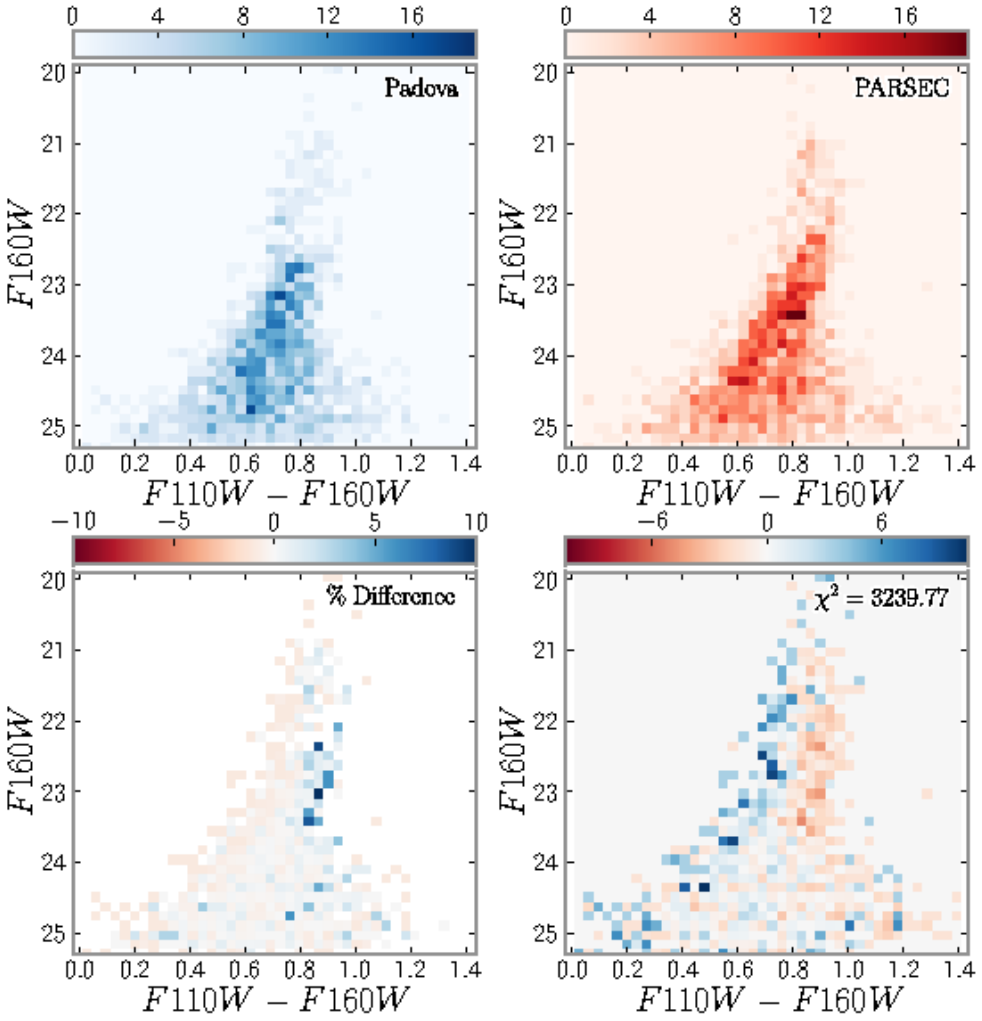

Figure A.4 Same as Fig. A.1 but showing NIR CMDs and LFs (SFHs still derived from optical CMDs).

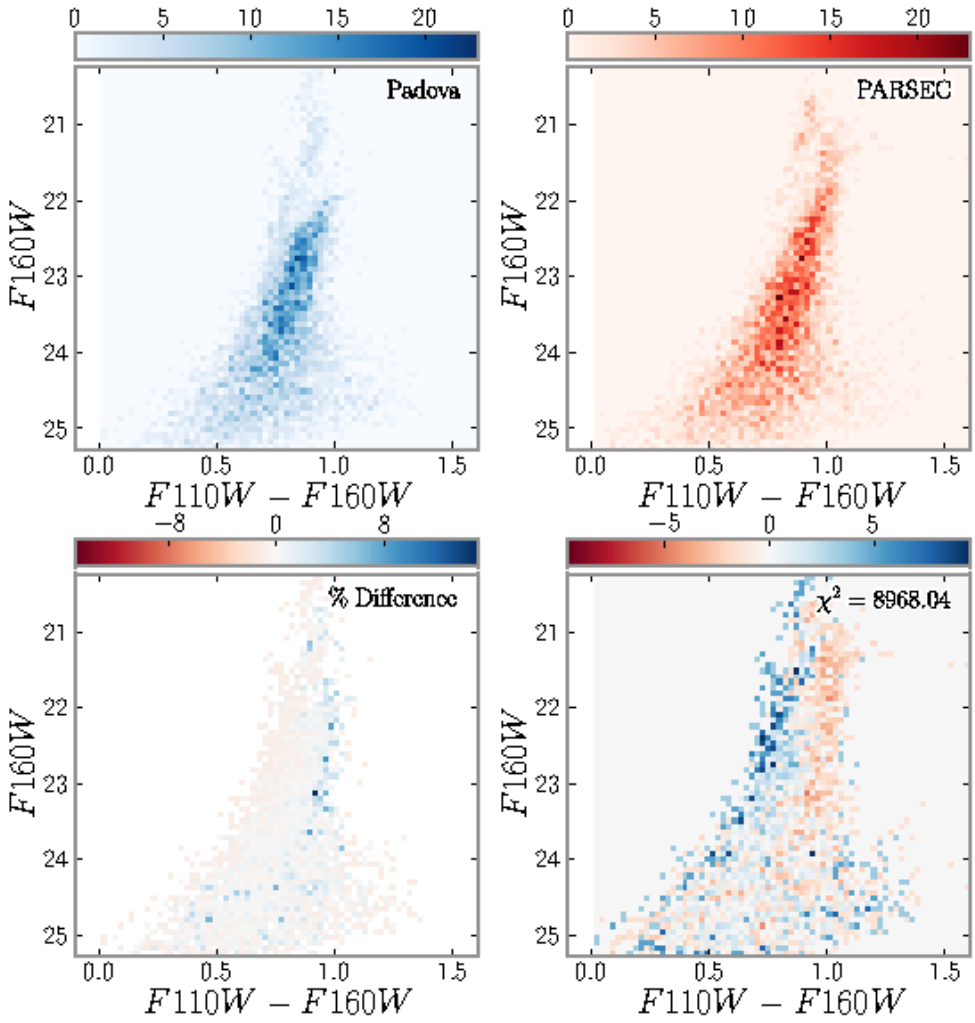

Figure A.5 Same as Fig. A.4 but for DDO71

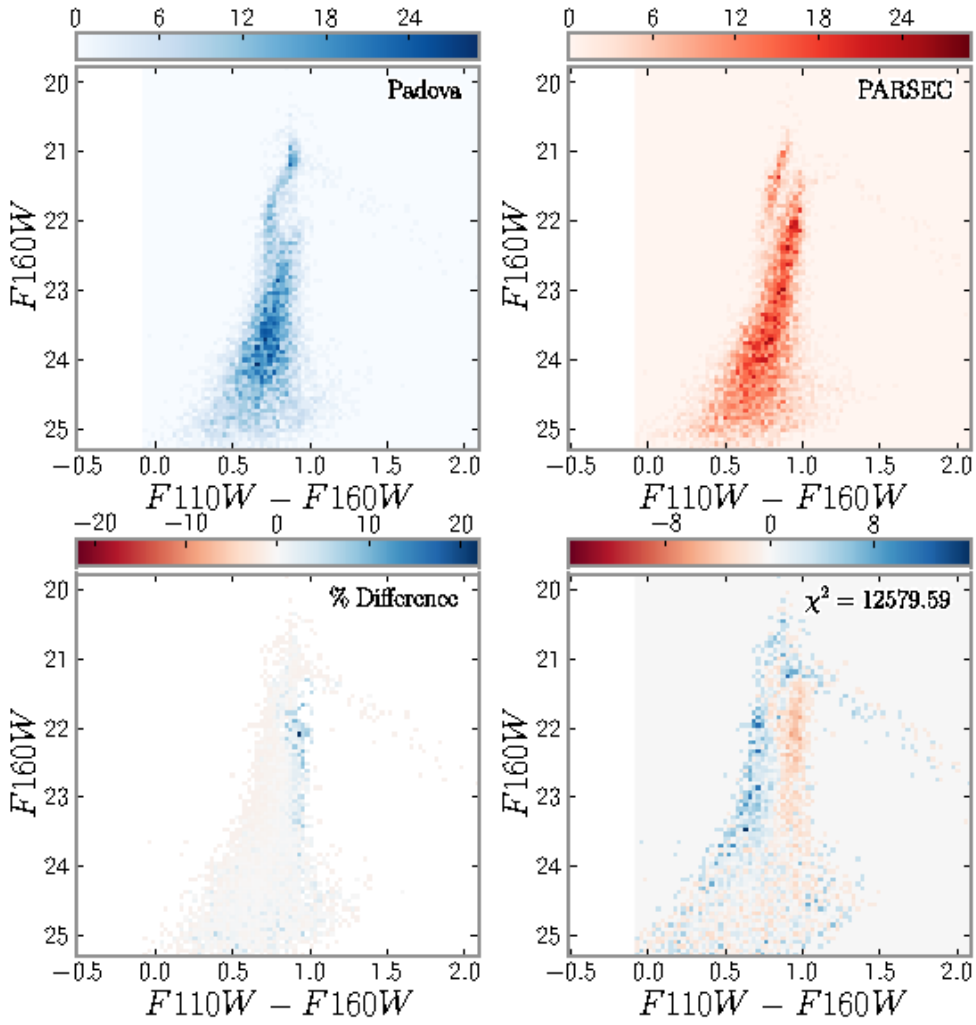

Figure A.6 Same as Fig. A.4 but for DDO78

VITA

Besides studying stellar evolution using resolved stellar populations in other galaxies, Phil Rosenfield has been coordinator of the UW planetarium, a director of the Forum on Science Ethics and Policy, started the Engage Program at UW (a program to train graduate students in effectively engaging public audiences with their research), and taught a freshman seminar to help retain under-represented students in STEM fields. Phil was an intern at Microsoft Research and worked to project WorldWide Telescope in planetariums and led the creation and building of the UW Moblie Planetarium. Before the UW, he earned an MS in Astronomy from San Diego State University after completing a BA in Physics and Astronomy from Boston University. He is originally from Minneapolis, MN.